# EFFECT OF MESOSCALE INHOMOGENEITIES ON PLANAR SHOCK RESPONSE OF MATERIALS

A Thesis
Presented to
The Academic Faculty

by

Brian A. Ferri

In Partial Fulfillment
of the Requirements for the Degree
Master of Science in the
George W. Woodruff School of Mechanical Engineering

Georgia Institute of Technology
May 2017

# EFFECT OF MESOSCALE INHOMOGENEITIES ON PLANAR SHOCK RESPONSE OF MATERIALS

Approved by:

Dr. Sunil Dwivedi, Advisor
School of Material Science
*Georgia Institute of Technology*

Dr. David McDowell
School of Mechanical Engineering
*Georgia Institute of Technology*

Dr. Richard Neu
School of Mechanical Engineering
*Georgia Institute of Technology*

Date Approved: April 14, 2017

To my friends and family

# ACKNOWLEDGEMENTS

I would like to thank my peers at Georgia Tech including the Computational Materials Group, as they were my family away from home. I would not have the level of understanding that I have today without them. I would also like to thank my mother and father for their support back at home. I do not think words can describe the appreciation I have for the work my advisor, Dr. Dwivedi, put in to make this thesis and my entire degree come to fruition. Finally, I would like to thank the support from the HDTRA1-12-1-0004 grant and from the School of Mechanical Engineering for supporting me on a Graduate Teaching Assistantship for one semester.

# TABLE OF CONTENTS

# LIST OF TABLES

# LIST OF FIGURES

# LIST OF SYMBOLS AND ABBREVIATIONS

| | |
|---|---|
| RH | Rankine Hugoniot |
| V | Specific Volume |
| $\rho$ | Density |
| $U_s$ | Shock Velocity |
| $u_p$ | Particle Velocity |
| $P$ | Pressure |
| $E$ | Energy |
| $C$ | Speed of Sound |
| $S$ | Slope of Hugoniot Line |
| $K$ | Bulk Modulus |
| $G$ | Shear Modulus |
| EOS | Equation of State |
| $\gamma$ | Gruneisen Coefficient |
| $\mu$ | Specific Volume Relationship |
| $\eta$ | Either Second Specific Volume Relationship or Viscosity Term for Jim Johnson Model |
| $K_n$ | Mie Gruneisen Coefficient for SHOCK-1D |
| $C_n$ | Mie Gruneisen Coefficient for LS-DYNA |
| $\sigma$ | Stress |
| $\delta_{ij}$ | Kronecker Delta |
| $\varepsilon$ | Strain |
| $H'$ | Hardening Parameter |
| $U_s$ | Shock Velocity |

| | |
|---|---|
| RVE | Representative Volume Element |
| $D_0$ | Damage Parameter for Cochran Banner Model |
| $\Sigma$ | Spall Strength for Cochran Banner Model Also Referred to as $Sp$ |
| $T^m$ | Maximum Traction for Cohesive Element Model Also Referred to as $M_{TR}$ |
| $\lambda$ | Distance Parameter for Cohesive Element Model Also Referred to as $C_{RD}$ and $F_{RD}$ |
| VNGC | Void Nucleation Growth and Coalescence |
| $\alpha$ | Distention Parameter for Jim Johnson Model |
| $\phi$ | Porosity |
| $a_s$ | Material Stress Parameter for Jim Johnson Model |
| $f$ | Objective Function |
| $\theta$ | Objective Function Parameters |
| $B^n$ | Body |
| $L^n$ | Body Length |
| $M^n$ | Merge Setting |
| LiF | Lithium Fluoride |
| UMAT | User Material Model |

# SUMMARY

In all previous spall models, the source of spall failure in metals either comes from damage at the grain boundary or from void nucleation, growth, and coalescence. However, it has been observed in experiments that both phenomena occur in Aluminum 6061-T6, which is termed "combined failure" for the purposes of this thesis. Thus, the challenge undertaken in this thesis is to use a computational study to determine the role that each source of spall plays separately, and then in tandem to determine the traditional failure parameters for each source. The results of determining each failure model's ideal parameters, which are representative of that source's role in combined failure, is compared with data gathered from plate-flyer experiments to determine the accuracy of the model in both 1D and in 2D simulations.

Sand is a heterogeneous granular material that has the capability of allowing a shock wave to propagate through it. The computational model and study presented in this thesis is phenomenologically similar, yet easier to conduct than a spall study on granular Aluminum. The study of sand using the same computational LS-DYNA method shows both an introduction to the process for completing the spall study on granular Aluminum, and it also yields interesting results in the wave phenomena as well as the effect of porosity on the average stress on the sand grains.

With the conclusion of the sand study, the same process of creating the grain structure is applied to create the Aluminum grain structure for spall simulations, which are carried out in LS-DYNA using 2D cohesive elements. The results of the LS-DYNA

Aluminum simulation are compared to both the 1D spall results as well as to the experimental data to determine model accuracy.

The main findings from this thesis show that, first, a mutually exclusive combined failure linear relationship can be shown with the 1D simulation results, which gives insight into a method that could be used to choose a set of optimal failure parameters. Second, the 2D LS-DYNA homogeneous results had excellent agreement with the 1D homogeneous results, which gave confidence to the notion that the parametric studies in 1D simulations could be used to find parameter values that could be applied in the 2D models. Lastly, LS-DYNA was shown to be an effective way to simulate grain structure response to shock wave propagation and showed spall modeling was possible with 2D cohesive elements, which lays the groundwork for combined failure studies in 2D.

# CHAPTER 1. INTRODUCTION

A sound wave is a mechanical wave that propagates through a medium (gases, liquids, solids) via material particles that vibrate around their mean position in a sinusoidal manner with a series of compressive and rarefaction pressure oscillations [1]. The amplitude and frequency (time-period) of a soundwave depend on the induced disturbance and material and are generally approximated by the superimposition of the first few fundamental frequencies (modes of vibration) of the material.

A shock wave, which is also a mechanical wave, excites all the fundamental frequencies of the material and travels as a discontinuity in which the material ahead of the shock front is in its initial state, and the material behind the front is in a compressed shock state. The amplitude, referred to hereafter as the shock stress, is on the order of a few hundreds of MPa to several GPa, and the rate of loading within the shock front exceeds a strain rate of $10^6$/s-$10^7$/s. This kind of loading can be created by a bullet impact, missile impact, or blast loading and has been of great significance in defense applications.

Shock physics has been an area of intense research dating back before the Manhattan project. However, major breakthroughs in the understanding of shock wave phenomena were due in large part to the advancements made in Los Alamos National Laboratory during that project and in parallel at Lawrence Livermore and Sandia National Laboratories. Since then, many different applications, from defense, to energy and space, to geothermal, have motivated and benefitted from continued research into shock physics. More importantly, probing the material's state under extreme loading conditions has become an integral part of shock compression research.

Experiments have been carried out by subjecting materials to shock loading by explosive detonation or by high velocity impact from a gas gun [2]. Both methods introduce a shock wave at the surface that propagates through the sample material and is followed by a rarefaction wave. The surface load that creates a shock wave is an impulse load of finite time duration reducing to zero at the end. Consequently, a rarefaction wave is created to satisfy zero stress at the free surface. The rarefaction wave is a tensile wave that follows the shock wave traveling in the same direction and unloads the material from the compressed shock state. Different points along the path of the rarefaction wave are at a reducing stress state, which results in the rarefaction wave having a fan-shaped structure.

When a propagating shock wave impinges on a material interface, a part is reflected in the parent material and a part is transmitted into the sample material. The reflected wave that travels in the opposite direction can be compressive if the new material has higher impedance. But, it can also be a tensile or an unloading wave if the new material has lower impedance compared to the parent material. The most common example for the latter is when the compressive shock wave impinges on a free surface. The new material being air with negligible impedance, the compressive shock wave is reflected in its entirety as an unloading tensile wave back into the parent material. The two unloading waves, rarefaction wave traveling in the direction of shock wave and the unloading wave from the free surface traveling in the opposite direction, interact to create high strain rate tensile loading at the plane of intersection. The tensile loading can be of sufficient magnitude for the material to fail and tear apart – a phenomenon known as spall of materials in shock wave studies.

It is well known that shock loading can be detrimental to a material's structural integrity. An important field of application examines how to increase the amount of energy

dissipation and reduce the shock stress as it propagates through the material. The information from shock studies has helped produce more effective armor as well as safer building materials. Nevertheless, the spall studies have remained an integral part of the shock wave research. Experimentally, it is used to determine the maximum tensile stress at which the failure occurs – known as spall strength of the material. Spall strength is different from the conventional tensile strength of the material. Tensile strength is determined by subjecting a stress-free material sample to tension with strain rate limited to a maximum of $10^3$/s. Spall strength is the tensile strength post shock compression in which the tensile strain rate exceeds $10^6$/s. Understanding of material failure due to spall can be used to make combined impact failure and momentum models to model trajectory and speed of the spalled portions of a material when it fragments. Another use can be to understand how the geometries of objects known to undergo shock loading can be changed to mitigate spall failure.

There are number of commercial software packages available today to simulate the material's response to shock compression. However, none of the software packages have a material model to simulate the spall failure post shock compression. The models available are based on cut-off pressure or cut-off stress. On reaching the specified cut-off value, the stresses in the particular element are reduced to zero in one step (instantaneously) or in a number of steps (gradually). Thus, these models can predict brittle or near brittle spall failure. However, there are a number of spall models available in the literature [3] which can be used in an existing code to model spall. They are invariably based on void nucleation, growth, and coalescence (VNGC) phenomena for ductile materials and crack initiation, growth, and coalescence for brittle materials with or without a rate effect. VNGC

models perfected by Seaman et al. [3] through extensive experiments and measurements of voids at different planes in recovered samples are based on the assumption of spherical void nucleation, their growth and coalescence leading to failure at the spall plane. However, with the advancement in the experimental techniques and characterization of the material itself, it is becoming increasingly obvious that void growth phenomena in ductile materials during the time of failure may not be spherical. Or, at least, there is a distinct indication that the void phenomenon is coupled with the grain boundary fracture and crack propagation.

It is important to note that failure mechanisms observed in recovered samples are late stage phenomena (after a couple of days). The entire process of spall occurs in a few tenths of micro-seconds starting from the instant that the two unloading waves meet to complete failure. There is no experimental evidence, to the best of the author's knowledge, showing the mode of failure in real time. However, it is prudent to assume that spall failure occurs by VNGC coupled with the grain-boundary fracture based on the failure observed in the recovered sample. But the fact remains that the parameters of the existing VNGC models alone can be tweaked to simulate the spall failure in agreement with the experimental data. What this suggests is that irrespective of the rigor of a VNGC model, it is important to model the rate of energy release and shaping of the compressive stress wave from spall plane which govern the pull-back velocity measured and recorded in experiments.

The motivation of the present work is to determine whether the VNGC model with grain boundary fracture can be coupled to predict the spall failure in agreement with the data. While this has not been attempted previously to the best of the author's knowledge,

the approach, if successful, will provide a much-needed tool to tailor the spall strength of materials to the phenomenological occurrences during failure. This thesis is focused on investigating the capabilities and limitations of a combined failure model for spall in 6061-T6 Aluminum.

This thesis is separated into six chapters. First a brief background of shock physics, computational modeling, and spall models is presented. Chapter 3 focuses the methods and results for 1D spall modeling using consistent material and model parameters. Using the results of the 1D spall modeling, the program, LS-DYNA is used with similar parameters to perform 2D spall modeling in Chapter 4. Finally, in Chapter 5, the 1D model is repeated with consistent geometry with respect to sample size, grain size, and grain distribution to present the effects of changing the material and model parameters.

# CHAPTER 2. BACKGROUND

## 2.1 Mechanics of Shock Waves

The first concept of shock wave mechanics is that there is a propagating wave that travels through the material as well as the particles in the material that transmit the wave. A common way to explain the difference between the speed at which the wave travels and the speed at which the particles in the material are travelling is by examining how fast a wave of water in a wave pool travels past a person in an inner tube. The wave travels past the person causing the inner tube to travel in the direction of the wave, however, the speed at which the person moves is not the same as the wave speed and the distance that the person travels is not the same as the wave's ultimate propagation.

The Rankine Hugoniot (RH) relations for a shock wave propagating as a discontinuity in an isotropic, homogeneous medium at rest, shown in Figure 1, are obtained by applying conservation of mass, momentum, and energy given in Equations 1-3, respectively.

Conservation of Mass: $$\frac{\mathrm{v_H}}{\mathrm{v_0}} = \frac{(U_s - u_p)}{U_s} \quad (1)$$

Conservation of Momentum: $$P_H = \rho_0 U_s u_p \quad (2)$$

Conservation of Energy: $$E_H - E_0 = \frac{P_H(\mathrm{v_0} - \mathrm{v_H})}{2} \quad (3)$$

where the variables $U_s$, $u_p$, $\rho_0$ are the shock velocity, particle velocity and initial density of the material, respectively. Equation 1 describes the volume ratio of a shock-state with respect to the original specific volume $\mathrm{v}_0 = 1/\rho_0$. Equation 2 describes the Hugoniot stress as a pressure $P_H$. Equation 3 shows a conservation of energy, $E_H$ being the specific energy, with respect to the shock properties. The initial density is measured prior to an experiment, and the particle velocity and shock velocity are measured using sensory devices during a shock experiment. However, if any two variables are measured in a different experimental method, the other variables can be determined by the Rankine Hugoniot relationships.

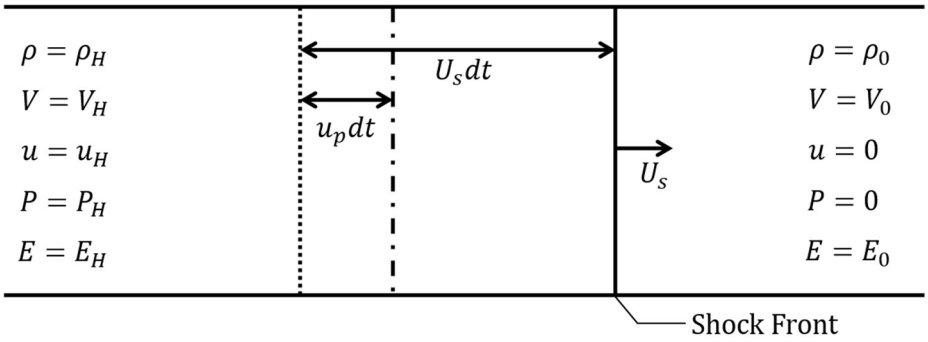


**Figure 1 – Hugoniot Relations where the material is in a shocked state to the left behind the shock front and the material is in its initial condition to the right in front of the shock front**

Figure 1 shows not only how the Rankine Hugoniot variables are related to shock, but also the difference between the shock velocity and the particle velocity. As seen in the figure, the distance that the particle travels is $u_p dt$ while the distance travelled by the shock wave in the same time is $U_s dt$.

Experimentally, the relationship between the shock velocity and particle velocity can be determined for different materials. The relationship was originally found using

explosive loading at very high shock stresses and was determined to be linear shown by Equation 4.

$$U_s = C_0 + Su_p \tag{4}$$

where $U_s$ and $u_p$ are measured during the experiment and $C_0$, the material speed of sound, and $S$, a material constant, are found as the offset and slope, respectively, of a linear regression of the measured particle and shock velocities [4]. Equation 4 is also referred to as a Hugoniot line.

The sound speed of materials at ambient conditions were also determined by acoustic methods and are defined by Equations 5-7.

$$C_L = \sqrt{\frac{K + \frac{4}{3}G}{\rho_0}} \tag{5}$$

$$C_S = \sqrt{\frac{G}{\rho_0}} \tag{6}$$

$$C_B = \sqrt{\frac{K}{\rho_0}} = \sqrt{C_L^2 - \frac{4}{3}C_S^2} \tag{7}$$

where $C_L$, $C_S$, $C_B$ are the longitudinal, shear, and bulk speeds of sound respectively. $K$ is the bulk modulus of the material and $G$ is the shear modulus of the material. It was found that Equation 4 could be fitted for most materials by establishing $C_B \approx C_0$, thus Equation 4 applies at high stresses when the shear strength of the material can be neglected.

However, the relationship was later found to deviate from a linear relationship at lower shock states, so the linear regression in Equation 4 fails to hold true as the effect of the shear strength can no longer be neglected at lower shock stresses. Thus, a majority of the material testing currently performed in the shock research community is outside of the linear range presented by Morris et al. [5]. Regardless, shock wave behavior will change based on changes in material properties if the particle velocity is unchanged.

Next, an equation of state (EOS) is required to determine the pressure of the Rankine Hugoniot state. The most commonly used version of the Mie-Gruneisen EOS, shown in Equation 8 [4], is applicable:

$$P(\mathrm{v}, E) = P_H \left(1 - \frac{\gamma\mu}{2}\right)(E - E_H) \tag{8}$$

where $\gamma$ is the Gruneisen coefficient, $\mu = \mathrm{v}_0/\mathrm{v} - 1$, and $P_H$ and $E - E_0$ are from the Rankine Hugoniot relationships in Equations 2 and 3.

Substituting Equation 2 into Equation 8 and using Equation 4 gives Equation 9,

$$P(\mathrm{v}, E) = \frac{\gamma}{\mathrm{v}}[E(\mathrm{v}) - E_0(\mathrm{v}_0)] + \frac{\rho_0 C_L^2 \eta}{(1 - S\eta)^2}\left[1 - \frac{\gamma}{2\mathrm{v}}(\mathrm{v}_0 - \mathrm{v})\right] \tag{9}$$

where $\eta = 1 - \mathrm{v}/\mathrm{v}_0$ [4]. The Mie-Gruneisen EOS is used when there is no phase change evident in the material as in the case of the 6061-T6 Aluminum investigated in this thesis. There are other EOS equations that are capable of relating pressure volume and temperature when there are phase changes present [6].

Another form of the Mie Gruneisen EOS applicable at lower shock stress is given as Equation 10 [7-9].

$$P = (K_1\mu + K_2\mu^2 + K_3\mu^3)\left(1 - \frac{\gamma\mu}{2}\right) + \frac{\gamma}{\mathrm{v}}E_m \tag{10}$$

where $K_1$, $K_2$, and $K_3$ are constant material properties defined in advance and $E_m$ is the specific internal energy. Equation 10 is used in order to update the hydrostatic stress based on volumetric strain and energy [9].

Another way to use Equation 10 is shown in Equation 11.

$$P = C_0 + C_1\mu + C_2\mu^2 + C_3\mu^3 + (C_4 + C_5\mu + C_6\mu^2)E_V \tag{11}$$

where $E_V$ is the internal energy per unit volume. The material constants $C_n$ are defined much like $K_n$ from Equation 10. Equation 11 is much easier to define the state curve as only the constants and original density is needed. Equation 11 is the version of the Mie Gruneisen EOS that is used in LS-DYNA.

It is important to note that the Mie Gruneisen EOS in Equations 8-11 defines the compressed shock state and gives a positive value for $P$ in compression. The mean stress is $\sigma_m = -P$. In addition, if the shock state is high enough, the EOS in Equation 8-11 completely defines the stress in the shock state. However, if the shock state is lower, then an addition strength model is required to determine the deviatoric component of the stress which is added to the hydrostatic stress to get the total stress.

## 2.2 Computational Modeling of Shock

Computational modeling is advantageous for studying shock response because it is very repeatable in comparison to shock physics experiments, which are complicated and yield limited data. A computational model for shock propagation and wave induced stresses works very similar to a computational fluids code, however there is an addition of the effect of the material's strength.

In evaluating the validity of computational results, the results can be compared to both the experimental results as well as analytical predictions. In the nodal time-history information, the peak amplitude of the stress in the direction of the wave propagation, $\sigma_{xx}$ (assumed to be positive in compression), is assumed to be the mean stress $P$ calculated by the EOS if the shock state is high enough for the material strength to be neglected. However, the total stress is found using Equation 12 if the shock state is low enough that the material strength cannot be neglected as is the case for the impact speeds investigated in this thesis.

$$\sigma_{ij} = \delta_{ij}\sigma_m + \sigma_{ij}' \tag{12}$$

where $\sigma_m = -P$ is the mean stress found using the EOS, $\sigma_{ij}'$ are the deviatoric stresses found using a material strength model, and $\delta_{ij}$ is the Kronecker delta.

The mean stress in Equation 13 [10] is given as,

$$\sigma_m = \frac{1}{3}\mathrm{tr}(\sigma) = \frac{\sigma_{xx} + \sigma_{yy} + \sigma_{zz}}{3} \tag{13}$$

For the shock wave propagating in an isotropic and homogeneous material under planar impact loading, the velocity gradients in the planes normal to the shock propagation are zero due to inertial confinement. This leads to $\varepsilon_y = \varepsilon_z = 0$ and $\sigma_{yy} = \sigma_{zz}$ giving the mean stress in Equation 14.

$$\sigma_m = \frac{\sigma_{xx} + 2\sigma_{yy}}{3} \tag{14}$$

The relationship above that $\sigma_{yy} = \sigma_{zz}$ is found whether a 2D or 3D simulation is carried out so long as the planar wave assumption holds. The assumption allows the equations to reduce to 1D greatly facilitating material model development. In addition, shear strains are still possible in 1D due to the presence of $\partial v/\partial x$ and $\partial w/\partial x$.

Since the material strength cannot be neglected, the deviatoric stresses must be calculated as well. The bilinear Von-Misses material strength model used in the simulation is seen in Equations 15a and 15b.

$$\Delta\sigma_{ij}{}' = 2G\Delta\varepsilon_{ij}{}' \tag{15a}$$

$$f(\sigma_{ij}, \varepsilon_p) = \sqrt{\frac{3}{2}\sigma_{ij}{}'\sigma_{ij}{}'} \leq \tau_y \leq \tau_y^0 + H'\bar{\varepsilon}_p \tag{15b}$$

where $G$ is the updated shear modulus based on the mean stress [11] and $\varepsilon_{ij}{}'$ are deviatoric strains found from the nodal displacements in Equation 15a. In Equation 15b, $\tau_y$ is the instantaneous yield strength, $\tau_y^0$ is the initial yield strength, $H'$ is the bilinear hardening

slope, and $\bar{\varepsilon}_p$ is the effective plastic strain. Essentially, if the left side of Equation 15b is larger than the right side, the material will start to flow.

The implementation of the material strength in Equation 15 with shock mean stress is shown in Figure 2.

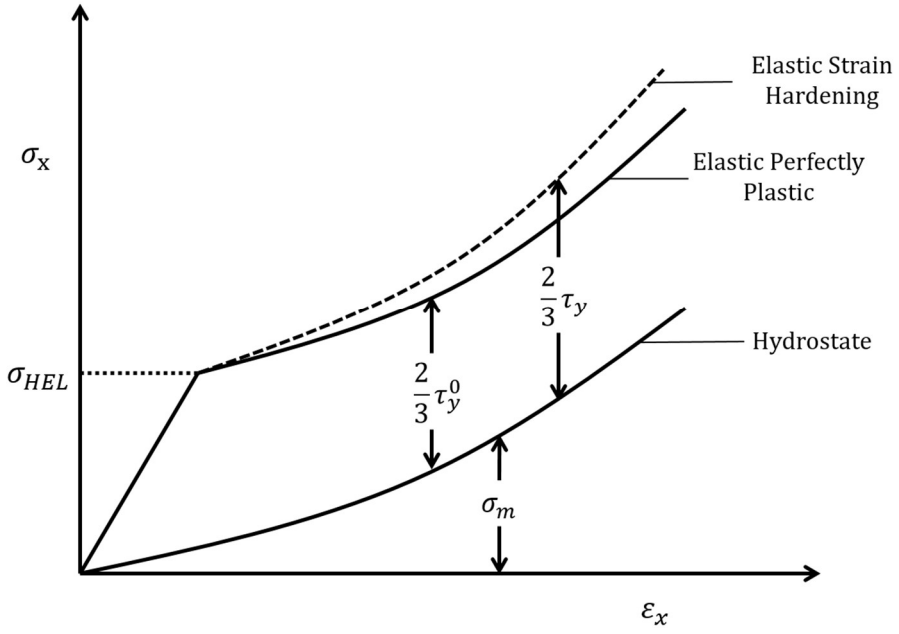


**Figure 2 – Stress-strain curve under a uniaxial-strain condition at low shock stresses [4, 12]**

Both the SHOCK-1D code used for 1D and LS-DYNA, used for 2D simulations, use an upgraded Lagrangian coordinate system, which is good for keeping track of the material as it moves in relation to itself. The alternatives, Eulerian coordinate mapping or Arbitrary Lagrangian-Eulerian (ALE), the method used in hydrocodes such as CTH [13], is advantageous for large deformations. Figure 3 shows high strain in both Lagrangian and ALE meshes. In the context of this thesis, where there is low strain in between nodes and no fragmentation, a Lagrangian coordinate system is used. This allows tracking nodal

history data distances with respect to the material's orientation, such as tracking the velocity of the free surface of the material.

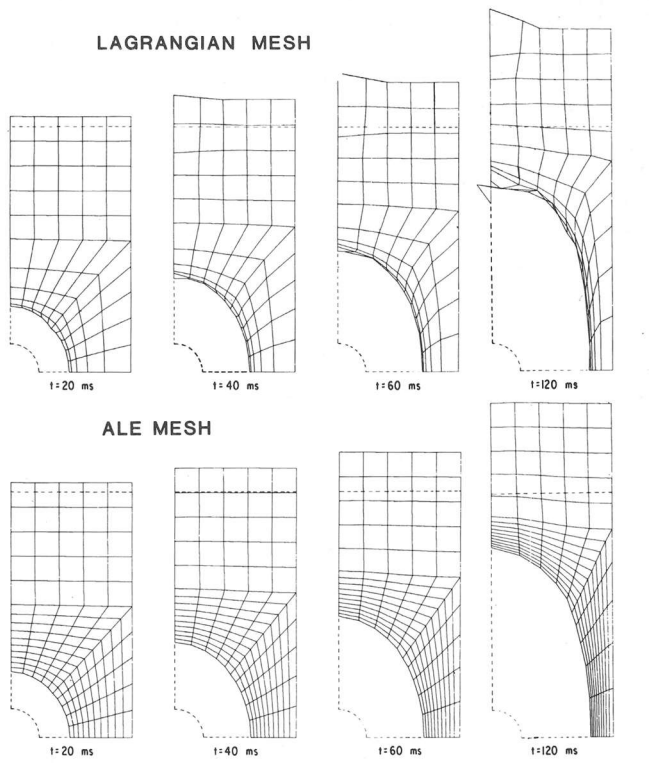


**Figure 3 – Comparison of response to high strain on Lagrangian Nodes (Top) to Eulerian-Lagrangian Remap Nodes (Bottom) [14]**

Lagrangian codes Shock 1D [15] and LS DYNA [16] used in this work integrate equations of motion by explicit method using variable time steps. For symmetric impacts, meaning that both the impactor and sample are the same material, the particle velocity for nodes on the impact surfaces right after impact can be set using Equation 16 or found by a contact algorithm.

$$u_p = \frac{V_i}{2} \tag{16}$$

where $V_i$ is the speed of the impactor. Prior to the impact, the speed of the sample is zero. Immediately after impact, symmetric shock waves travel through the sample and simultaneously back into the impactor. Even though the particle velocities are the same in both the impactor and the sample, the shock velocities are different due to the initial velocity of the impactor. However, when the impactor and the sample are different materials, the particle velocity at the impact surface is found using the continuity of velocity and stress. Thus, if the sample and impactor are of different materials, Equation 18 will not hold true because the particle velocity of the sample will be higher or lower than the result of Equation 18 based on the impedance of the impactor and the sample [4].

The two codes, SHOCK-1D and LS-DYNA, advance the solution in time by finding the velocity at $t + \Delta t/2$ from the known acceleration at time $t$. The velocity at $t + \Delta t/2$ gives the new nodal position at time $t + \Delta t$ after imposing contact constraints. The incremental strains at the mid-point are calculated and are used in the EOS to calculate mean stress and deviatoric stresses, which satisfy the Von-Mises flow rule. The total stresses after accounting for the artificial viscosity give the nodal forces at time $t + \Delta t$, used to calculate the nodal acceleration and advance the solution to the next time step.

During the simulations, the two codes provide outputs for state variables of all nodes and elements known as state outputs and variables for specified nodes and elements at specified time interval. The state outputs are used to spatially visualize the shock

propagation while nodal or element outputs are used to visualize temporal properties of shock variables.

A 1D simulation is quick in computational time and is fairly accurate for perfectly planar shock waves considering the entire cross-section of a material is experiencing the same stress and velocity. However, 1D simulations do have limitations compared to 2D and 3D simulations. Heterogeneities in the material prevent the shock wave from travelling in a perfectly planar manner, so the higher dimensional simulation is preferred for more accurate modeling of heterogeneous effects. In this case, 2D or even 3D simulations are the way to consider heterogeneities that can simultaneously lead to material failure perpendicularly to the wave direction.

## 2.3 Material Failure due to Shock

Spall due to wave propagation is a failure mode of material post shock compression. Spall is not an effect of compressive failure, but it occurs due to the interaction of release waves causing tensile loading leading to failure. It is a heterogeneous effect based on mesoscale defects in the material including voids, cracks, grain boundaries, etc. [17-19]. There are very few studies on spall that account for the mesoscale effects on spall. Most of the work relies on a phenomenological homogeneous continuum model. The major sources of spall highlighted in this thesis are the sources from void nucleation and growth as well as grain boundary failure due to damage.

Figure 4 shows a recovered Aluminum sample that has spall failure. As seen in the left image, the material has a planar region with voids. The image on the right shows a region with mainly crack separation.

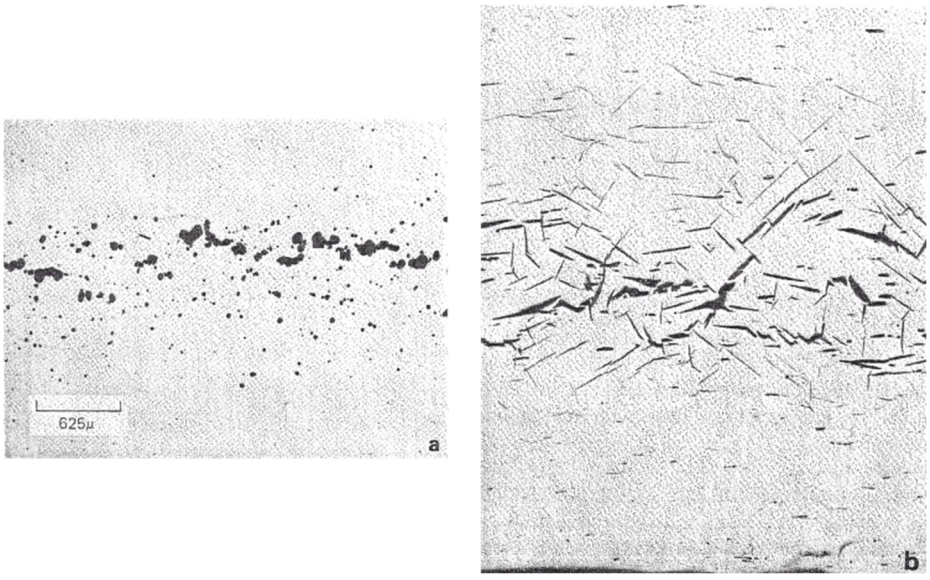


**Figure 4 – Failure due to void nucleation growth and coalescence (a). Failure due to crack propagation (b). [20]**

The two failure modes in Figure 4 can happen separately or simultaneously in the same sample and are the results of the same wave phenomena. Figure 5 displays a loading stress wave travelling through a 1D representative volume element (RVE), and Figure 6 shows how wave interaction leads to material failure.

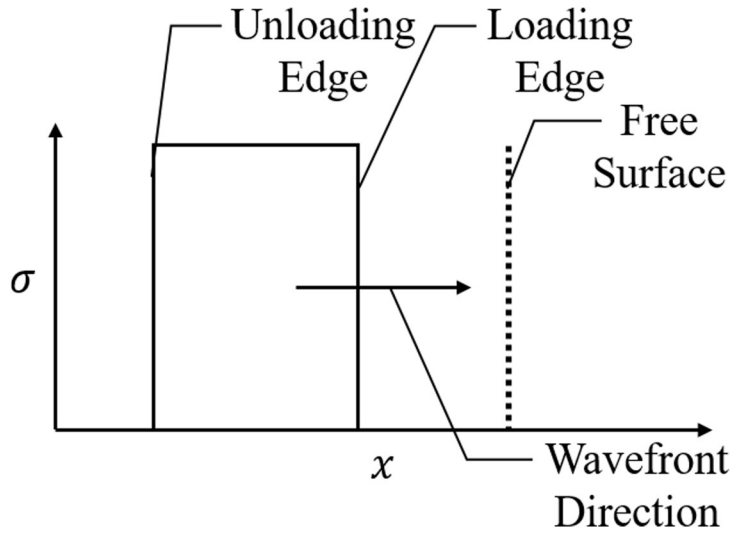


**Figure 5 – Stress wave travelling along material in the $+x$ direction**

In Figure 5, a stress wave with positive amplitude $\sigma$ causing compression is travelling through the material towards the free surface. In shock physics, it is shown experimentally that the compressive wave is followed by a rarefaction (unloading) wave. The rarefaction wave has a fan structure, but it is shown in Figure 5 with instantaneous unloading for simplified illustration purposes. Once the wave reaches the free surface, it reflects towards the $-x$ direction as seen in Figure 6 (a). For tensile loading to occur, two unloading waves will intersect and cause a constructive interference leading to a negative or tensile load, as seen in Figure 6 (b).

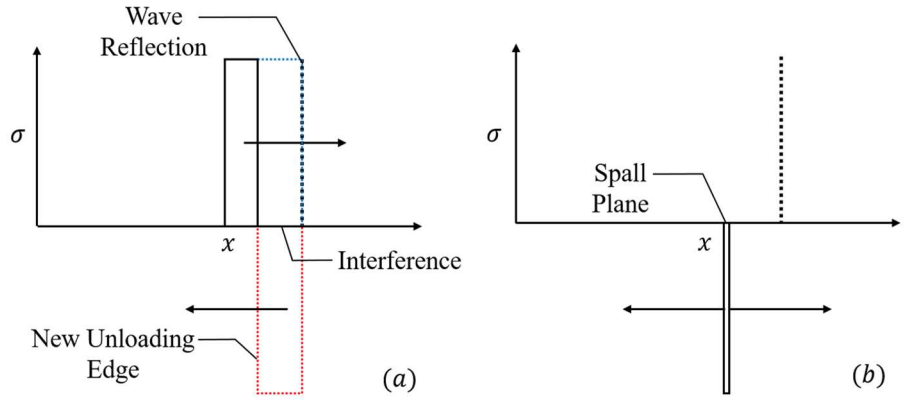


**Figure 6 – When two unloading waves intersect due to reflection off the free surface (a), there is a tensile wave created through interference with the original unloading edge (b)**

When the unloading waves compound due to interference, the resultant stress magnitude is $-\sigma$ if the magnitude of $\sigma$ is less than the spall strength. Spall occurs if the value of $\sigma$ exceeds the spall strength. In this thesis, a negative sign in the stress denotes that the material is in tension. The free surfaces created post spall failure have to be stress free. For this reason, compressive stress wave is created on the new surfaces which travel forward towards the free surface and backward in the sample.

The wave interaction phenomena is further shown in an $x$-$t$ diagram in the context of the plate flyer experiment in Figure 7.

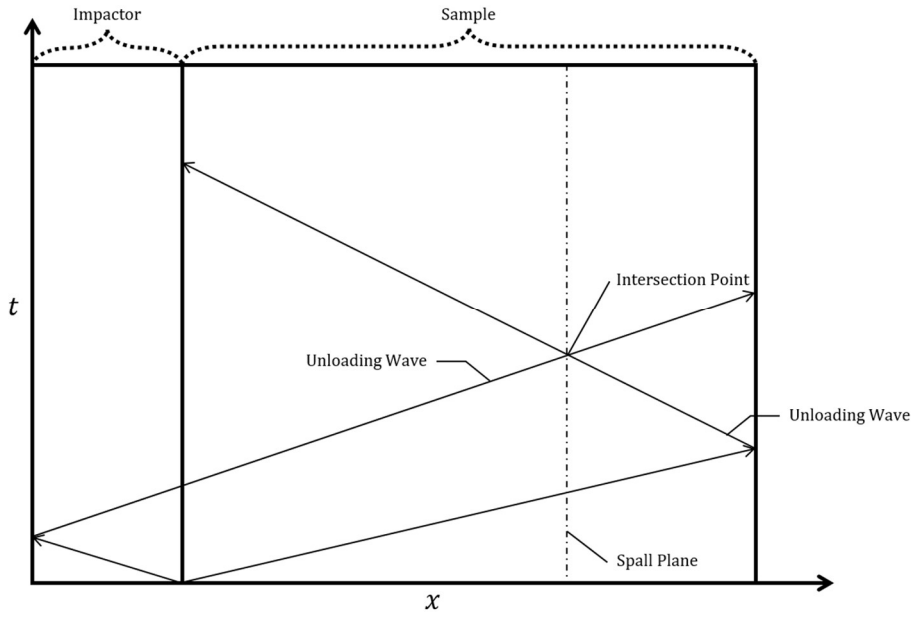


**Figure 7 – X-t diagram illustrating the wave propagation and creation of tension when the two unloading waves meet at the intersecting plane (point)**

As seen in Figure 7, the compressive waves will reflect off of each of the free surfaces of the impactor and of the sample. As they reflect, they become unloading waves as labelled. The spall plane occurs where the two unloading waves intersect at time $t$.

Experimentally, the spall phenomena cannot be observed with sensors that directly measure stress or strain inside the material due to the speed, nature of the wave interaction, and failure. An embedded sensor or a gauge fixed to the edge of the sample will not give useful data that correlates to the failure of the material along the planar spall zone in real time. To solve this problem, the spall phenomenon is observed implicitly and indirectly through the behavior of the free surface.

Figure 8 shows a generic schematic of the planar plate experiment generally used to perform the experiments and used in simulations in this thesis. The impactor disk impacts on the sample disk at high velocity. The impactor may or may not have a backing disk primarily used to support the impactor at very high velocity or to shape the rarefaction wave reflected from the impactor. Similarly, the sample may or may not have the window disk. The window is generally a high impedance material to study the sample unloading. The spall experiments in general do not use a window, or the window is a low impedance material used to shape the unloading wave from the sample.

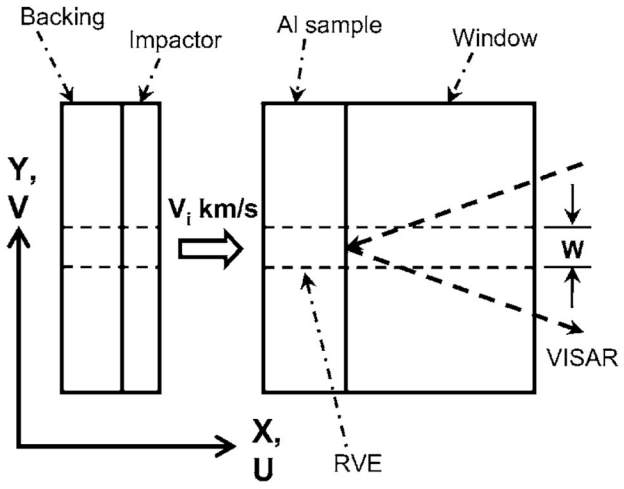


**Figure 8 – Schematic of a generic flyer plate experiment setup [11]**

Data is captured using a VISAR laser pointed at the free surface of the impacted sample. Thus, only the time-variant position and velocity information can be taken from a single point on the free surface. The spall data collected by the VISAR experiment for the Aluminum 6061-T6 can be seen in Figure 9 and Figure 10 for the .5km/s and 1.3km/s impact velocity cases, respectively [2].

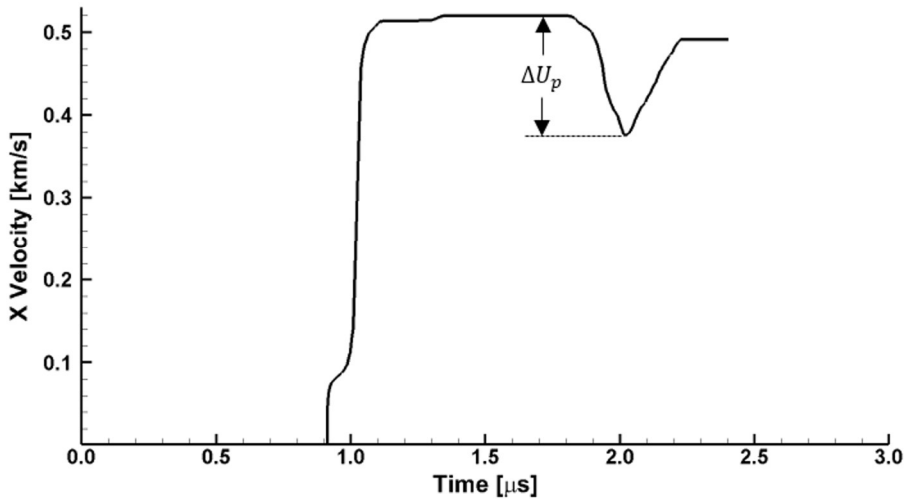


**Figure 9 – Free surface velocity data from .5km/s impactor experiment. The "V" shape in the curve from 1.75μs to 2.25μs is a pullback phenomenon caused by material failure [2]**

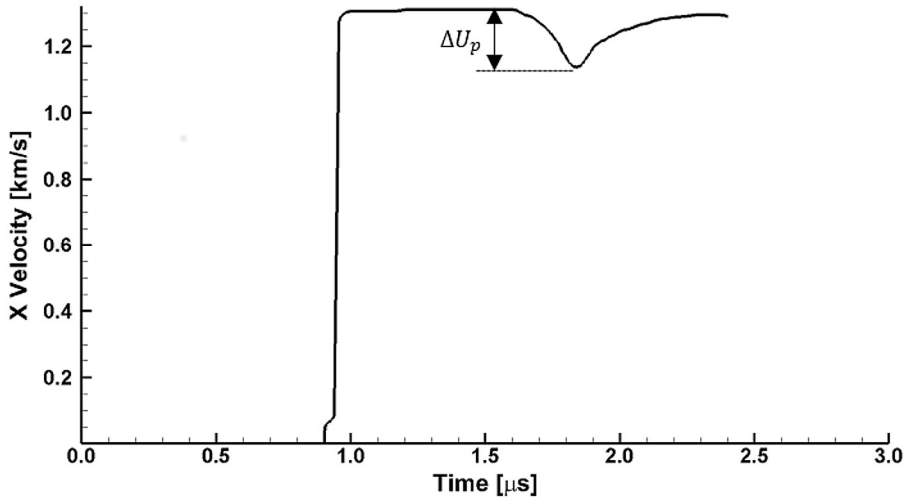


**Figure 10 – Free surface velocity data from 1.3 km/s impactor experiment. A similar pullback signal to the .5km/s case is observed [2]**

The free surface gains velocity and attains the plateau when the shockwave reaches the free surface and is reflected as the release wave. The velocity starts reducing on the arrival of the unloading wave from the impactor side. If the material was not failing, the unloading pulse would cause the free surface velocity to drop all the way to zero. However,

if the material fails and spall occurs in the sample, the material separates at the spall plane and a compressive wave is generated at the spall plane. This compressive wave, on reaching the free surface, starts increasing the velocity of the free surface. The pullback velocity, $\Delta u_p$, shown in Figure 9 and Figure 10 is used to calculate the spall strength using Equation 17.

$$\sigma_{spall} = \frac{\rho_0 C_L \Delta u_p}{2} \tag{17}$$

where $\sigma_{spall}$ and $\Delta u_p$ are the spall strength and pull-back velocity shown in Figure 9 and Figure 10 [18].

As mentioned earlier, there are number of spall damage models with a varying number of parameters. The values of the parameters are generally found by tweaking them based on attempting to match the simulation free surface velocity to the free surface velocity experimental data due to the absence of data on real time failure. Moreover, the VNGC model can alone simulate spall failure in agreement with data even though the failure observed shows coupling with grain boundary fracture. Due to these difficulties and discrepancies, three spall models were chosen with a minimum number of parameters to arrive at a combined failure model with relative ease.

### *2.3.1 Cochran Banner Model for Spall Failure*

The first spall model studied in this thesis is the Cochran-Banner Damage model [17, 18] in the SHOCK-1D code. The model defines spall failure based on an ultimate

damage parameter and on the rate at which the damage parameter is reached during failure. Equation 18 shows how the damage parameter is found.

$$F = 1 - \left(\frac{D(x,t)}{D_0}\right)^{2/3} \tag{18}$$

where $F$ is the damage parameter which varies from one for intact material to zero for complete failure or spall. $D$ is the void opening or void diameter calculated after spall strength is reached in the material. $D_0$ is the void opening at complete spall. The larger the value of $D_0$, the longer it will take to reach the ultimate damage criteria [18]. After reaching the spall strength Σ, the longitudinal stress is calculated using Equation 19.

$$\sigma = F\Sigma \tag{19}$$

where σ and Σ are the stress normal to the failure plane and the spall strength parameter based on the material experimental data [18].

The relationship between the tensile stress and the growing void size following the Cochran Banner model is shown in Figure 11.

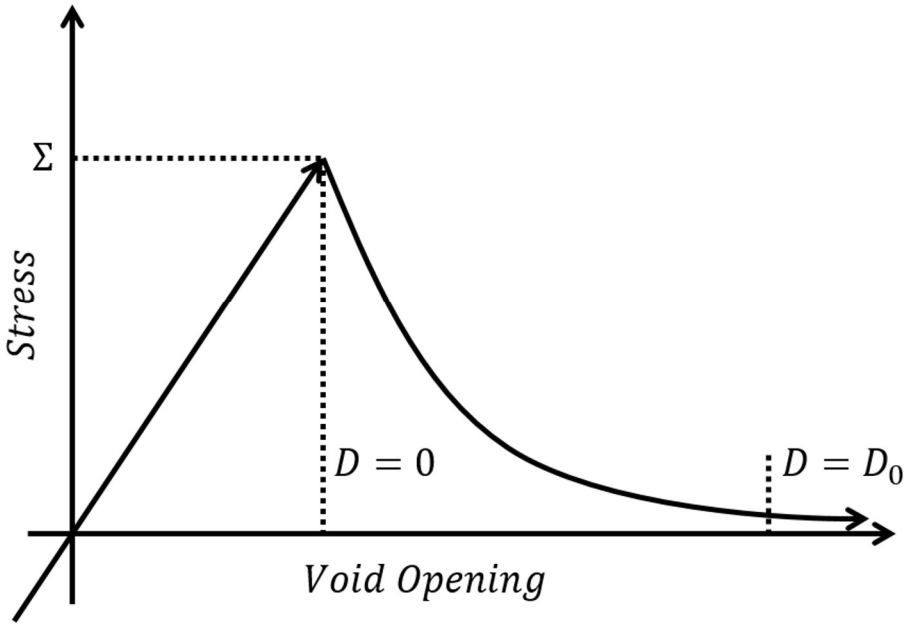


**Figure 11 – The amount of tensile stress that the material can sustain peaks at Σ and then reduces until it reaches the maximum separation of $D_0$**

The main assertion of the Cochran-Banner model is that as the material is failing, the tensile stress that the material can ultimately undergo reduces. Once the material fails, the stress the material can maintain through the spall plane becomes zero. The advantage of this model is that it only requires the optimization of two failure parameters and that these two parameters can be used to model both brittle and ductile materials undergoing shock loading.

The Cochran Banner model calculates stress post spall initiation which is defined at the element's integration points, located at the center of the 1D elements in this case. Hence, the failure defined by the model is the element failure or intra-grain failure.

### *2.3.2 Cohesive Element Model for Spall Failure*

In fracture mechanics, cohesive elements can be used to simulate crack propagation. Cohesive elements, embedded between two grains at their boundaries, are elements in computational modeling that initially have zero volume. Once the material undergoes tensile loading, the volume begins to increase. As the volume increases, there is a larger nodal force that attempts to pull the nodes back together. While 2D cohesive elements have been used in previous spall work, the present work used 1D cohesive elements for the first time for the purpose of spall simulation. In 1D, cohesive elements are zero volume elements comprised of 2 nodes. In 2D, cohesive elements are zero area elements comprised of 4 or more nodes. Figure 12 shows the geometry and behavior of cohesive elements in 2D. Cohesive elements are used to simulate crack propagation and grain boundary failure by modeling the grains as multi-edged surfaces with common node locations along the edge.

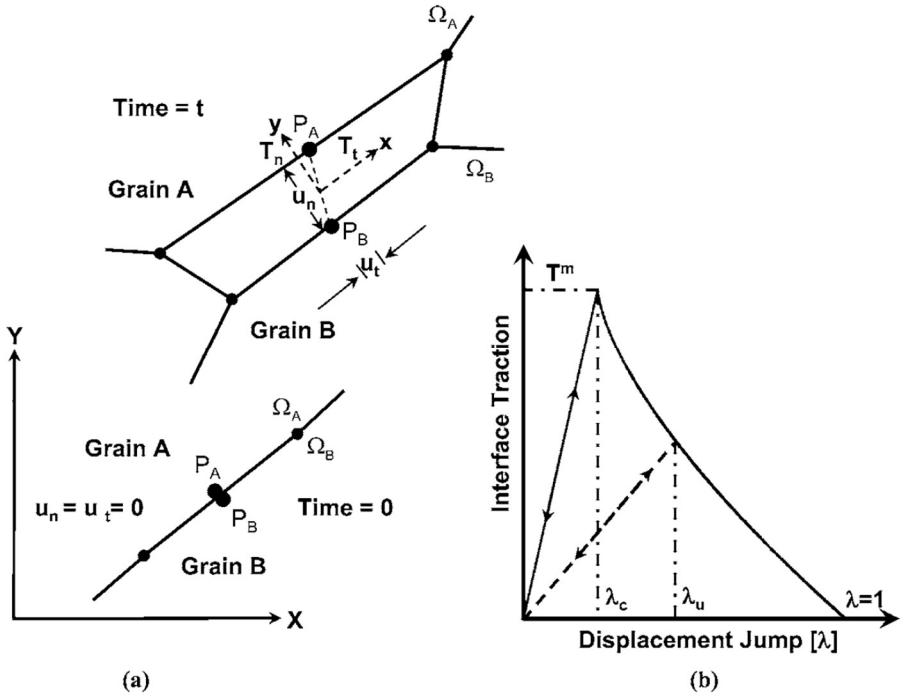


**Figure 12 – A 2D four node cohesive element described at time $t_0$ and at time $t$ (a). The traction displacement triangle described by the maximum traction $T^m$, the critical distance $\lambda_c$ and final distance $\lambda$ (b)**

Cohesive elements also impose reactionary forces to prevent "hourglassing", or negative volume, in compression. The elements impose a reactionary force that prevents expansion in tension as a function of the stiffness assigned to the element, which is the maximum traction $T^m$ divided by the critical distance $\lambda_c$. Once the element nodes reach a maximum relative displacement $\lambda$, the element is eroded and the surfaces are permitted to move apart freely with no transmitted stress.

Figure 11 and Figure 12 show that the cohesive element formulation and the Cochran Banner model in 1D are phenomenologically similar. The difference is that the cohesive model applies to specific nodes and thus models inter-grain failure while the Cochran Banner model applies to elements, modeling intra-grain failure.

### *2.3.3 Jim Johnson VNGC Model for Spall Failure*

The third spall model studied in this thesis is the Jim Johnson model, a simple void nucleation, growth, and coalescence (VNGC) model [19]. There are many VNGC models available and the Lynn Seaman model is the most prolific, however the Jim Johnson model is much simpler and has fewer variables, which is why it was chosen for this study.

The VGNC model assumes, in the unstressed state, that there are initially micro voids with an original void pressure that may or may not be zero. Figure 13 shows that as the pressure around the voids decreases in the hydrodynamic tensile loading phase of spall plane creation, the void size increases due to the pressure differential between the outside pressure and the pressure the void can support internally due to plastic yielding. The failure happens when the voids grow to a large enough size and coalesces along the spall plane, that the material becomes discontinuous, and thus the sample cannot sustain tensile stress.

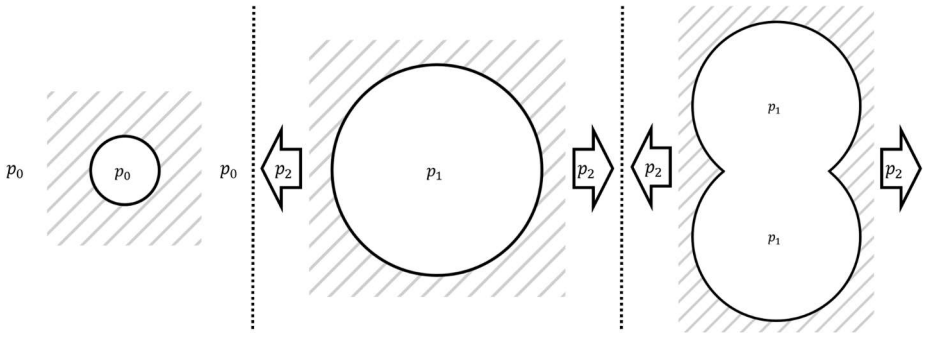


**Figure 13 – A pre-existing void at $t_0$ with internal pressure $p_0$ and external pressure $p_0$ (Left). At time $t$ the external pressure $p_2 < p_1$ so the void grows as the material is in tension (Center). The void coalesces at $t_f$ with another void along the spall plane as the porosity goes to the limit leading to material failure (Right)**

As seen in Figure 13, it is important to note that all the stages are shown where the void is in tension. The VNGC model is not a failure model when the material is in

compression. When the shock state is in a compressive state, the void size is reduced. The voids will not disappear completely, however, but the porosity of the overall material is greatly reduced in the compressed region. The porosity will increase if the region goes into a tensile loading case. For this thesis, $p_0 = 0$.

The amount of void presence in a metal such as 6061-T6 Aluminum can be a result from the manufacturing-related pre-stresses of the metal due to inclusion cracking on the microscale [21-23]. The porosity can be written in relation to the distention of the material seen in Equation 20 [2].

$$\phi = 1 - \frac{1}{\alpha} \tag{20}$$

where ϕ is the porosity and α is the distention of the material.

The model gives the critical pressure for the void to grow or collapse in Equation 21 [19].

$$P_{eq}(\alpha) = \pm \frac{a_s}{\alpha} ln \frac{\alpha}{\alpha - 1} \tag{21}$$

where $a_s$ is the material stress parameter and $P_{eq}$ is positive for compression and negative in tension.

For $\Delta P = P - P_{eq}$, the void will grow in tension if $\Delta P$ is negative and collapse in compression if $\Delta P$ is positive. The corresponding change in distention is found in Equation 22.

$$\dot{\alpha} = -\frac{\alpha^2(\alpha-1)}{\eta}\Delta P\left[\alpha\left(\frac{\alpha-1}{\alpha_0-1}\right)^{\frac{2}{3}} - (\alpha-1)\left(\frac{\alpha}{\alpha_0}\right)^{\frac{2}{3}}\right] \quad if\ \Delta P\dot{\varepsilon}_{\mathrm{v}} < 0 \qquad (22a)$$

$$\dot{\alpha} = 0 \quad if\ \Delta P\dot{\varepsilon}_{\mathrm{v}} \geq 0 \qquad (22b)$$

Pressure, $P$, is given by the Mie Gruneisen EOS of Equation 10 in compression and in tension, it is given as Equation 23.

$$\dot{P} = K_1\left(\dot{\varepsilon}_{\mathrm{V}} + \frac{\dot{\alpha}}{\alpha}\right) + \frac{\gamma}{\mathrm{v}}\dot{E}_m \qquad (23)$$

Where the cohesive element damage model is applied at the grain boundary, the Jim Johnson VNGC model is applied to the region inside of the grain. Thus, inter and intra grain failure can be observed by each failure model respectively.

## 2.4 Effect of Material Properties on Shock Response

In using a homogeneous assumption, the shock wave will propagate in a perfectly uniform planar manner. Thus, a 1D simplification can be made that the shock wave will travel along a single vector direction and that all particle velocities will also be along the vector of travel. As seen in Equation 7, the bulk properties affect the material response to shock loading in the homogeneous case.

In reality, a homogeneous material does not exist. Focusing on the mesoscale, the bulk properties and homogeneous assumption about the material for the entire length is no longer possible as discontinuities must be input to replicate the structure to show how the

complex mesoscale structure responds to shock compared to a macro scale homogeneous model. Thus, mesoscale heterogeneities are imposed.

Some of the possible heterogeneities that can be studied in their shock response are the presence of voids, grain boundaries, alloyed inclusions, and defects. Computationally, it is possible to include these heterogeneities in a mesoscale material model or by use of mesh geometries.

Porosity can be present in a continuous material in the form of voids that are left over from manufacturing or machining. They affect the material's density and integrity in certain areas of the material leading to a loss of isotropy.

Grain boundaries have a different strength and cohesion properties compared to the strength and cohesion of the lattice inside the grains. The isotropy of a metal can be informed by the material behaviour during loading on a macroscale. However, the mesoscale heterogeneities can inform better macroscale phenomenological models.

## 2.5 Shock Response of Sand

Sand is a granular material that can sustain a propagating shock wave. The purpose of investigating sand is so that a simpler model for 2D grain interaction could be performed prior to a 2D granular spall study for 6061-T6 Aluminum in LS-DYNA.

Research on shock response of sand is commonly done because of its relevance for space and geomechanical applications. Many of the experimental procedures for impact loading of sand are similar to the flyer plate experiment. One method is to fire a light projectile into a sandbox from a vertically oriented position and then to examine the

geometry of the crater after the collision. Another method is to fire a projectile into a sand sample that is horizontal with a strain gauge imbedded inside [24-26].

Sand has been reviewed for its shock response properties and the studies have shown that the porosity of compacted sand affects the shock response on both the micro scale as well as the mesoscale. On the microscale, there are surface reverberations and shock wave refractions that affect the energy of the wave front as it travels through a sample [26]. Because of the microscale responses, there can be pressure concentrations that correlate to higher temperatures than sand can sustain. For the purposes of the granular study in this thesis, temperature effects were ignored because the impactor speed was sufficiently small enough that the phase change temperature was assumed to not be reached.

## 2.6 Model Calibration

Once the model is implemented, the next step is to ensure that the parameters in each model have the best values that replicate the real-world behavior of the material. The importance of this step with respect to this thesis is that the combined failure model has yet to be implemented. While there are many parameters that affect the performance of both the material failure model as well as the characteristic material properties, different parameters need to be isolated to determine not only how they affect the simulation, but also to what degree they affect the simulation. The reason the failure models studied in this thesis were chosen is that they each have a small number of variable parameters. Thus, they are easier to isolate for understanding how the simulation is affected. The parameters studied in this thesis are Σ and $D_0$ for the Cochran Banner model. The parameters studied for the cohesive element failure model are $T_m$, $\lambda_c$, and $\lambda_u$. The parameters for the Jim Johnson VNGC model are $\alpha_0$, $a_s$, and $\eta$.

The models are first implemented in simulations with "best guess values" based on values from previous work for plate impact simulations for Aluminum 6061-T6 [11]. Once the initial values are implemented, the values of each parameter are altered to understand whether the behavior of the model can be optimized to match the data mode closely.

The experimental data shown in Figure 9 and Figure 10 is compared to the outputs from a single simulation. Each simulation corresponds to a single set of failure parameter values. Once a way to compare the result of the single simulation to the experimental data is developed, a function describing that relation can be created as seen in Equation 24.

$$\{f(\theta_1, \theta_2, \dots \theta_n)\} \tag{24}$$

where $f$ is the function to be minimized or objective function, $\theta$ is a parameter in the model, and $n$ is the number of parameters in the model.

The objective function is prescribed based on the desired behavior of the model. Thus, two objective functions for the material failure models were used. The first objective function was the model free surface profile compared with the experimental data free surface profile. The second objective function compares the absolute spall strength of the model to the absolute spall strength of the experimental data neglecting the profile of the free surface.

### *2.6.1 Calibration with Respect to Pull-back Profile*

The first step is to develop an objective function. To compare profiles, the area between the two curves is found numerically. Thus, the objective function will look like Equation 25.

$$\{f(\theta_1, \theta_2, \dots \theta_n)\}_T = A_T \tag{25}$$

where $A_T$ is the area between the two curves with respect to the $n$ parameters in a specific combination $T$.

To calculate $A_T$, the area between the curves is shown in Equation 26.

$$A_T = \int_{t_0}^{t} |v_m(t) - v_e(t)| dt \tag{26}$$

where $v_m(t)$ is the free surface velocity found using the model parameters in Equation 25 and $v_e(t)$ is the experimental free surface velocity.

A simple method for evaluating the integral in Equation 26 was developed to easily be scripted so that many combinations for the parameters could be evaluated. Numerically, the absolute value of the integrated area is found using a variation of the trapezoid method for integration. The method is instead the sum of the triangular areas formed by using the points in each curve as seen in Figure 14.

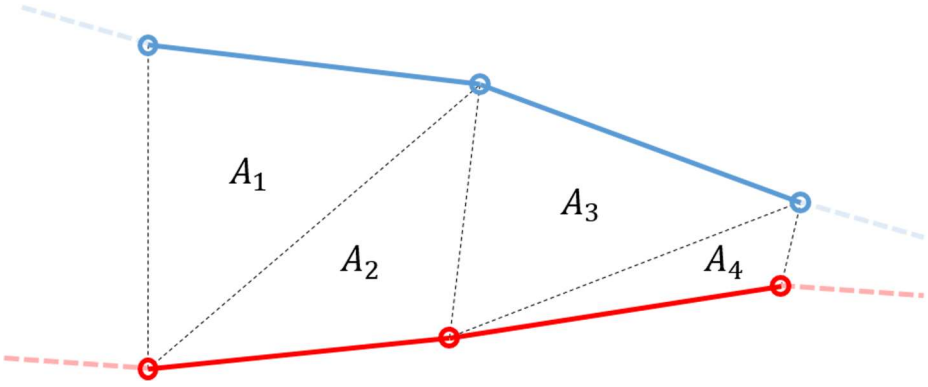


**Figure 14 – Triangles formed between curves**

In Figure 14, the first triangle is defined by the first two points of the data curve (blue) and the first point of the simulation curve (red). The second triangle is defined by the first two points of the simulation curve (red) and the second point of the data curve (blue). The advantage of using this method is that there is no interpolation required to

ensure that each y value corresponds to the same x values. Instead, the only requirement is that there are the same number of points along both curves.

There are fewer data points in the experimental data, so the simulation data is truncated and indexed to have the same number of points along the same range. The area for each triangle is found using Equation 27.

$$A_n = \left| \frac{1}{2} Det \begin{pmatrix} x_1 & y_1 & 1 \\ x_2 & y_2 & 1 \\ x_3 & y_3 & 1 \end{pmatrix} \right| \tag{27}$$

The absolute value of the area from $A_0$ to $A_n$ is summed to find the total area between the curves.

### *2.6.2 Calibration with Absolute Spall Strength*

The second objective function is the absolute difference in the pullback velocity, meaning the difference between the maximum velocity and the minimum velocity in the pullback range. The objective function for this method can be seen in Equation 28.

$$\{f(\theta_1, \theta_2, \ldots \theta_n)\}_T = \left[\Delta u_p^m - \Delta u_p^e\right]_T \tag{28}$$

This objective function is distinctly different than the objective function of the area between the curves because the objective function in Equation 28 can be minimized with different values than the minimum values of the objective functions in Equation 25.

Once many trials have been run, both objective function values are normalized from zero to one and thus they can be compared. The method for comparison is seen by using Equation 29.

$$F = rf_1^m + (1 - r)f_2^m \tag{29}$$

where $r$ is a percentage from zero to one and $f_1^m$ and $f_2^m$ are the normalized minimum objective functions. Depending on the value of $r$, the weight of the total objective function will skew more towards either the profile objective function or skew towards the spall strength objective function.

# CHAPTER 3. OBJECTIVE

The present work examines spall phenomena in Aluminum 6061-T6 during planar plate impact experiments through a computational approach. Through the computational efforts, the thesis can be broken into two major objectives. First, each of the currently available intra-grain failure models, Cochran Banner, and Jim Johnson VNGC model, and inter-grain failure cohesive model are used to predict spall response using the SHOCK-1D Code. The second objective is to effectively combine the VNGC and cohesive model to predict spall under a combined spall failure model.

The SHOCK-1D code is used to replicate the experimental results for Aluminum 6061-T6 including both the homogeneous assumption without failure to affirm phenomenologically correct material behavior as a response to planar shock loading. Next, each of the failure models are implemented separately and compared to the experimental results for flyer-plate experiments at .5km/s and at 1.2km/s.

The second objective is the major contribution of this thesis, as it is the first implementation of a computational study of simultaneous failure modeling for spall. The combination of the two failure models is expected to alter the best-fit model parameters of the separate failure models, and thus an investigation of the values of these parameters is needed to determine both the feasibility and accuracy of a combined failure model.

In addition to the two objectives using SHOCK-1D code, the additional goal of this thesis is to evaluate the new features of automatic contact and cohesive elements in LS-

DYNA for 2D simulation by simulating shock response of sand to evaluate automatic contact and simulating spall failure to evaluate cohesive formulation.

# CHAPTER 4. 1D SHOCK SIMULATION RESULTS AND DISCUSSION

## 4.1 Methods for 1D Impact Simulation

The schematic of a generic planar plate impact experiment used for 1D simulations is shown in Figure 15. In the figure, different bodies correspond to physical bodies used in the gas gun experiment. Thus, in order to replicate the experimental data, the geometry of the simulation must directly correspond to the experimental setup. As discussed, the impactor body, $B^2$, may not have the backing body, $B^1$ , because the backing body is only added if the impact velocity is high enough to require the backing to preserve the impactor integrity. The spall experiments discussed below do not have the window, $B^4$, but the window body has been used in a different simulation, which is further discussed below. 1D simulations were carried out using the SHOCK-1D code [15]. The input file needs to include the length of each material, their initial velocity, their material number, and the merged condition ($M^1$ to $M^3$) and the number of nodes. If the merged parameter of two consecutive bodies is the same, then the two bodies are merged at their interface; the contact algorithm is not used and the two bodies cannot separate. If the merged parameters are different, a contact algorithm is used and the two bodies can separate. Further inputs required are the material model to be used and material properties for each distinct material number. Other parameters needed are artificial viscosity, node and element numbers of output files and time intervals for node, element, and state outputs.

First, the geometry for the 1D simulation is created using conventions shown in Figure 15.

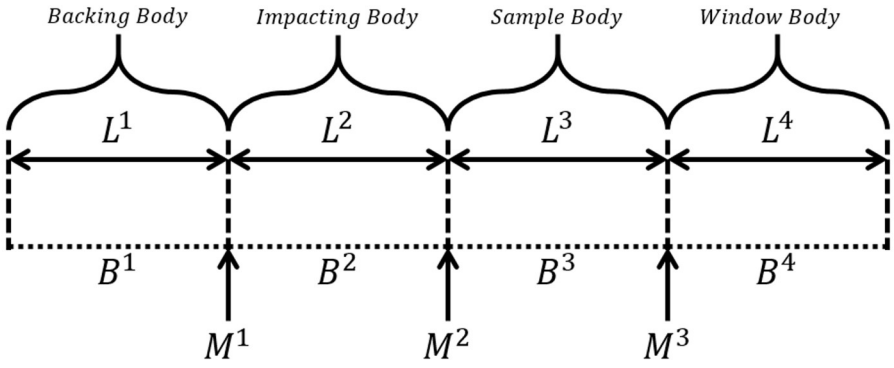


**Figure 15 – Schematic of a generic planar plate impact experiment used in 1D simulations**

For each of the different configurations simulated, the properties of each material remained constant. The parameters for the SHOCK-1D code for the Aluminum 6061-T6 symmetric impact are given in Table 1. Table 1 can also be found in Appendix A as Table A.1 along with the values for other material properties used in the 1D simulations including Z-Cut Quartz in Table A.2, Lithium Fluoride in Table A.3, and Lexan in Table A.4.

**Table 1 – Parameters used for 1D simulations that correlate to Aluminum 6061-T6**

| Material Parameter | Symbol | Value | Unit |
|---|---|---|---|
| Density | $\rho_0$ | 2.703E+03 | kg/m$^3$ |
| Linear Artificial Viscosity | $A_L$ | 3.000E-01 | |
| Quadratic Artificial Viscosity | $A_Q$ | 2.000E+00 | |
| Shear Modulus | $G_0$ | 2.993E+10 | Pa |
| Yield Stress | $\sigma_Y$ | 3.240E+08 | Pa |
| Hardening Coefficient | $H$ | 1.050E+09 | Pa |
| Ultimate Yield Stress | $\sigma_U$ | 1.000E+20 | Pa |
| **EOS Parameter** | | | |
| Coeff 0 | $K_0$ | 7.116E+10 | Pa |
| Coeff 1 | $K_1$ | 0.000E+00 | Pa |
| Coeff 2 | $K_2$ | 1.584E+11 | Pa |
| Coeff 3 | $K_3$ | 9.235E+10 | Pa |
| Gruneisen Coefficient | $\gamma_0$ | 2.000E+00 | |

There are two output options for the plots generated by the SHOCK-1D code. The first option is plotted as a snapshot of all the nodal and element data from a given time interval as a function of $x$, or horizontal position in a Lagrangian coordinate system. The second option, nodal output, is plotted as a time history data of a Lagrangian coordinate that moves relative to the material as a function of $t$. The nodal time history data is presented in this thesis as it can be directly compared to the data from the VISAR experiment. The stress history is plotted for the element to gain insight into the temporal variation of the in-situ stress.

## 4.2 1D Simulation of Symmetric Impact Without Backing and Window

The first 1D simulation was performed without an impactor backing, $B^1$, and window, $B^4$. There was just an impactor body, $B^2$, impacting on a target body, $B^3$. The values corresponding to the geometric configuration of this simulation is shown in Table

2. The purpose of this simulation was to gain insight into the shock wave propagation with unloading but without failure. These results were also compared with the 2D simulation discussed in Chapter 5.

**Table 2 – Geometric values for 1D homogeneous simulation with no material failure model with an impactor at .5km/s**

| Body | Material | Length [mm] | $V_i$ [km/s] | Merge Setting |
|---|---|---|---|---|
| $B^2$ | 6061-T6 | 1.000 | 0.500/1.300 | 1 |
| $B^3$ | 6061-T6 | 3.000 | 0.000 | 2 |

The nodal and elemental time-history data for different nodes and elements along the geometry was output every 1.0E-15s and is shown in Figure 16 and Figure 17 for the impact velocity of 0.5km/s.

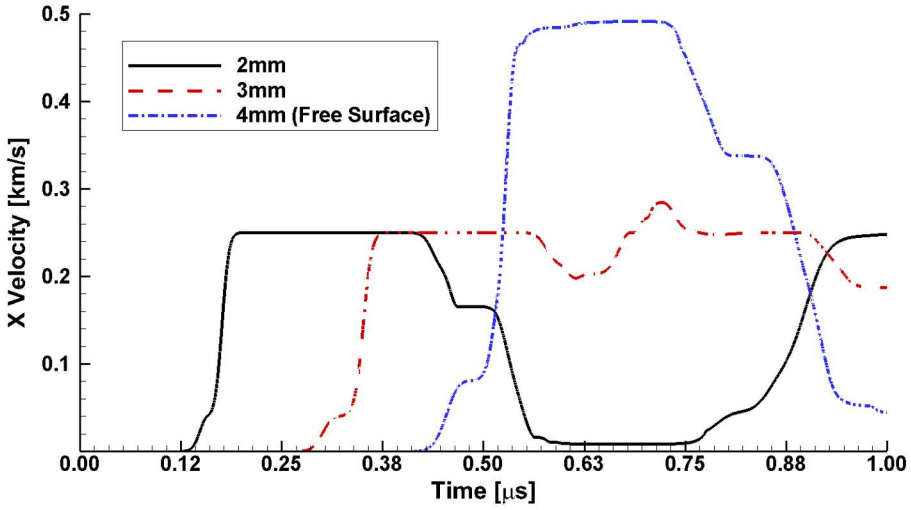


**Figure 16 – X Velocity nodal time history data for nodes at 2mm, 3mm, and 4mm along the target with 0mm being the beginning of the .5km/s impactor**

The 2mm and 3mm nodes reach a peak velocity of .25km/s and the free surface reaches a speed of .5km/s, which is expected because the reflective velocity wave behavior boundary condition.

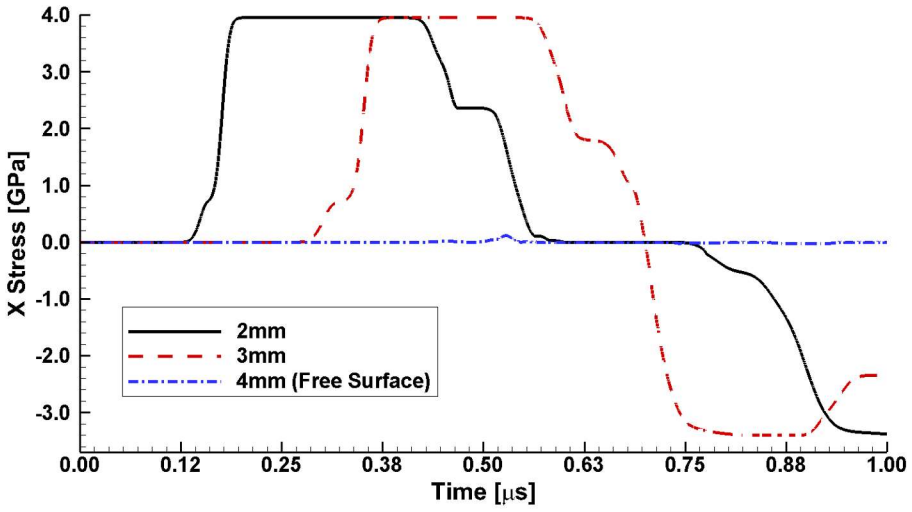


**Figure 17 – X Stress elemental time history data for nodes at 2mm, 3mm, and 4mm along the target**

There is virtually no stress at the free surface, 4mm, which is what is expected as the free surface must be traction free, the condition that generates the reflected stress wave unloading the target. More importantly, Figure 16 and Figure 17 show the elastic wave followed by the plastic wave propagating in the material. As the reflected unloading wave from the target free surface interacts with the unloading wave from the impactor the material goes into tension as seen at the 3mm element in Figure 17. The magnitude of maximum tensile stress is comparable to the maximum compressive stress due to the absence of a failure model.

Next, the same geometry as that in Table 2 was repeated for impact velocity of 1.3km/s. The results from the 1.3km/s symmetric homogeneous impactor can be seen in

Figure 18, which shows the time-history nodal velocity and Figure 19, which shows the time-history elemental stress data.

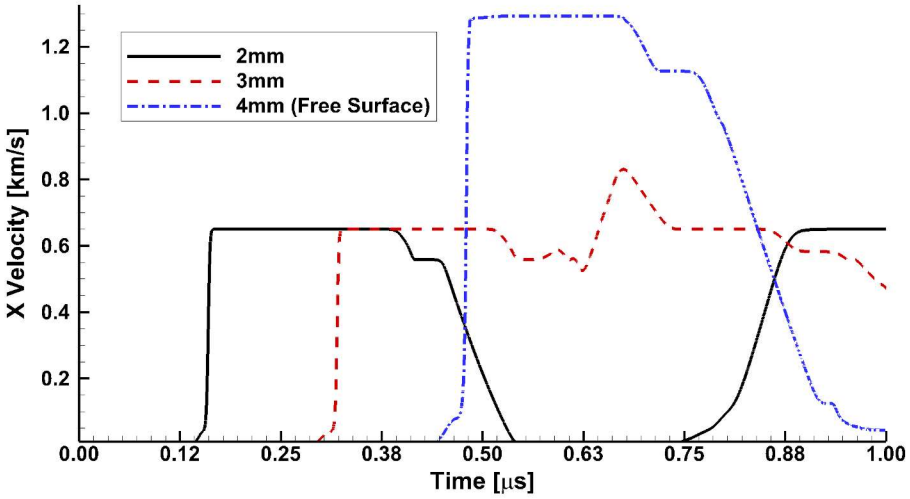


**Figure 18 – X Velocity nodal time history data for nodes at 2mm, 3mm, and 4mm along the target with 0mm being the beginning of the .5km/s impactor**

The nodal velocity data from the same geometry with a higher impact speed shows the same type of profile due to the same homogeneous material properties. However due to the higher impactor speed, the peak velocity is higher and the time to the peak velocity is shorter because the shock wave speed is higher due to Equation 2. Additionally, there is no evidence of the elastic wave. The elastic wavelike feature is due to the artificial viscosity. The shock stress at 1.3km/s is of the magnitude such that the plastic wave overtakes the elastic wave as per Figure 2 from Chapter 2. Such shock waves are generally termed *overdriven*.

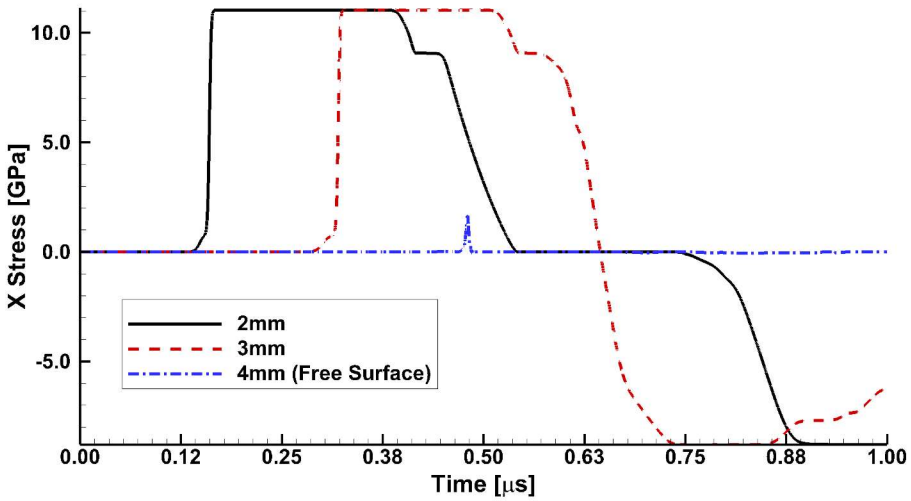


**Figure 19 – X Stress elemental time history data for nodes at 2mm, 3mm, and 4mm along the target**

The stress history from Figure 19 for the 1.3km/s impactor matches the profile seen in Figure 17 for the .5km/s impactor. However, the peak stress is approximately 6GPa higher. Additionally, the maximum tensile stress at the 3mm element is comparable to the maximum compressive stress.

### 4.3 1D Simulation of Symmetric Impact Without Backing but with Window

The next 1D simulation was performed for symmetric impact just as the previous simulation, but had the addition of a LiF window material. Table 3 shows the simulation configuration. The purpose of the window is to increase the travel of the shock wave to the free surface of the window to prevent the reflection of the shock wave from causing spall failure inside the sample. The use of the window in the different configurations of this thesis is to ensure that the behavior of the failure model is consistent in updating the correct nodal velocity and elemental stress levels which are compared to the nodal velocities and elemental stresses of the same geometry without a failure model. If there is reasonable

agreement, then the failure model is repeated without a window to induce failure inside the sample. Since there are two sets of impactor speed data, each geometry is run at both impactor speeds.

The geometry of the window was chosen such that window had sufficient length to transmit the loading and unloading pulse past the free surface of the Aluminum before the reflection from the free surface of the window would reach the free surface of the sample, which prevents spall in the sample. Considering that spall was not occurring in the sample, the results from the spall models in the sample are compared to the homogeneous model to ensure that there is not a discrepancy in the velocity and stress calculation.

**Table 3 – Geometric values for 1D homogeneous simulation with no material failure model with an impactor at .5km/s and an LiF window**

| Body | Material | Length [mm] | $V_i$ [km/s] | Merge Setting |
|---|---|---|---|---|
| $B^2$ | 6061-T6 | 1.000 | 0.500 | 1 |
| $B^3$ | 6061-T6 | 3.000 | 0.000 | 2 |
| $B^4$ | LiF | 2.500 | 0.000 | 2 |

Figure 20 and Figure 21 show the results from the .5km/s impactor with window configuration.

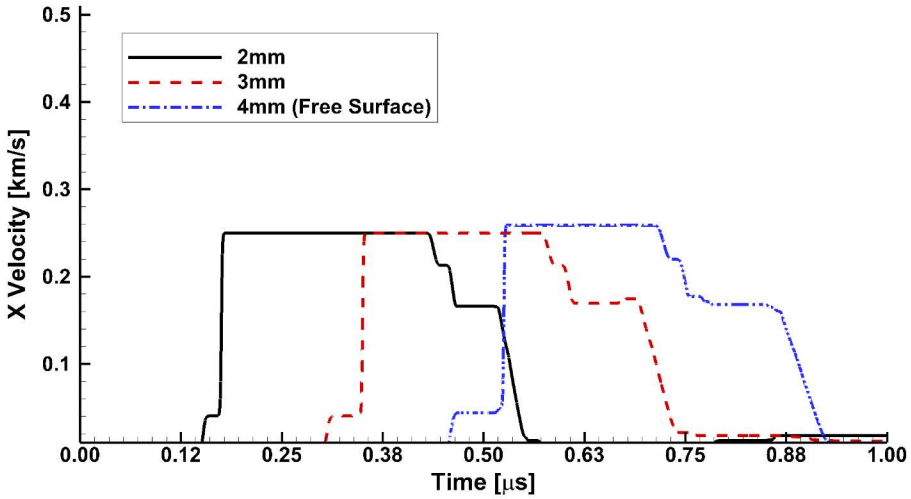


**Figure 20 – X Velocity nodal time history data for nodes at 2mm, 3mm, and 4mm along the target with 0mm being the beginning of the .5km/s impactor with an LiF window**

The free surface node from the previous simulation is now the interface between the Aluminum sample and the LiF window. Thus, the boundary condition is different and allows the wave to pass into the window instead of reflecting. This is evidenced by the 4mm velocity profile in Figure 20 compared to the profile in Figure 16. In addition, the wave can completely unload as compared to the 3mm profile from Figure 16 which maintains velocity due to reflection from the free surface.

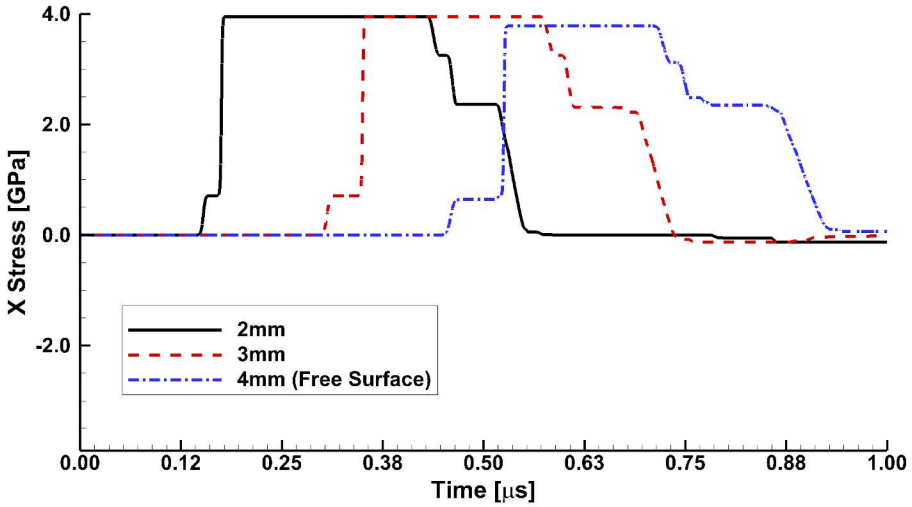


**Figure 21 – X Stress elemental time history data for nodes at 2mm, 3mm, and 4mm along the target**

The stress elemental history of Figure 21 can be compared to the profiles shown in Figure 17, but the profile of the 4mm node location shows that it can withstand compressive loading because the wave is travelling into the window.

Next, the same geometry as Table 3 was repeated such that $V_i$ of $B^1$ was 1.3km/s. The results from the 1.3km/s symmetric homogeneous impactor can be seen in Figure 22 which shows the time-history nodal velocity and Figure 23 which shows the time-history elemental stress data.

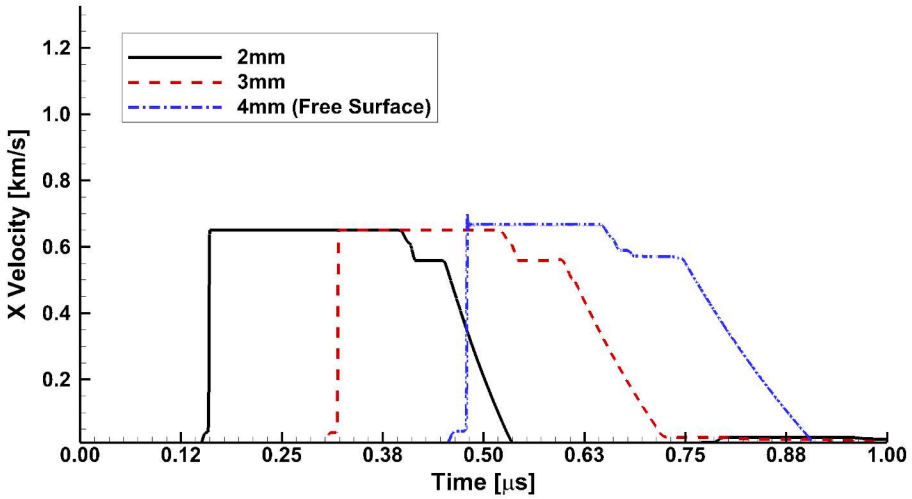


**Figure 22 – X Velocity nodal time history data for nodes at 2mm, 3mm, and 4mm along the target with 0mm being the beginning of the 1.3km/s impactor with an LiF window**

The results from the 1.3km/s impact velocity with a LiF window show the same nodal velocity trend as the .5km/s velocity with a LiF window.

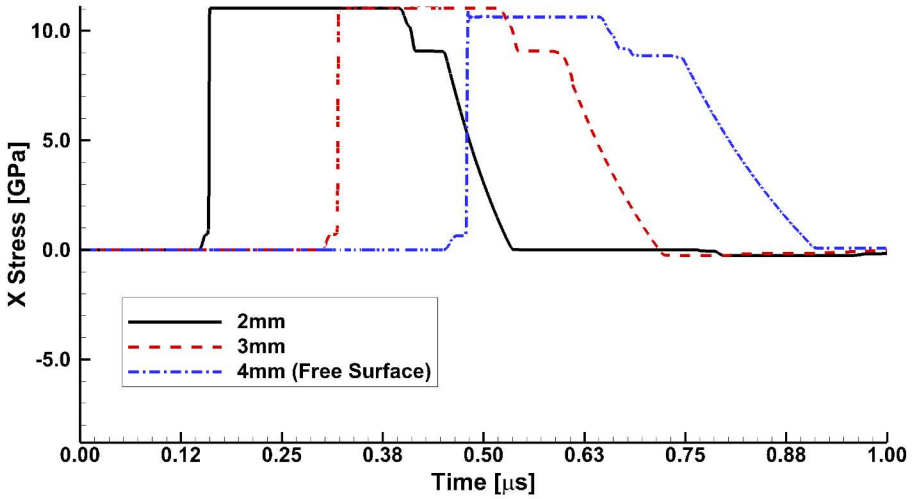


**Figure 23 – X Stress elemental time history data for nodes at 2mm, 3mm, and 4mm along the target**

The results from the simulations with the window show that the entire length of the sample can be examined without the reflective wave effects from the free surface of the sample. This means that the failure models can be run similarly to ensure that they are consistent with the homogeneous model without causing the material to fail due to the wave reflection from the free surface.

### 4.4 1D Spall Simulation with Cochran-Banner Damage Model

The Cochran-Banner damage model discussed previously was used to simulate spall in 6061-T6 Aluminum at 0.5 km/s and 1.3 km/s impact velocities. The model parameters were determined so that the simulated free surface velocity profile matched reasonably well with the experimental data for both velocities. The spall strength Σ from Equation 19 is referred to in SHOCK-1D as $Sp$, and is thus referred to this way for the remainder of the thesis. Results are presented for the final values of parameters $Sp = 1.15\text{GPa}$ and $D_0 = 15\mu\text{m}$ for the 0.5 km/s and $Sp = 1.45\text{GPa}$ and $D_0 = 10\mu\text{m}$ for the 1.3km/s impact velocity.

Prior to running spall simulations with the damage model, a symmetric impact at .5km/s with a window and geometry from Table 3 was performed with the damage model and compared to the homogeneous non-failure model. The results from this comparison are seen in Figure B.1-4 in Appendix B.

The 1D geometric properties for the .5km/s spall experiment can be seen in Table 4. The impactor was made of Z-Cut Quartz with material and EOS properties that can be found in Table A.2 in Appendix A.

**Table 4 – Geometric properties for .5km/s impactor case**

| Body | Material | Length [mm] | $V_i$ [km/s] | Merge Setting |
|---|---|---|---|---|
| $B^2$ | Z-Cut Quartz | 3.187 | 0.497 | 1 |
| $B^3$ | 6061-T6 | 5.883 | 0.000 | 2 |

The free surface nodal velocity data is shown in Figure 24 along with the experimental data for the .5km/s impactor.

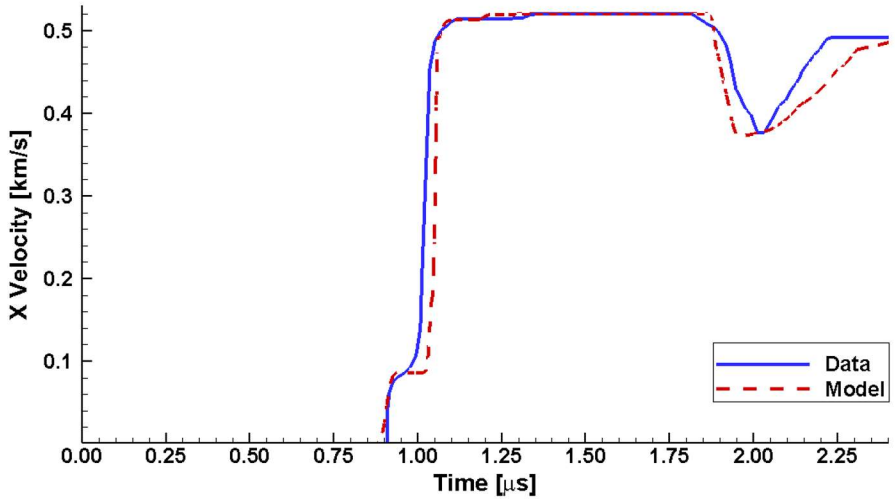


**Figure 24 – Free surface velocity from Cochran-Banner model (red) and experimental data from .5km/s impactor test (blue)**

As seen in Figure 24, the profile for the Cochran-Banner model shows reasonable agreement to the experimental data for the .5km/s impactor spall experiment. The most notable agreement is that the spall strength is nearly accurate, but the slope of the post pull-back velocity is slightly shallower from 2μs to 2.25μs.

The 1D geometric properties for the 1.3km/s experiment can be seen in

Table 5. The impactor was made of Aluminum 6061-T6 with a Lexan backing. The material and EOS properties of Lexan that can be seen in Table A.4 in Appendix A.

**Table 5 – Geometric properties for 1.3km/s impactor case**

| Body | Material | Length [mm] | $V_i$ [km/s] | Merge Setting |
|---|---|---|---|---|
| $B^1$ | Lexan | 4.000 | 1.318 | 1 |
| $B^2$ | 6061-T6 | 3.078 | 1.318 | 1 |
| $B^3$ | 6061-T6 | 5.910 | 0.000 | 2 |

The free surface velocity nodal velocity data is shown in Figure 25 along with the experimental data for the 1.3km/s impactor.

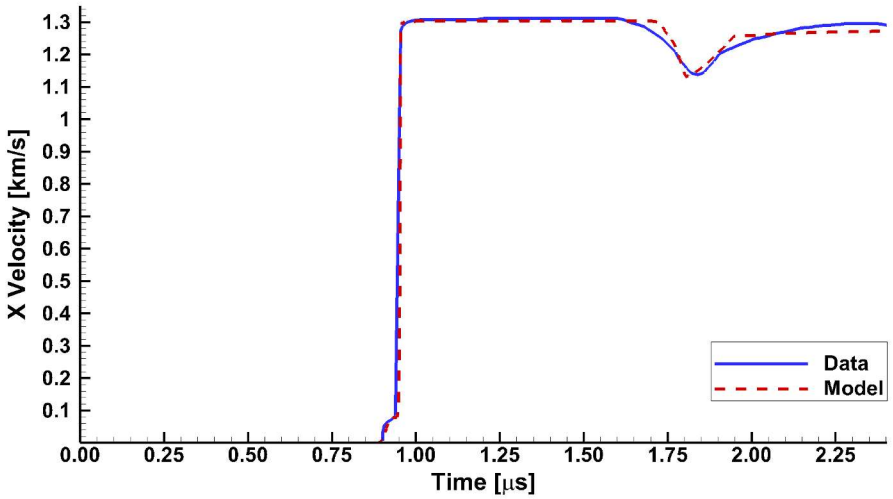


**Figure 25 – Free surface velocity from Cochran-Banner model (red) and experimental data from 1.3km/s impactor test (blue)**

As seen in Figure 25, the profile for the Cochran-Banner model shows reasonable agreement to the experimental data for the 1.3km/s impactor spall experiment.

## 4.5 1D Spall Simulations with Jim Johnson VNGC Failure Model

To ensure that VNGC model did not predict spall failure in the presence of the window body, symmetric impact with a LiF window of Table 3 was simulated activating the model for 6061-T6 Aluminum. In the absence of failure, the simulation results should

agree with the simulation results with homogeneous model presented in section 4.3. The agreements are shown in Figure B.1-4 in Appendix B.

The actual spall experiment with geometry given in Table 4 was simulated at 0.5 km/s impact velocity. Figure 26 compares the free surface velocity profile obtained from simulation with experimental data. Reasonable agreement was obtained for the Jim Johnson model parameters $a_s = 0.115\text{GPa}$, $\alpha_f = 1.05$, and $\eta = 1.50$.

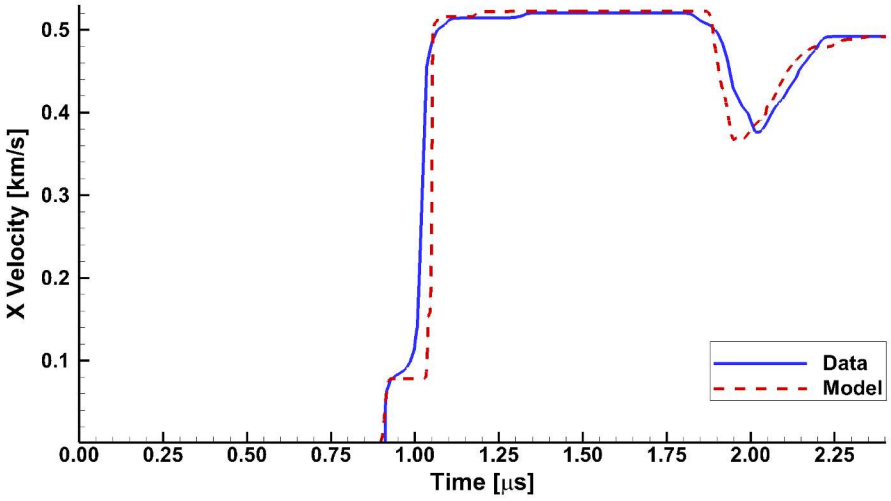


**Figure 26 – Free surface velocity from Jim Johnson model (red) and experimental data from .5km/s impactor test (blue)**

Like the Cochran-Banner results, the Jim Johnson VNGC model shows reasonable agreement. However, the Jim Johnson model shows closer profile matching from 2μs to 2.25μs. It needs to be pointed out that while $Sp$ in the Cochran-Banner model directly represents spall strength, the parameter $a_s$ in Jim Johnson model is not the spall strength. The spall strength still needs to be calculated from the pull-back velocity.

Figure 27 shows the comparison of the simulated velocity profile with experimental data for 1.3km/s impact velocity with geometry given in Table 5. For the 1.3km/s impactor

case, the failure parameters for the Jim Johnson simulation showed reasonable agreement with $a_s = 0.140\text{GPa}$, $\alpha_f = 1.05$, and $\eta = 0.65$.

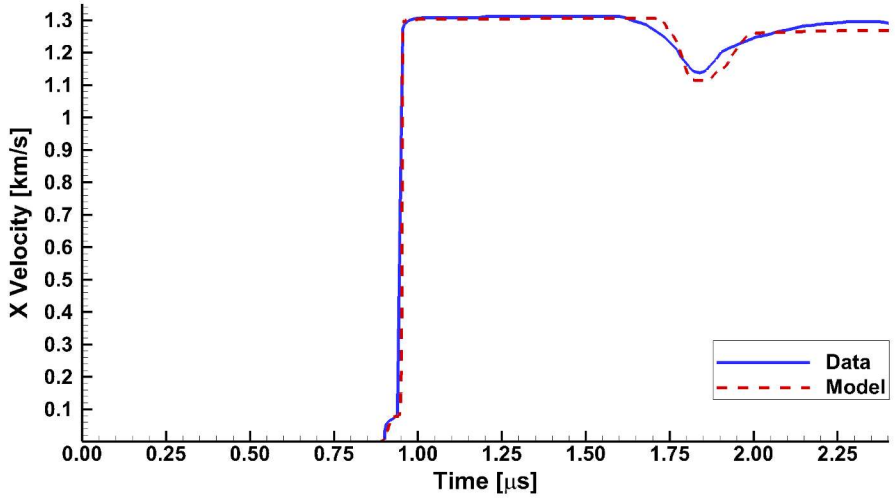


**Figure 27 – Free surface velocity from Jim Johnson model (red) and experimental data from 1.3km/s impactor test (blue)**

As seen in Figure 27, the profile for the Jim Johnson VNGC model shows reasonable agreement to the experimental data for the 1.3km/s impactor spall experiment. With the increase in impact velocity, the increase in $a_s$ value corresponds to the increase in the $Sp$ value of Cochran-Banner model. This also corresponds to a decrease in the viscosity $\eta$ value showing that the material hardens as the shock stress increases.

## 4.6 1D Spall Simulation with Cohesive Element Failure Model

To simulate spall failure by grain boundary cohesive failures, the sample body was divided into 99 bodies (assuming 99 grains with average grain size 60μm) with cohesive elements between two consecutive bodies representing the grain boundary cohesion. Each body was further discretized into 25 1D elements. While the sample body was technically subdivided, the total length of all bodies of the sample body correlated to the geometry

from Table 4. The three variables corresponding to the cohesive model are input to the SHOCK-1D code as the maximum traction $T^m$ ($M_{TR}$), the critical distance $\lambda_c$ ($C_{RD}$), and failure distance $\lambda_f$ ($F_{RD}$). Figure 28 compares the free surface velocity profile obtained from simulation with experimental data. The reasonable agreement was obtained for the cohesive element failure model parameters $M_{TR} = 1.109$GPa, $C_{RD} = 3.369$E-3, and $F_{RD} = 3.292$E-5.

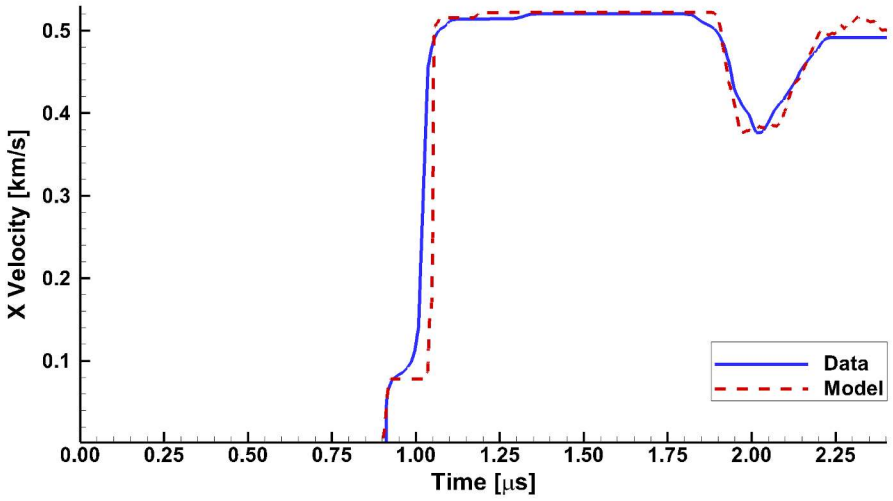


**Figure 28 – Free surface velocity from cohesive element failure model (red) and experimental data from .5km/s impactor test (blue)**

The cohesive element failure model is also able to match the spall strength of the experimental data with reasonable agreement. However, the pullback signal of the cohesive element failure model from 1.9μs to 2.1μs is almost flat in Figure 28.

The 1.3km/s impact case was similarly simulated by splitting the sample body from Table 5 into grain size bodies and implementing the cohesive elements between them. Figure 29 shows the 1.3km/s cohesive element failure model simulation with model parameters $M_{TR} = 1.235$GPa, $C_{RD} = 1.930$E-2, and $F_{RD} = 2.900$E-5.

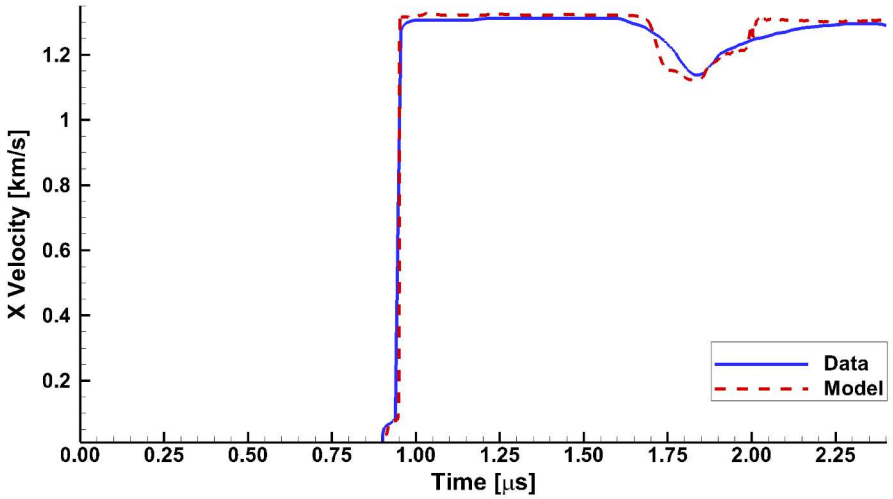


**Figure 29 – Free surface velocity from cohesive element failure model (red) and experimental data from 1.3km/s impactor test (blue)**

Like the .5km/s simulation, the cohesive element failure model matches the experimental data for the 1.3km/s test with acceptable agreement. It is important to note that the ratio of $M_{TR}$, $C_{RD}$, and $F_{RD}$ is different than the ratio used in the 1.3km/s simulation which corresponds to the effective elastic modulus of the cohesive elements.

## 4.7 1D Spall Simulation with Combined Failure Model

To simulate spall failure under the combined effect of VNGC and grain boundary cohesive failures, the cohesive element failure model was implemented at the grain boundary as before, but this simulation adds the VNGC model which acts within each element during tensile loading. The failure parameters with the best agreement for each of the damage models discussed above were used for the combined failure model and the results for the 0.5 km/s and 1.3 km/s are shown in Figure 30 and Figure 31.

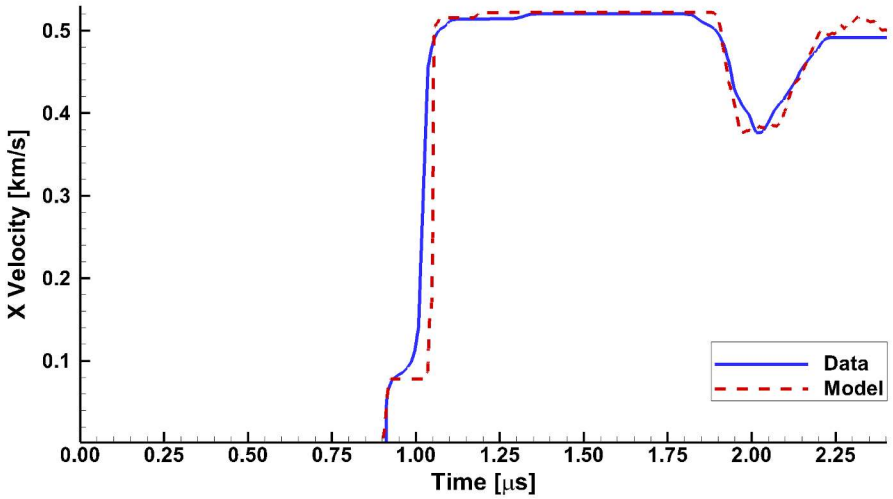


**Figure 30 – Free surface velocity from combined damage and VNGC failure model (red) and experimental data from .5km/s impactor test (blue)**

The results in Figure 30 for the velocity of the free surface show the exact same result from the cohesive element only failure model simulation. The reason for this is that the implemented failure parameters cause one failure mode to dominate the simulation. For this reason, a thorough study into the effect of changing the model parameters was conducted and is discussed below.

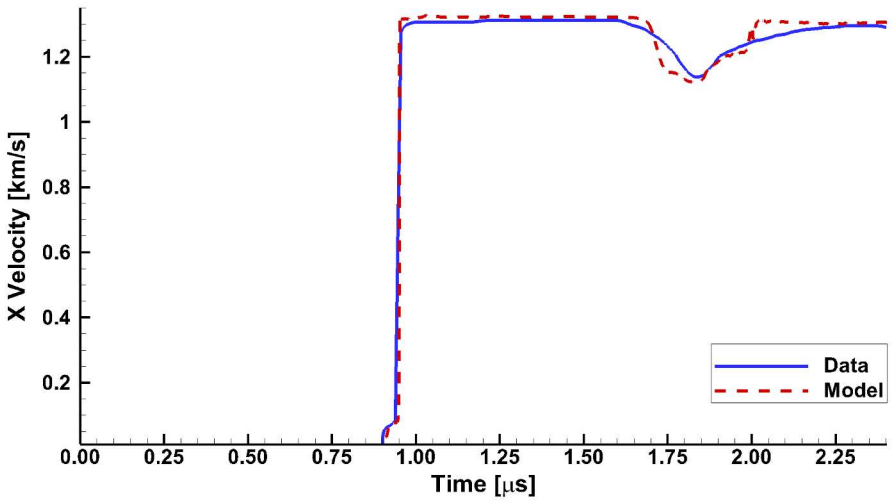


**Figure 31 – Free surface velocity from combined damage and VNGC failure model (red) and experimental data from 1.3km/s impactor test (blue)**

The free surface velocity result from the 1.3km/s combined failure simulation seen in Figure 31. This result is also the same as the result for the 1.3km/s cohesive element only simulation.

## 4.8 Discussion of 1D Impact Simulation Results

1D simulations play a key role in model development and the determination of their parameters for shock response of materials. As discussed above, this is due to the low cost of time and computational memory for 1D simulations. Also, the material deformation under uni-axial strain conditions with zero lateral strains for homogeneous materials in 1D is similar to the plane strain conditions in 2D. The results from the homogeneous material symmetric impact with window from Section 4.3 were important to understand the effect of the wave reflection from the free surface vis-à-vis when it is not reflected and to ensure that damage models do not predict failure when tensile stress is not generated in the sample.

The free surface velocity profile from the simulation agreed reasonably well with experimental data at the two impact velocities when each individual failure model was used and with best-fit model parameters. However, when the VNGC and cohesive models were activated together in the combined failure model, the results showed the need to re-tweak their parameters. This was performed in a limited way and is presented below to gain insights into the combined failure modes. However, detailed simulations to determine the best-fit parameters were not undertaken due to the limitations and subtle differences between the 1D cohesive model and the 2D cohesive model. In reality, grain boundaries are, in general, randomly oriented requiring at least 2D simulations.

# CHAPTER 5. 2D SHOCK SIMULATION RESULTS AND DISCUSSION

## 5.1 Methods for 2D Impact Simulation

The work done in 1D was advanced to 2D simulations, with the end objective of implementing the spall models in a shock propagation simulation code and simulate spall failure in 2D. This end objective could not be fully achieved due to lack of time; however, 2D simulations performed as a preparation to the end objective are presented and discussed. The code chosen was LS-DYNA and the Sandia National Laboratories mesh generation code CUBIT. LS-DYNA has a well-established history of shock simulation starting with HEMP in the early 1960s followed by DYNAs in the 1980s developed at Lawrence Livermore National Laboratory for the specific purpose of simulations of shock response of materials. LS-DYNA is the off-shoot from DYNAs, available as commercial software and popular in impact crashworthiness analyses. The code has an easy-to-use pre-processor GUI to create geometry, discretize into finite elements, assign materials properties, define contact with friction either by defining slide-lines or automatic contacts, and post-process of results in the form of state, nodal, and element outputs. However, defining geometries and discretization in CUBIT is better than LS-DYNA, and the latter code has the option to import a CUBIT-generated mesh file. For this reason, the two codes were used in tandem. The three different types of simulations carried out are as follows. The first simulation carried out was the symmetric impact of 1mm thick 6061-T6 Aluminum on a 3mm thick Aluminum target presented in Section 4.2 at 0.5 km/s impact velocity. In contrast to the 1D simulation with zero width, the width of both impactor and sample were 1mm so that

the waves from the two boundaries do not reach the centreline, which is where the VISAR measurement is taken. The geometry can be seen in Figure 32.

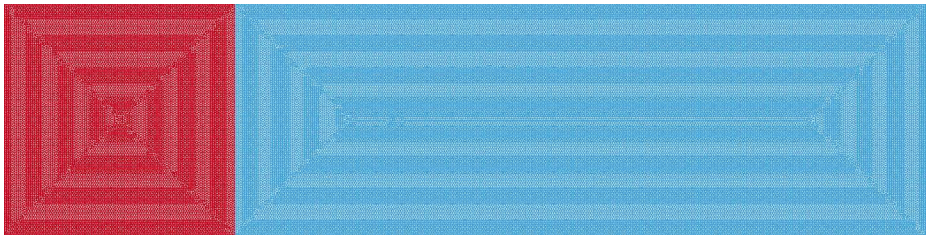

**Figure 32 – 2D Homogeneous Geometry**

The simulation also served the purpose of testing the automatic contact algorithm in LS-DYNA with friction. Instead of pre-defining a slide-line with master and slave surfaces between impactor and sample, the built in automatic contact algorithm was prescribed with a static friction coefficient of 0.3 to prevent the two bodies from overlapping. The contact algorithm in LS-DYNA imposes an impenetrability condition by applying penalty forces proportional to the detected magnitudes of overlap or penetration.

The lateral velocity in Y- direction for nodes on the two boundaries y=0mm and y=1mm were restrained while all other nodes inside the RVE were free to move in the X- as well as the Y- directions.

Two mesh sizes were studied. The two bodies were discretized in LS DYNA into 3-noded constant strain triangles with size 5μm first and then 10μm. The nodes of the meshes were checked to ensure that the nodes on the boundary of the impactor corresponded to the nodes on the boundary of the sample. The mesh, can be seen in Figure 33, which is a zoomed in area of Figure 32.

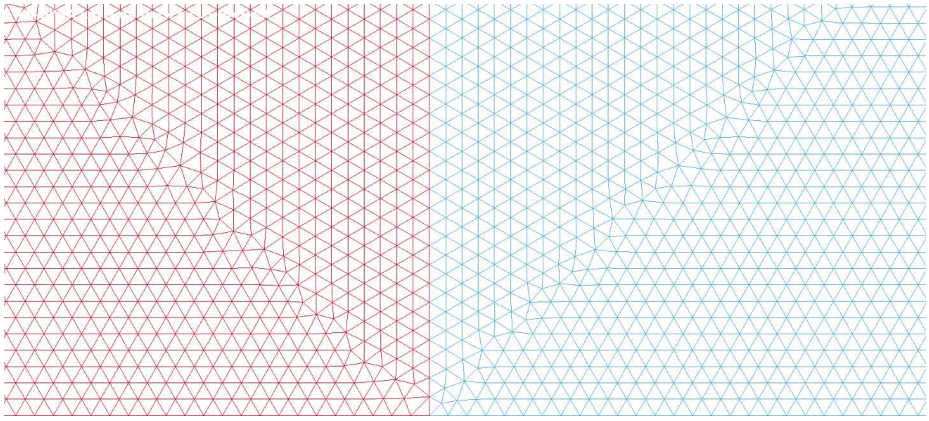

**Figure 33 – Mesh of 2D homogeneous shock simulation**

The second 2D simulation performed was the shock response of dry sand at an impact velocity of 0.75km/s. The objectives were to create a granular geometry that did not require cohesive elements or a user-defined material model (UMAT) and to test full functionality of automatic contact in LS-DYNA. As shown in Figure 34, the geometry chosen for this purpose was an 8mm thick impactor impacting on a 3mm thick sand sample encapsulated between two 1mm thick buffer and backed by an 8mm thick window. All the materials were Z-cut Quartz with the difference that the impactor, buffers, and window were made elastic while sand grains were made to be elastic-plastic. The thickness of the RVE was 1mm, mean grain size of the sand was 60μm with ±20% variation, and porosity was 20% and 30%.

The sand sample was generated by randomly seeding a larger RVE with 50% larger grain size, generating grains using Voronoi tessellation, shrinking the grains to their original size, and allowing the grains to fall freely by eliminating overlap and minimizing energy. The process checks the porosity in layers and freezes the grains in the layer from further movement once the desired porosity is reached. Thus, sand grains were randomly

oriented with mostly point contact between them and free spaces representing porosity. Finally, the 3mm x 1mm RVE was cut from the generation. The generated grains together with the impactor, buffers, and window blocks were imported to CUBIT and discretized into 3-noded triangular elements using the mesh size of 5μm. The mesh can be seen in Figure 34. The generated and discretized bodies were imported directly to LS-DYNA and assigned materials properties, boundary conditions, initial conditions, etc. using the GUI of the code.

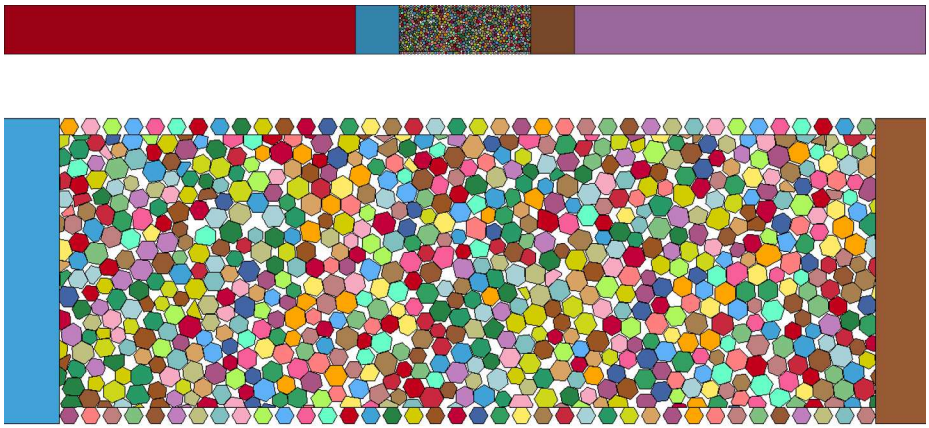

**Figure 34 – The five separate sections (Top). A close look at the Z-Cut Quartz sand grains configuration (Bottom)**

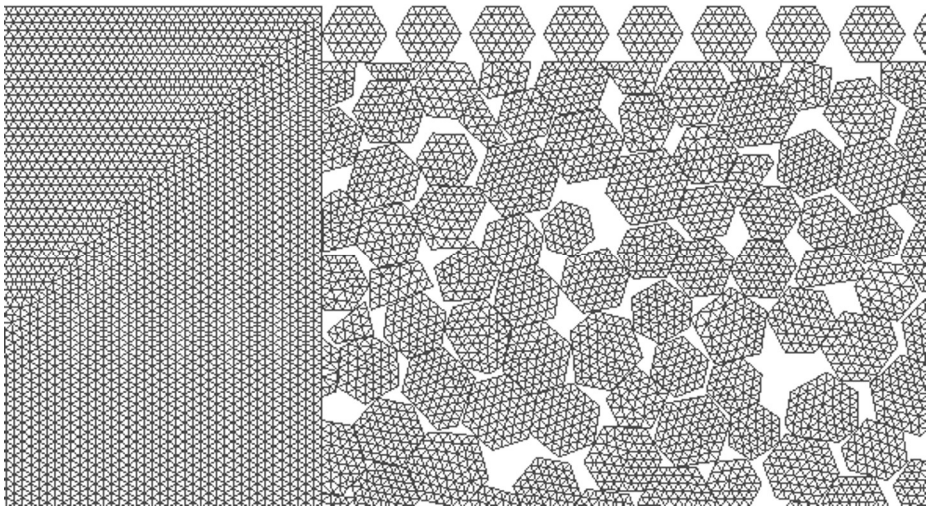

**Figure 35 – Sand mesh as well as the mesh for the first stationary Z-Cut Quartz block**

The third simulation carried out was for the 2D heterogeneous simulation using LS-DYNA for spall in Aluminum with a 0.5km/s impact velocity with a 3.187mm thick impactor and 5.883mm thick sample, as presented in section 4.4. The width of the two blocks was set to 0.5mm to decrease computational time compared to the 1mm width of the homogeneous experiment. The purpose of the simulation was to test the LS-DYNA features of a cohesive element coupled with automatic contact.

Instead of using the free-falling algorithm used for setting up the sand geometry, Aluminum grains were generated by seeding the actual size RVE for 60μm mean grain size having ±20% variation, and generating grains by Voronoi tessellation. Thus, the Aluminum grains had coincident edges as desired for the alloy system. The geometry can be seen in Figure 36.

**Figure 36 – Geometry of .5km/s impactor with heterogeneous 6061-T6 Aluminum sample**

The grains were meshed in CUBIT using a 10μm mesh size to reduce computational time. Two simulations were run. The first has all the grain edges merged and the second has the grain edges unmerged with 2D automatic surface to surface contact enabled. The meshed grains can be seen in Figure 37. Finally, cohesive elements were embedded between unmerged grains. In LS-DYNA, cohesive elements are specified using MAT-138 [16].

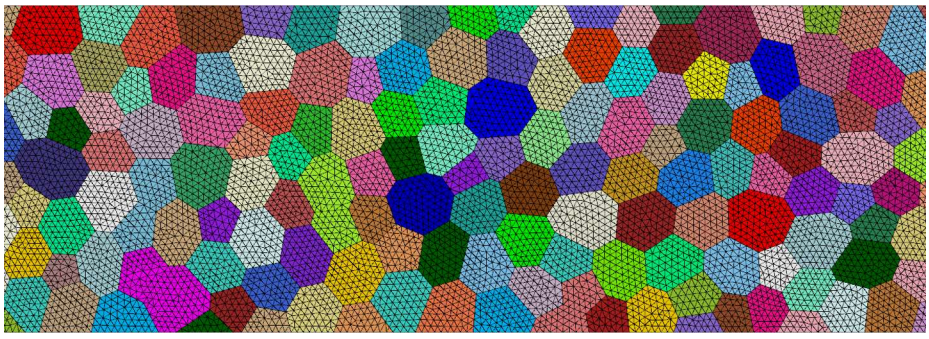

**Figure 37 – Close view of 2D meshed 60μm grains with 10μm mesh size**

The geometry for the 2D simulation of granular 6061-T6 Aluminum, with cohesive elements, is the same as the geometry for the merged and un-merged simulations seen in Figure 36. However, the meshing is slightly different.

The mesh size for the cohesive element simulation, 10μm, is the same as the merged and un-merged granular simulation. The difference is that there are additional elements along each of the grain boundaries. The cohesive elements are zero-volume elements, but

they can be visualized in Figure 38, where they are shown as four-sided elements along grain boundaries by shrinking the grains for visualization purpose.

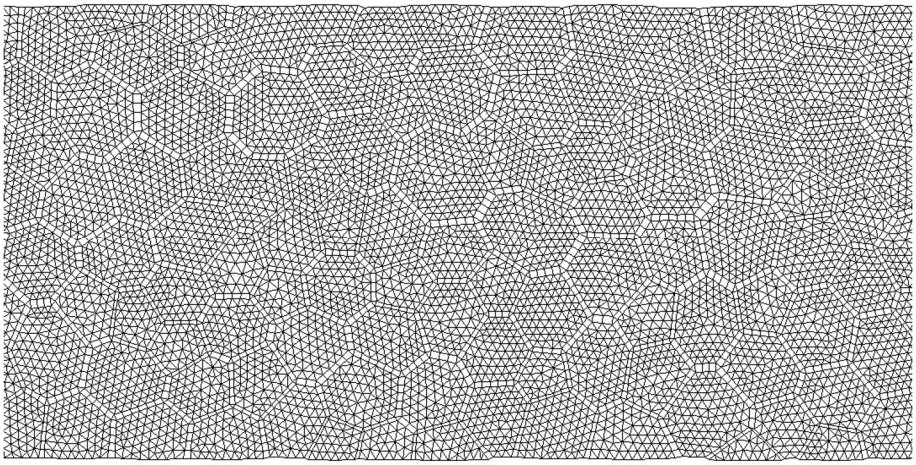

**Figure 38 – Shrunken grain mesh with expanded interface 2D cohesive elements for visualization purposes**

## 5.2 2D Symmetric Impact Simulation Results and Discussion

The contours of longitudinal velocity and stress in the X- direction from simulations at 0.5km/s impact velocity can be seen in Figure B.5-9 in Appendix B. Figure 39 shows the longitudinal velocity profile at 2mm, 3mm, and 4mm (free surface) at the center of a sample obtained from 2D LS-DYNA simulation. The velocity profiles from 1D simulation are superimposed for comparison. Figure 40 compares the longitudinal X-stress at the same positions with the 1D simulation results.

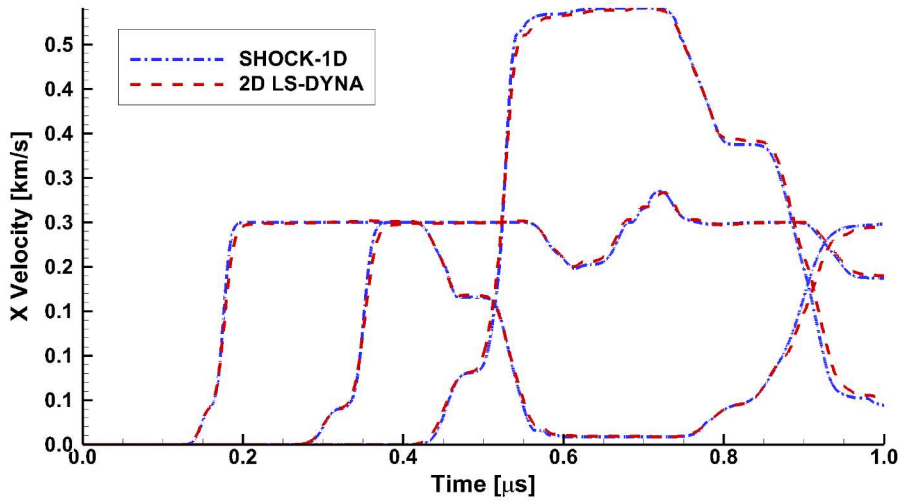


**Figure 39 – Comparison of homogeneous SHOCK-1D X Velocity results (blue) to homogeneous 2D LS-DYNA X Velocity (red)**

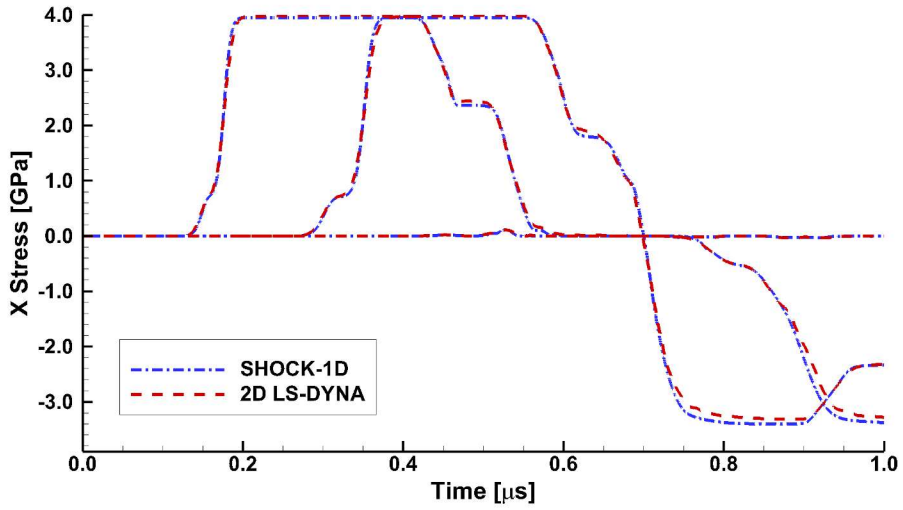


**Figure 40 – Comparison of homogeneous SHOCK-1D X Stress results (blue) to homogeneous 2D LS-DYNA X Velocity (red)**

Figure 39 and Figure 40 show very good agreement between 1D and 2D simulations results for the homogeneous case using the same materials properties. For this reason, the results for the stress and velocity calculation inside each grain in LS-DYNA can also be

assumed to also correspond to their respective calculations in SHOCK-1D as the grain interiors are effectively homogeneous bodies for the Aluminum simulation.

## 5.3 2D Heterogeneous Sand Simulation Results and Discussion

The sand simulations were carried out at 0.75km/s for 20% and 30% porosities in sand sample. In previous simulations for the homogeneous case, velocities and stresses were plotted at specific nodes and elements. This procedure cannot be used for the heterogeneous case due to the local wave reflection phenomena within grains. For this purpose, in-situ velocity and stress were obtained by averaging each of the two quantities along 300μm vertical lines. The vertical lines are initially centered at nodes at specified distances that move with the node. The procedure is carried out in TECPLOT using the macros written for the purpose. Because the average is used, the presence of local extreme values will not be seen in the plotted nodal history.

Figure 41 shows the in-situ longitudinal velocity and Figure 42 shows the longitudinal stress in the X- direction at three locations in the sand sample with 20% porosity. These locations correspond to 1.0mm, 1.5mm, and 2.0mm from the buffer-sand interface.

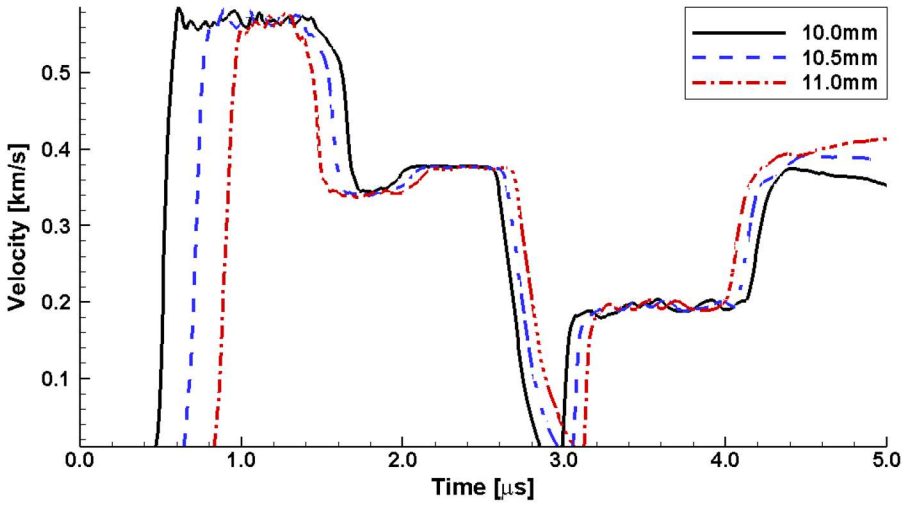


**Figure 41 – X-velocity nodal history data for 20% porosity Z-Cut Quartz sand simulation with impactor speed of .75km/s at 3 different locations in sand partition**

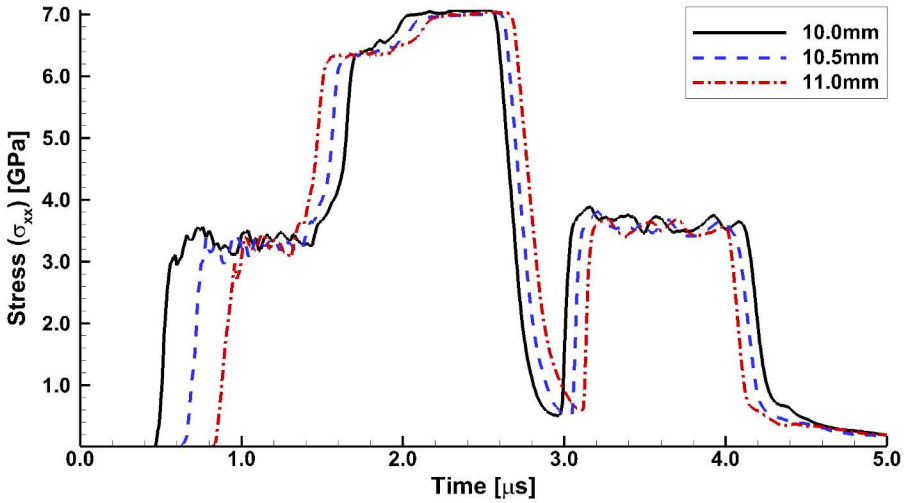


**Figure 42 – Stress in the X- direction for 20% porosity Z-Cut Quartz sand simulation with impactor speed of .75km/s at 3 different locations in sand partition**

As seen in Figure 41 and Figure 42, the sand is first loaded by the shock wave post impact after it travels through the buffer and enters the sand sample. The sand sample attains the peak state under shock loading at the three chosen locations. The shock wave on reaching the right buffer interface is reflected as a compressive wave due to the higher

impedance of the buffer. The reloading in compression at the three locations occurs by this reflected compressive wave. Finally, the material is unloaded by the unloading wave from the impactor's free surface.

Figure 43 shows the velocity and Figure 44 shows the stress profiles at same locations of the sand sample with 30% porosity.

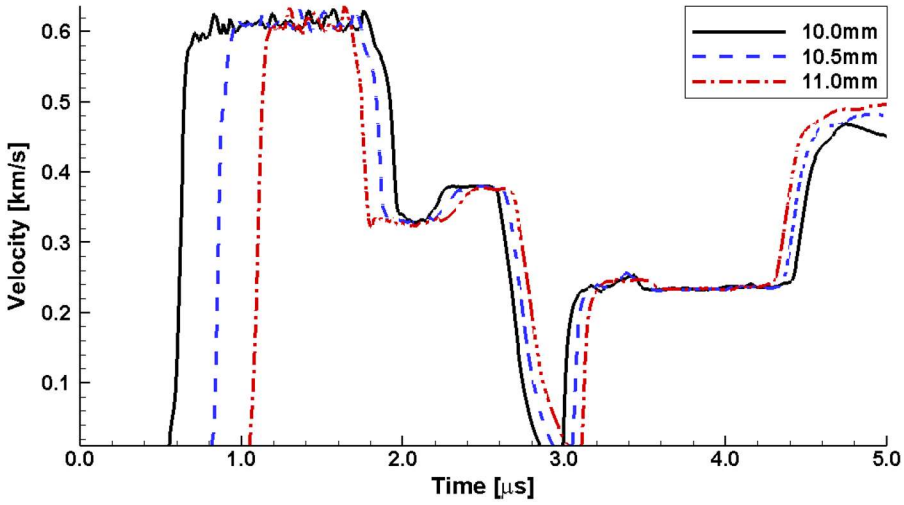


**Figure 43 – X-velocity nodal history data for 30% porosity Z-Cut Quartz sand simulation with impactor speed of .75km/s at 3 different locations in sand partition**

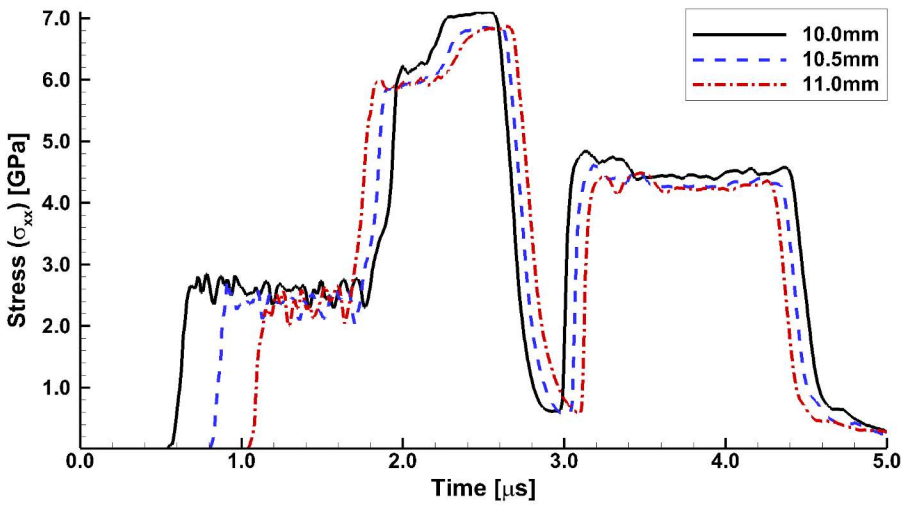


**Figure 44 – Stress in the X- direction for 30% porosity Z-Cut Quartz sand simulation with impactor speed of .75km/s at 3 different locations in sand partition**

As seen in Figure 43 and Figure 44, the sand experiences a similar loading pattern to the 20% porosity sand. However, the time between loading and reloading is greatly increased.

Figure 45 compares the longitudinal velocity and Figure 46 compares the longitudinal stress for 20% and 30% porosities at 10.0mm location.

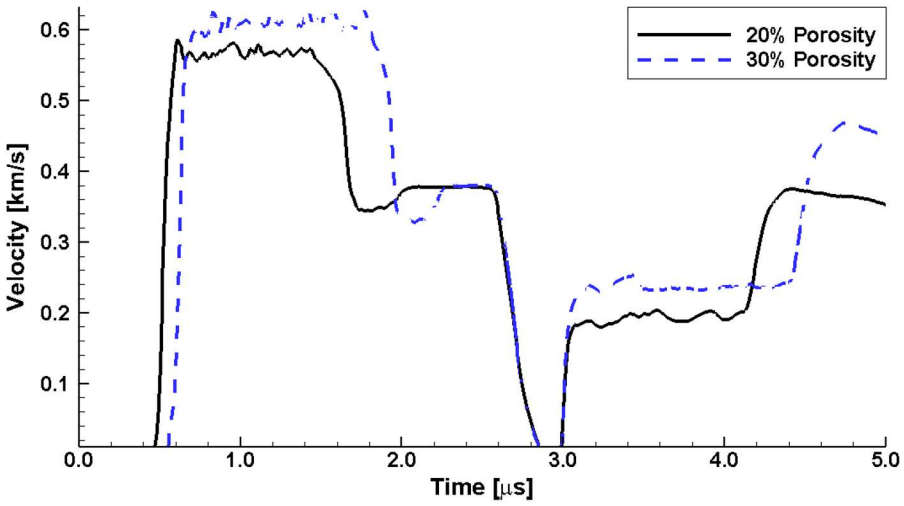


**Figure 45 – X-velocity nodal history data for both 20% and 30% porosity Z-Cut Quartz sand simulation with impactor speed of .75km/s at 10mm sand partition**

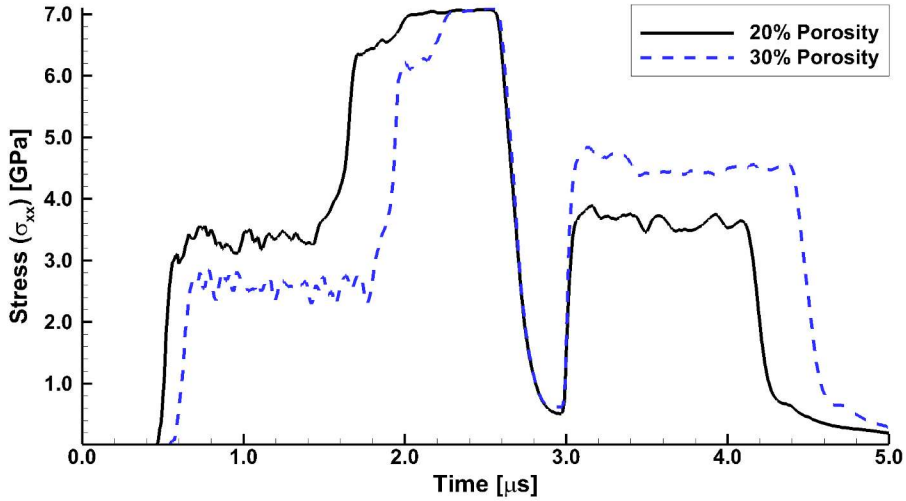


**Figure 46 – Stress in the X- direction for both 20% and 30% porosity Z-Cut Quartz sand simulation with impactor speed of .75km/s at 10mm sand partition**

For the same location in the sand partition, the higher the porosity, the longer it is taking for the compaction of the sand. In addition to the increased delay for the higher porosity the initial peak loading stress is lower and velocity is higher. However, the peak

reloading stress is the same. This indicates the differences in porosity in the compressed state does not affect the recompression appreciably.

### 5.4 2D Heterogeneous 6061-T6 Aluminum Simulation Results and Discussion

As discussed above, 2D simulations were carried out with a grain ensemble in the Aluminum sample. In the first simulation, grains had edge contacts with no cohesion at the grain boundaries: the load transfer between grains was primarily by the contact impenetrability condition with friction. In the second simulation, cohesive elements were embedded at the grain boundaries. As per the theory manual of LS-DYNA [16], the compressive response of cohesive elements is modelled through penalty formulation as is the case for imposing an impenetrability condition for the surface contact. However, whereas the penalty parameters in the contact algorithm are user defined and can be varied, the parameters in the cohesive formulation are built-in and cannot be varied by the user yet. This affects the agreement of the results from the two simulations. The contour results for the un-merged, contact-only, grain simulation can be seen in the Appendix B, Figure B.9, which shows the X- velocity, and Figure B.10, which shows the pressure.

The nodal time history for the X-velocity at the free surface can be seen in Figure 47. The grains separate as soon as the sample goes under tension due to the interaction of the two unloading waves. Thus, the unloading wave from the impactor does not reach the free surface to unload the velocity and subsequent increase. Thus, the contact-only simulation does not predict the unloading and pull-back velocity. The free surface velocity remains constant at the peak value except for a few oscillations.

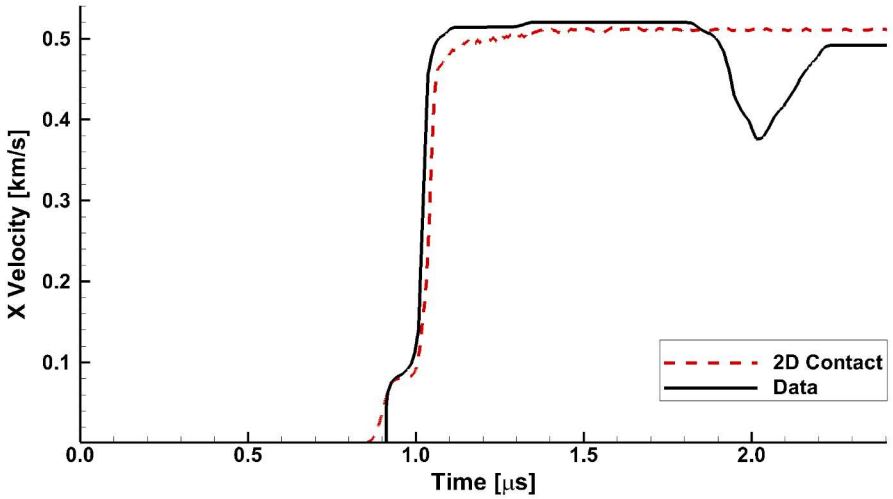


**Figure 47 – 2D contact grain simulation at free surface (Red) and experimental free surface velocity (Black)**

The contour results from a simulation with cohesive elements can be seen in Appendix B, Figure B.11, which shows the X velocity, and Figure B.12, which shows the pressure. The free surface results can be seen in Figure 48. Figure 49 shows the 2D cohesive element free surface velocity with the contact-only results as well as the experimental data for the 0.5km/s test.

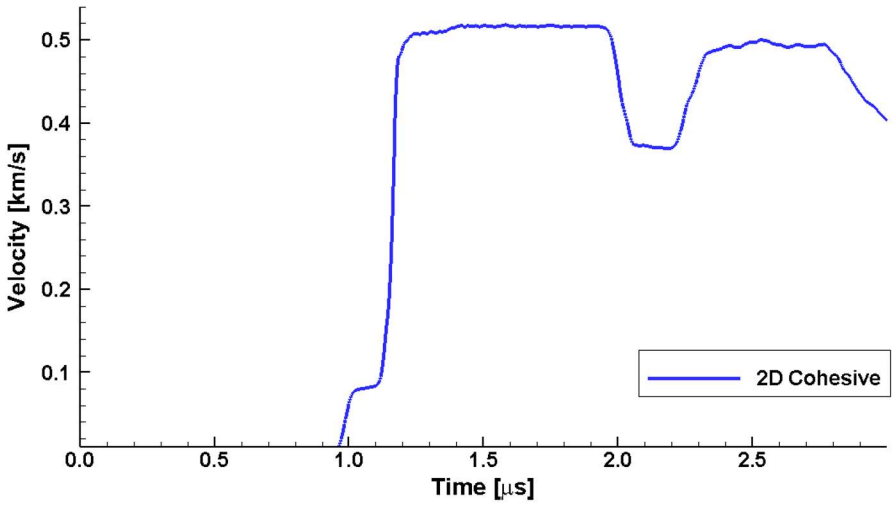


**Figure 48 – Nodal history result from 2D cohesive grain simulation at free surface**

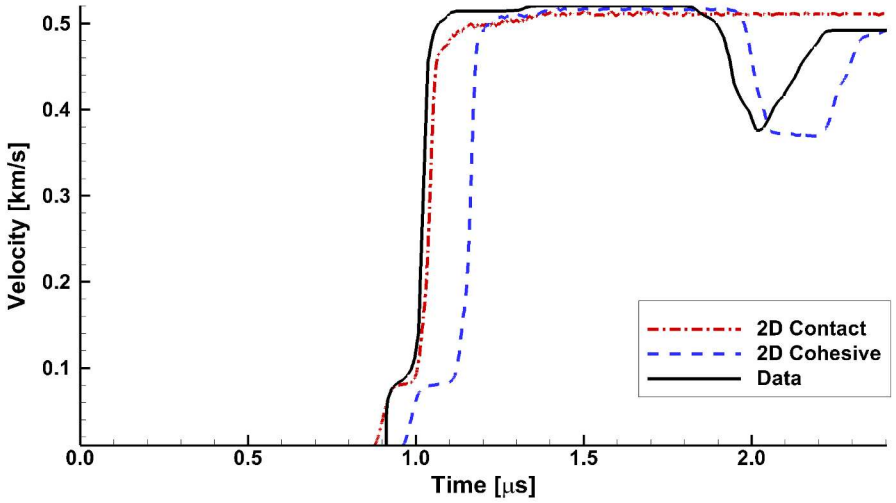


**Figure 49 – Nodal history result from 2D contact grain simulation at free surface (Red), 2D cohesive grain simulation at free surface (Blue), and experimental free surface velocity (Black)**

As seen in Figure 49, LS-DYNA predicts lower wave velocity for the cohesive simulations. This may be due to the penalty method used in its contact algorithm. The method calculates the penalty parameter using the current stiffness of the material. The parameter can be increased or reduced by specifying a multiplier in the input file. The force

applied to remove penetration (overlap) is calculated by multiplying overlap distance with the penalty parameter. The overlap may or may not be removed completely depending on the penalty parameter value and the overlap distance. Too large a value of the penalty parameter leads to instability. However, DYNAs has an additional parameter which is not available in LS-DYNA. Users in DYNAs can specify the percentage of overlap to be corrected at each cycle. Thus, overlap can be effectively corrected without instabilities in DYNAs by adjusting the percentage and the value of the penalty parameter. That is not the case in LS-DYNA. Thus, simulations advance with partial overlap between grains leading to lower wave velocity. However, the simulations could be optimized by undertaking detailed trial simulations and finding the optimal multiplier value for the penalty parameter. This exercise was not conducted in this work.

Figure 50 compares the free surface velocity from the 2D cohesive simulation with 1D cohesive simulation and experimental data.

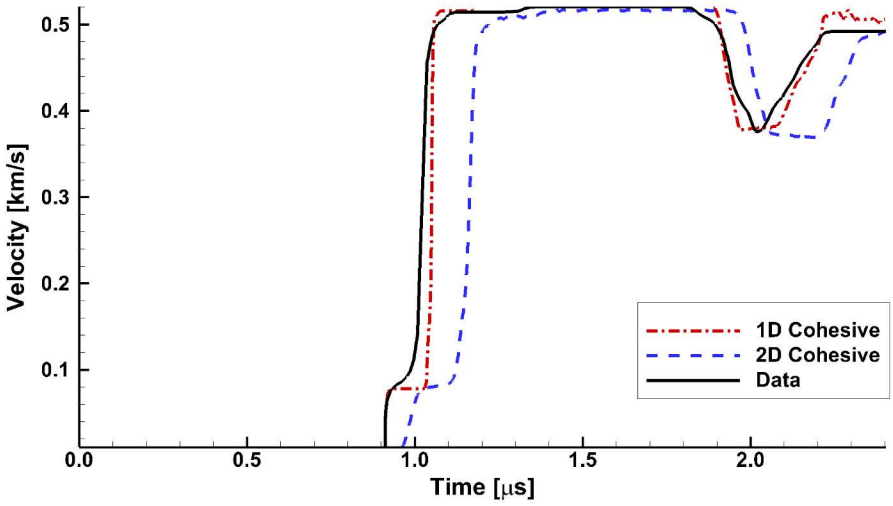


**Figure 50 – Nodal history result from 1D cohesive grain simulation at free surface (Red), 2D cohesive grain simulation at free surface (Blue), and experimental free surface velocity (Black)**

The result shows that apart from the lower wave velocity or time delay, the velocity profile from the 2D cohesive simulation is qualitatively similar to the result from the 1D cohesive simulation. The next step is to iterate with different values for the cohesive parameters in LS-DYNA to optimize the pull-back velocity profile. This was not undertaken in the present work primarily because the penalty parameter during compression of the cohesive elements cannot be varied. The future version of the code may have this option.

## 5.5 Discussion of 2D Impact Simulation Results

The mechanisms behind the homogeneous LS-DYNA simulations show very accurate agreement with the mechanisms behind the homogeneous SHOCK-1D simulations. With this, it can be assumed that in each area where the shock is propagating in a homogeneous manner, the agreement will also hold true such as inside the actual aluminum grains themselves. This allows for the parameters used in the 1D simulation to be optimized in 1D with reasonable expectation that they will hold relatively accurate in 2D simulations. This insight has the potential to save computing time.

Additionally, the reason for the delay in the shock loading when cohesive elements are introduced needs to be further investigated. However, the fact that the spall strength and general pull-back profile was nearly identical to the 1D is promising for future studies using these failure models in both 1D and in 2D simulations.

# CHAPTER 6. PARAMETER EFFECT ON 1D SHOCK PROPAGATION

The previous chapters presented and discussed the results from the 1D and 2D simulations using a set of individual model parameters obtained after in-depth iterative simulations carried out by varying individual parameters and studying the effect on shock propagation and velocity/stress profiles. The key effects of individual parameters and an attempt to calibrate the parameters for the combined failure model are presented below.

## 6.1 Effect of Artificial Viscosity on 1D Shock Profile

Following the work of Von-Neumann and Richtmyer for fluids and gases [27], artificial viscosity is a key mean stress component to obtain in-situ shock response without oscillations caused by the discontinuous shock front in a discretized medium. The basic premise of the artificial viscosity is that it changes the discontinuous wave front into a rapidly varying but continuous wave front. The thickness of the wave front so achieved varies from 3-to-5 times the grid/mesh size. Artificial viscosity calculates positive mean stress in compression and is otherwise zero during unloading and tension. There are two kinds of artificial viscosity: linear and quadratic. The linear viscosity damps the near-term oscillations, and quadratic viscosity damps the long-term oscillations. The details can be found in the work by Wilkins [28, 29] who pioneered the use of artificial viscosity for solids. The maximum values of coefficients are 0.5 and 4.0 for the linear and quadratic artificial viscosity, respectively. The first exercise in shock propagation simulation is to

arrive at the minimum value of the two coefficients that give the smooth wave profiles during propagation.

The effect of artificial viscosity is seen in the simulations if the term is not optimized for the given velocity of the impactor. If the artificial viscosity is too low, there will be oscillations in the time history data for the node. If the artificial viscosity is too high, the time history data will be over-damped and will not match the experimental phenomena. To show this effect, the coefficient of linear artificial viscosity was varied keeping the coefficient of quadratic viscosity at .2 while all other material parameters remained constant using the homogeneous model at 0.4km/s impact velocity. The longitudinal velocity in the X- direction at an interior node is shown in Figure 51.

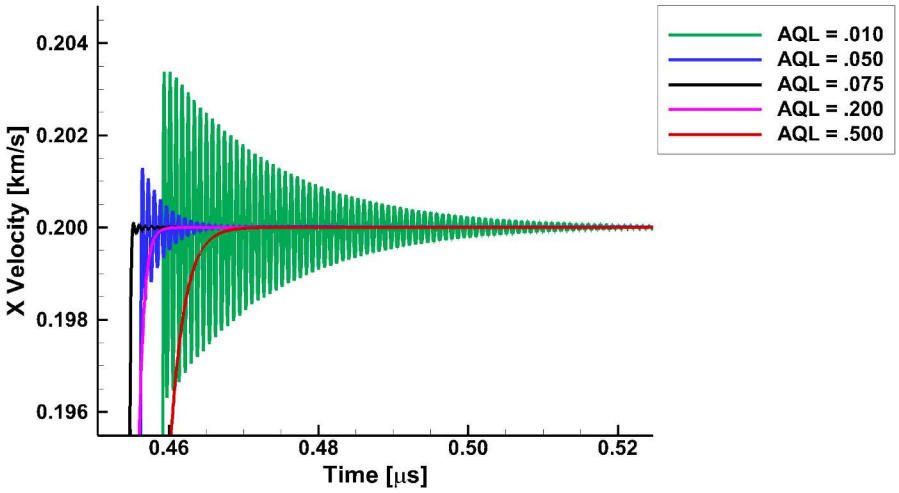


**Figure 51 – Interior nodal velocity of 6061-T6 Aluminum sample with differing linear artificial viscosity values with .4km/s impactor**

As seen in Figure 51, as the artificial viscosity term is increased, there are fewer oscillations in the X velocity profile. However, if the artificial viscosity term is too high,

there is over damping and the slope of the rising part of velocity starts increasing slowly as opposed to a sharp increase.

A similar effect is seen in Figure 52 for an impact velocity of 2.4km/s.

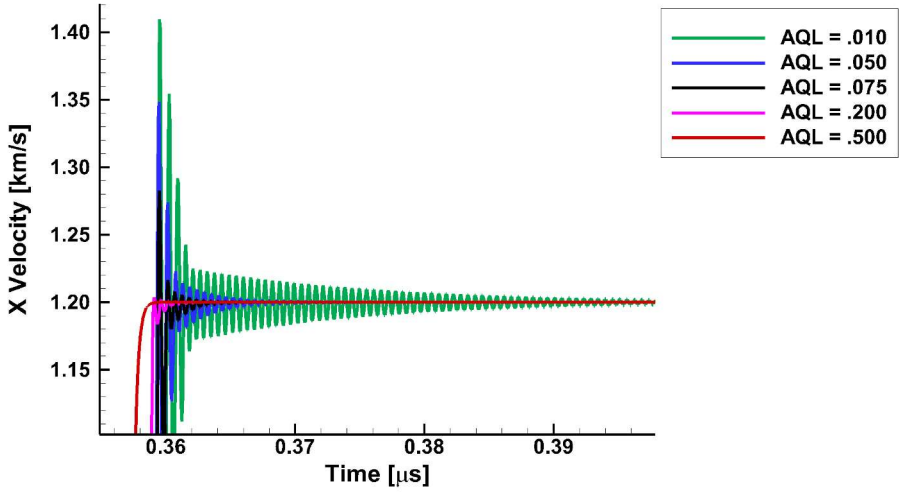


**Figure 52 – Interior nodal velocity of 6061-T6 Aluminum sample with differing linear artificial viscosity values with 2.4km/s impactor**

As seen in Figure 52, the same values of the linear artificial viscosity were used. However, the effect of the artificial viscosity, at the same value of $AQL$ as was used in the lower impact speed simulation, shows more oscillation at the higher impact speed.

## 6.2 Effect of Cochran-Banner Damage Model Parameters

Simulations were carried out by varying the spall strength $Sp$ keeping the void opening at failure, $D_0$, constant at 15μm and by varying $D_0$ keeping the spall strength $Sp$ constant at 1.15GPa. Figure 53 shows the effect of varying the spall strength at constant $D_0$ and Figure 54 shows the effect of varying $D_0$ at constant spall strength.

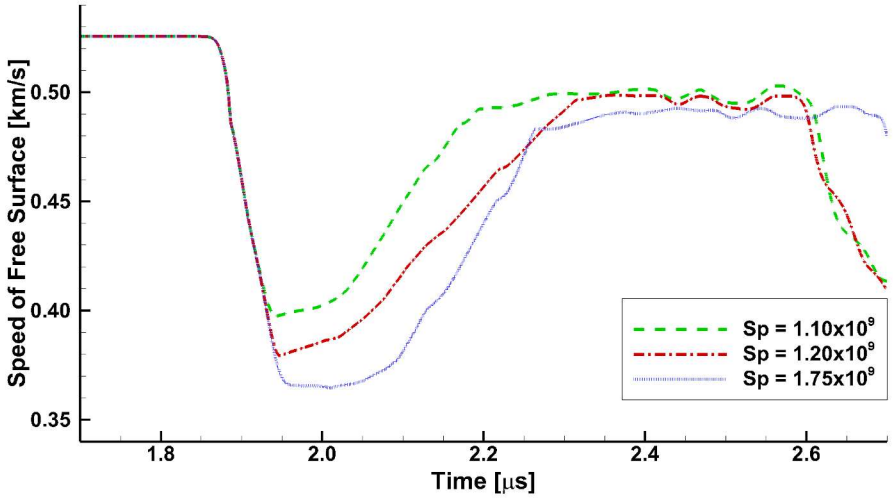


**Figure 53 – Effect of changing $Sp$ on Cochran-Banner Damage Model**

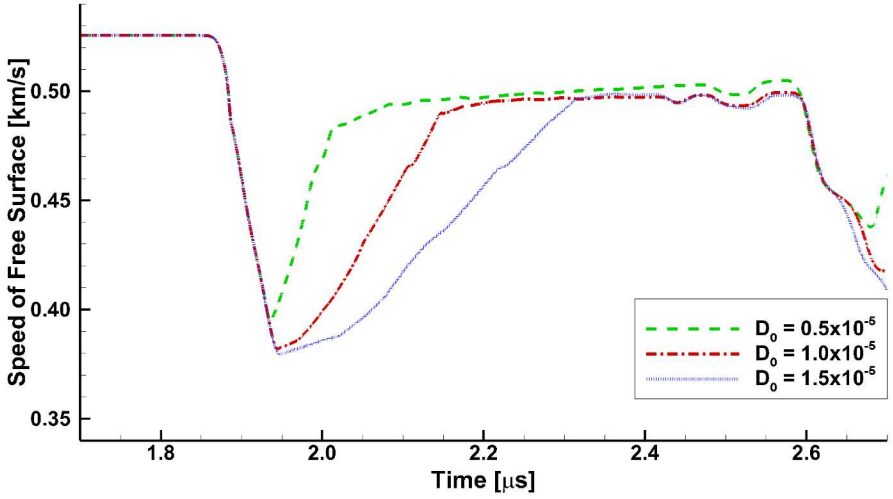


**Figure 54 – Effect of changing $D_0$ on Cochran-Banner Damage Model**

As seen in Figure 53, increasing spall strength increases the pull-back velocity, which corresponds to Equation 18. But, there are no appreciable changes in the slope of velocity post pull-back. The rounding of the velocity at higher spall strength indicates a lower rate of increase in void size. Increasing the void size at constant spall strength shown

in Figure 54 also increases the pull-back velocity, though marginally. However, there is appreciable increase in the slope of velocity post pull-back. Thus, the rate of void growth or spall failure causes the failure to become more brittle when reducing $D_0$.

## 6.3 Effect of Jim Johnson VNGC Model Parameters

Figure 55, Figure 56, and Figure 57 show the effect of varying $a_s$, $\alpha_f$, and $\eta$, respectively, while keeping the other two parameters of the Jim Johnson VNGC model constant.

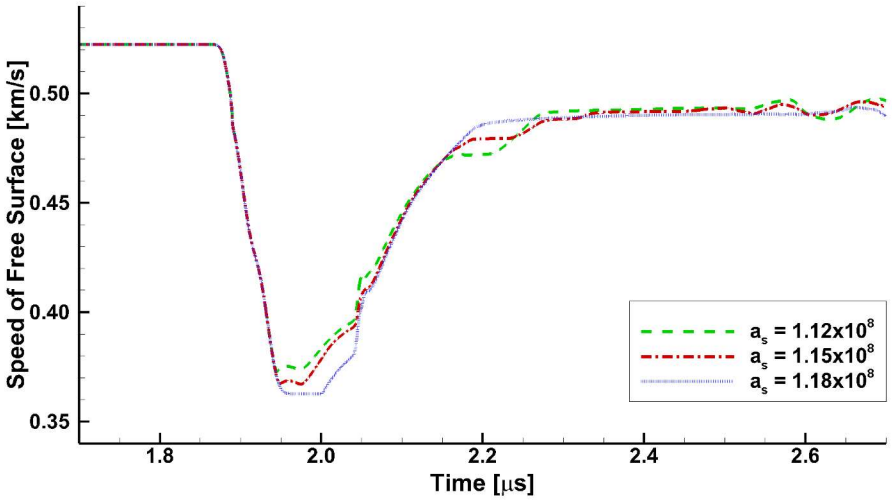


**Figure 55 – Effect of changing $A_s$ on Jim Johnson VNGC model**

As seen in Figure 55, while keeping $\alpha_f$ constant at $\alpha_f = 1.05$ and $\eta$ constant at $\eta = 1.5$, increasing $a_s$ increases the pull-back velocity and hence the spall strength. This is similar to how $Sp$ affects the spall strength in the Cochran-Banner damage model. There are no appreciable effects observed in velocity profile post pull-back.

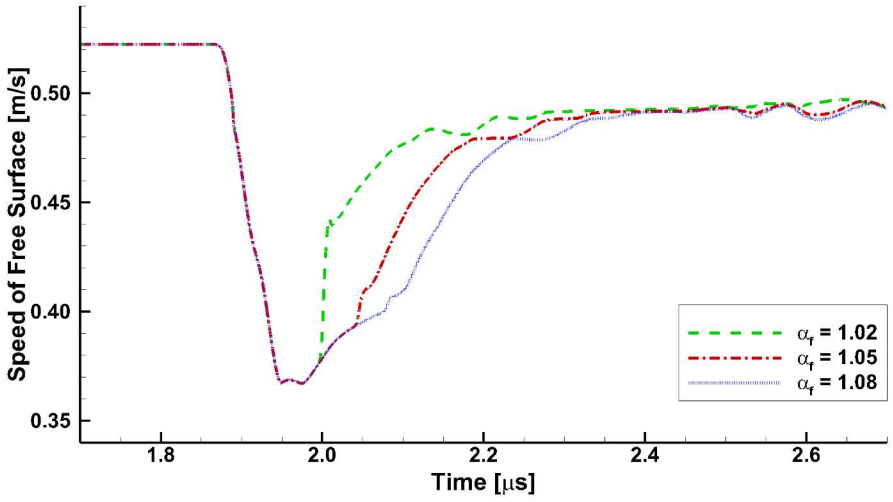


**Figure 56 – Effect of changing $\alpha_f$ on Jim Johnson VNGC model**

As seen in Figure 56, while keeping $a_s$ constant at $a_s = 1.15\text{E}{+}8$ and $\eta$ constant at $\eta = 1.5$, increasing failure distension $\alpha_f$ in the 1.02-to-1.08 range does not affect the spall strength as $D_0$ did in the case of Cochran-Banner model. However, velocity slope post pull-back is significantly increased when increasing failure distention from 2μs to 2.3μs.

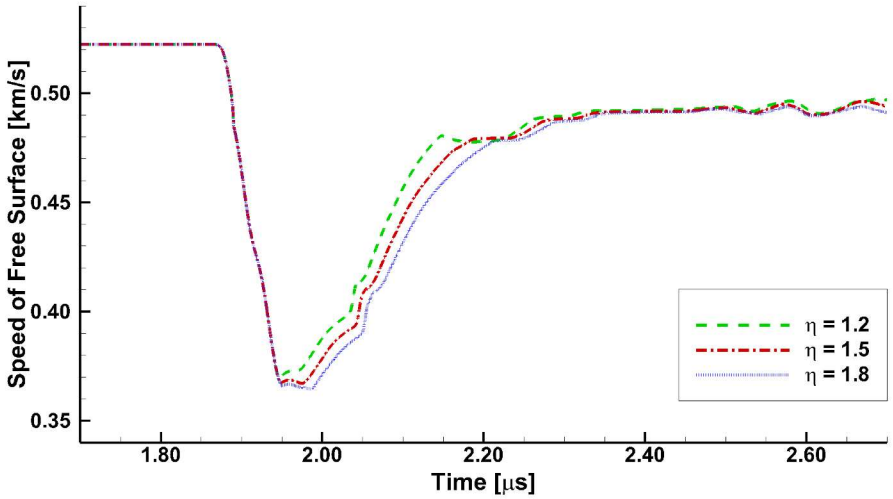


**Figure 57 – Effect of changing $\eta$ on Jim Johnson VNGC model**

As seen in Figure 57, while keeping $a_s$ constant at $a_s = 1.15\text{E}{+}8$ and $\alpha_f$ constant at $\alpha_f = 1.05$, increasing material viscosity $\eta$ marginally increases the pull-back velocity / spall strength, but has no significant effect on the post pull-back velocity slope. However, the rounding that happens immediately after pull-back increases significantly when increasing the viscosity. This indicates that the void growth at constant stress initially is followed by the stress reduction near coalescence. It needs to be mentioned that the VNGC model used in this work is rate independent. The effect of viscosity seen in this work may change if the rate effect is included in the model.

## 6.4 Calibration of VNGC and Cohesive Combined Failure Model

The value of $a_s$ in the VNGC model indirectly controls the spall strength and failure occurs inside the element, where maximum traction $M_{TR}$ in the cohesive element model directly correlates to the spall strength, and failure occurs at the grain boundary. The initial attempt to calibrate the combined failure model through 1D simulations

proved difficult because of the fact that if $M_{TR}$ was low, then the failure occurred at the grain boundary and VNGC was suppressed. If $M_{TR}$ was high, failure occurred by VNGC suppressing the grain boundary failure. This phenomenon may not be as pronounced in 2D and 3D simulations, which will have shear failure at grain boundaries and stress concentration at triple points to initiate the grain boundary failure. Nevertheless, such studies for the combined failure do not exist to the best of the author's knowledge. To gain some insight into the combined failure through 1D simulation, a new procedure was developed. Extensive simulations were carried out at 0.5 km/s impact velocity. The 200 sample values of the two parameters were selected using a uniform sampling method and can be seen in Figure 58.

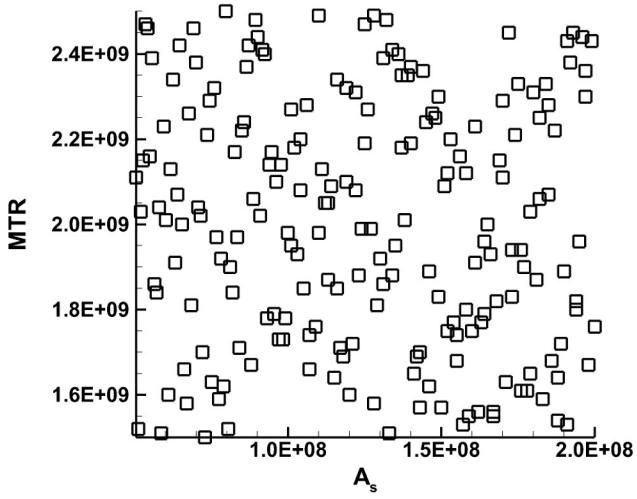


**Figure 58 – Sample values for combined failure parameters $MTR$ and $A_s$**

1D simulations were carried out for each set of values of the two parameters and failure was tracked using a logical flag of 1 or 0. A value of 1 indicates spall failure by cohesive element failure and 0 indicates that no cohesive elements failed. Thus, a flag of 0

(zero) is determined to be a failure by the VNGC failure model. The failure sources are shown in a contour plot in Figure 59.

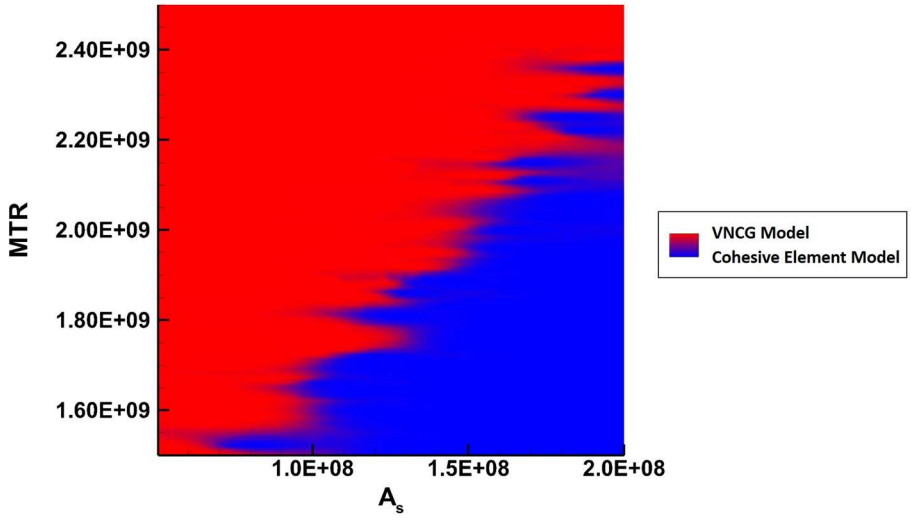


**Figure 59 – Failure source of combined failure model. VNGC failure source is shown (blue) and cohesive element failure source is shown (red)**

As seen in Figure 59, there is a distinct diagonal line between the two failure sources. Along that line, there is an equal chance of each failure mode happening. Because it is known that both failure sources occur in 6061-T6 Aluminum, the best combination of parameter values will be along the line.

Using the two error quantification methods, the model spall strength was compared to the experimental spall strength using Equation 20. The absolute difference in the spall strength for each of the 200 samples was interpolated between the sample and are shown in a 2D contour plot in Figure 60.

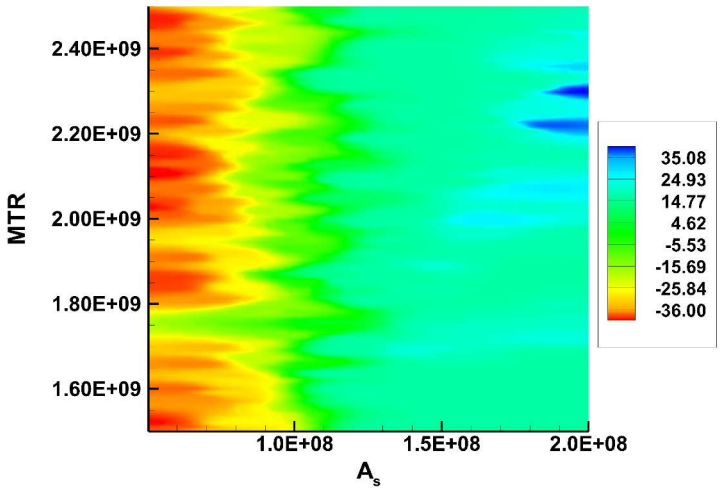


**Figure 60 – Interpolated absolute value of pullback velocity difference for sample values and experimental data from .5km/s flyer-plate impact experiment**

As seen in Figure 60, there is a vertical minimum line with the value of $a_s$ equal to 1.0E+08 and a horizontal minimum line with $M_{TR}$ value at 1.75E+09. Next, the area between the curves was calculated using Equation 27. The error was normalized between 0 and 1 where 0 was the closest match to the data and 1 was the worst match. The contour plot for the normalized error is found in Figure B.13 in Appendix B. Figure B.17 shows the normalized spall strength error and Figure B.14-6 show combinations of each error with different weighting.

The above procedure may serve as the first step towards developing an optimization method to calibrate an inter-grain and intra-grain combined failure model in 2D and 3D. Varying the parameters of the two models by intuition is difficult even for 2D simulations in which the run time will be approximately two days. The method developed will significantly aid in the determination of parameter values that will yield a combined failure

mode and provide pull-back velocity profile quantitatively as well as qualitatively matching the experimental data.

# CHAPTER 7. CONCLUSIONS AND FUTURE WORK

## 7.1 Conclusions

Detailed simulations were carried out in 1D and 2D to understand the shock propagation and spall failure in 6061-T6 Aluminum with and without mesoscale inhomogeneities using intra-grain, inter-grain, and combined intra-grain and inter-grain failure models. Results from 1D simulations using SHOCK-1D and 2D simulations using LS-DYNA for the homogeneous assumption were nearly identical for the same geometry and materials properties providing the needed confidence in the codes and simulation methods used in this work. To evaluate both the compressive state model given by the Mie-Gruneisen EOS and the tensile state model separately, the window was used to isolate the unloading wave interaction by allowing the sample material to unload completely without spall failure. The effectiveness of the window was shown in both a pure homogeneous simulation as well as when either of the failure models were applied; all failure models agreed with the homogeneous simulation with the window present.

The intra-grain failure modelled by the Cochran-Banner and the VNGC models and inter-grain failure modelled by the cohesive model in 1D all predicted the spall strength and pull-back velocity profile in reasonable agreement with the data. The profile of the free surface from the simulation of the separate model failure study agreed with the profile of the combined failure study when using the same “best guess” values. Moreover, the three simple models with fewer parameters offered the ease of interpretation of their parameters as well as the effect of individual parameters on spall failure and measured velocity profile. The spall failure in the combined failure model, attempted for the first time, presented

complexities as expected in 1D simulation. However, when the "best guess" parameter values were used together in the combined failure model, the cohesive element failure model dominates the failure mode over the VNGC failure model with the given parameters. Simulations showed that the lower maximum traction in the cohesive model will cause spall failure by grain boundary cracks suppressing the intra-grain failure by VNGC and vice-versa. This phenomenon will be less pronounced in 2D and 3D simulations, where the grain boundaries are randomly oriented with the presence of stress concentrations at triple points. Such stress concentration will allow failure by VNGC, and the grain boundary traction can still exceed the specified higher value required to couple with the grain boundary fracture.

However, the results of the simulations conducted under the combined failure model indicated the need to develop a more systematic method to study the effect of parameters of the two models. The method developed in this thesis was successful in arriving at the lower and upper bounds of the parameters of the VNGC along with the cohesive model for spall to occur under combined failure modes. It may be concluded that the procedure developed serves as the first step towards developing an optimization module that determines the values of parameters of the combined model to yield spall strength and a pull-back velocity profile that agrees with experimental data.

The 2D simulations showed that the LS-DYNA software is easy to use to simulate the shock response of materials with some exceptions. These exceptions were found mainly in the use of the code's new features of cohesive element that is still under revision and for which neither the theory nor the user manual are fully written. The 2D simulation results for the homogeneous case agreed with the results from the 1D simulations. More

importantly, 2D simulations to evaluate the automatic contact in LS-DYNA not only showed the ease of defining automatic contact, but also provided the response of 20% and 30% porous sand in agreement with expected shock propagation phenomena. The sand simulation was effective in creating heterogeneous grain boundary interaction. It also showed how porosity affected the shock response of the material. The spall simulations with cohesive elements provided results in good agreement with the experimental data except for the lower prediction of wave velocity due to issues with the contact algorithm in the cohesive element formulation. When the cohesive elements were implemented with the best-guess values from the 1D cohesive failure model parameters, the 2D simulation showed spall strength in agreement to the 1D cohesive element failure model. However, due to other parameters in the 2D cohesive model, there was an observed delay caused by a reduction in the shock velocity. Nevertheless, the present work shows that LS-DYNA can be an effective software package to model spall using a combined failure model after necessary tweaking of the cohesive model. Unlike other popular finite element codes, it is easy to add material models to LS-DYNA.

## 7.1 Future Work

Further work is needed to develop an optimization module to determine the five parameters for the 1D combined failure model to predict the spall strength as well as the pull-back velocity profile in agreement with experimental data. The approach adopted is independent of the 1D or 2D simulations, relying primarily on the experimental data and simulated spall strength and pull-back velocity profile.

More work is needed for truly combined failure simulations in 2D using LS-DYNA. To do this, a UMAT for a simple VNGC model needs to be added to the LS-DYNA. Lastly, the optimization module needs to be coupled with the LS-DYNA simulation procedure to fine tune the parameter values for 2D combined failure. Lastly, simulations need to be carried out at varying impact velocities and for other materials, which will require more experimental spall data.

# APPENDIX A. MATERIAL PROPERTIES

Table A.1 shows the material and EOS properties used for the Aluminum 6061-T6 sample in the 1D cases. In the 1.3km/s impactor case, the impactor is also made of the Aluminum 6061-T6.

**Table A.1 – Material and EOS properties for Aluminum 6061-T6**

| **Material Parameter** | **Symbol** | **Value** | **Unit** |
|---|---|---|---|
| Density | $\rho_0$ | 2.703E+03 | kg/m$^3$ |
| Linear Artificial Viscosity | $A_L$ | 3.000E-01 | |
| Quadratic Artificial Viscosity | $A_Q$ | 2.000E+00 | |
| Shear Modulus | $G_0$ | 2.993E+10 | Pa |
| Yield Stress | $\sigma_Y$ | 3.240E+08 | Pa |
| Hardening Coefficient | $H$ | 1.050E+09 | Pa |
| Ultimate Yield Stress | $\sigma_U$ | 1.000E+20 | Pa |
| **EOS Parameter** | | | |
| Coeff 0 | $K_0$ | 7.116E+10 | Pa |
| Coeff 1 | $K_1$ | 0.000E+00 | Pa |
| Coeff 2 | $K_2$ | 1.584E+11 | Pa |
| Coeff 3 | $K_3$ | 9.235E+10 | Pa |
| Gruneisen Coefficient | $\gamma_0$ | 2.000E+00 | |

Table A.2 shows the material and EOS properties for Z-Cut quartz, which is used as the impactor in the .5km/s spall experiment. Some of the major differences between the material properties of the Z-Cut Quartz and he Aluminum 6061-T6 are that the Z-Cut Quartz has an ultimate yield stress, which is lower than the yield stress. This is done to impose brittle material properties.

**Table A.2 – Material and EOS properties for Z-Cut Quartz**

| **Material Parameter** | **Symbol** | **Value** | **Unit** |
|---|---|---|---|
| Density | $\rho_0$ | 2.648E+03 | kg/m$^3$ |
| Linear Artificial Viscosity | $A_L$ | 2.000E-01 | |
| Quadratic Artificial Viscosity | $A_Q$ | 2.000E+00 | |
| Shear Modulus | $G_0$ | 4.692E+10 | Pa |
| | $G_1$ | 1.873E+00 | Pa |
| | $G_2$ | 3.459E-10 | Pa |
| Yield Stress | $\sigma_Y$ | 1.000E+20 | Pa |
| Hardening Coefficient | $H$ | 0 | Pa |
| Ultimate Yield Stress | $\sigma_U$ | 4.400E+09 | Pa |
| **EOS Parameter** | | | |
| Coeff 0 | $K_0$ | 4.319E+10 | Pa |
| Coeff 1 | $K_1$ | 0 | Pa |
| Coeff 2 | $K_2$ | 1.562E+11 | Pa |
| Coeff 3 | $K_3$ | 4.860E+10 | Pa |
| Gruneisen Coefficient | $\gamma_0$ | 6.750E-01 | |

Table A.3 shows the properties for the LiF window used in the simulations comparing the different failure model loading and unloading. LIF is used because it has a similar impedance to the Aluminum 6061-T6.

**Table A.3 – Material and EOS properties for Lithium Fluoride (LiF)**

| Material Parameter | Symbol | Value | Unit |
|---|---|---|---|
| Density | $\rho_0$ | 2.640E+03 | kg/m$^3$ |
| Linear Artificial Viscosity | $A_L$ | 1.000E-01 | |
| Quadratic Artificial Viscosity | $A_Q$ | 2.000E+00 | |
| Shear Modulus | $G_0$ | 3.000+10 | Pa |
| | $G_1$ | 1.325E+00 | Pa |
| | $G_2$ | -6.450E-10 | Pa |
| Yield Stress | $\sigma_Y$ | 9.030E+07 | Pa |
| Hardening Coefficient | $H$ | 0 | Pa |
| Ultimate Yield Stress | $\sigma_U$ | 1.000E+20 | Pa |
| **EOS Parameter** | | | |
| Coeff 0 | $K_0$ | 7.000E+10 | Pa |
| Coeff 1 | $K_1$ | 0 | Pa |
| Coeff 2 | $K_2$ | 1.074E+11 | Pa |
| Coeff 3 | $K_3$ | 1.288E+10 | Pa |
| Gruneisen Coefficient | $\gamma_0$ | 1.630 | |

Table A.4 shows the material and EOS properties of Lexan. Lexan was used as a backing for the 1.3km/s impact experiment to keep the integrity of the flyer.

**Table A.4 – Material and EOS properties for Lexan**

| **Material Parameter** | **Symbol** | **Value** | **Unit** |
|---|---|---|---|
| Density | $\rho_0$ | 2.648E+03 | kg/m$^3$ |
| Linear Artificial Viscosity | $A_L$ | 2.000E-01 | |
| Quadratic Artificial Viscosity | $A_Q$ | 2.000E+00 | |
| Shear Modulus | $G_0$ | 4.692E+10 | Pa |
| | $G_1$ | 1.873E+00 | Pa |
| | $G_2$ | 3.459E-10 | Pa |
| Yield Stress | $\sigma_Y$ | 1.000E+20 | Pa |
| Hardening Coefficient | $H$ | 0 | Pa |
| Ultimate Yield Stress | $\sigma_U$ | 4.400E+09 | Pa |
| **EOS Parameter** | | | |
| Coeff 0 | $K_0$ | 4.319E+10 | Pa |
| Coeff 1 | $K_1$ | 0 | Pa |
| Coeff 2 | $K_2$ | 1.562E+11 | Pa |
| Coeff 3 | $K_3$ | 4.860E+10 | Pa |
| Gruneisen Coefficient | $\gamma_0$ | 6.750E-01 | |

# APPENDIX B. ADDITIONAL FIGURES AND TABLES

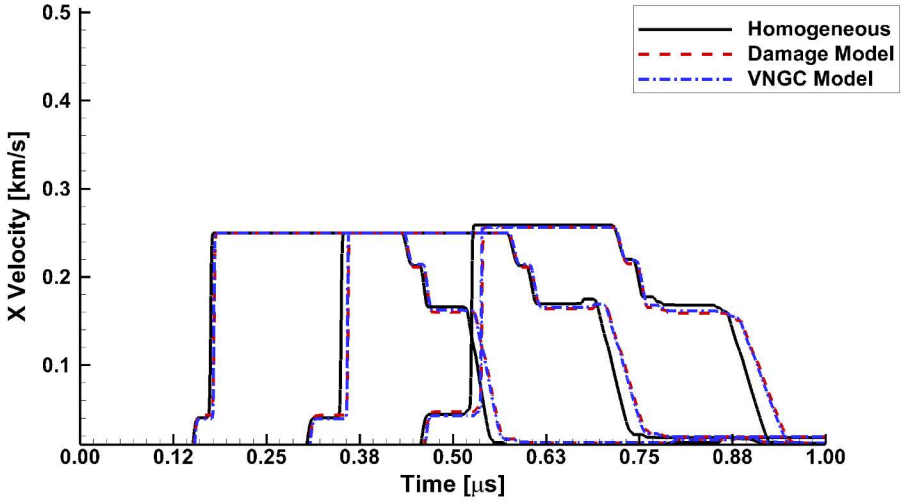


**Figure B.1 – Homogeneous SHOCK-1D X Velocity results (black) compared to damage model results (red) and VNGC model (blue) for .5km/s impactor with LiF window**

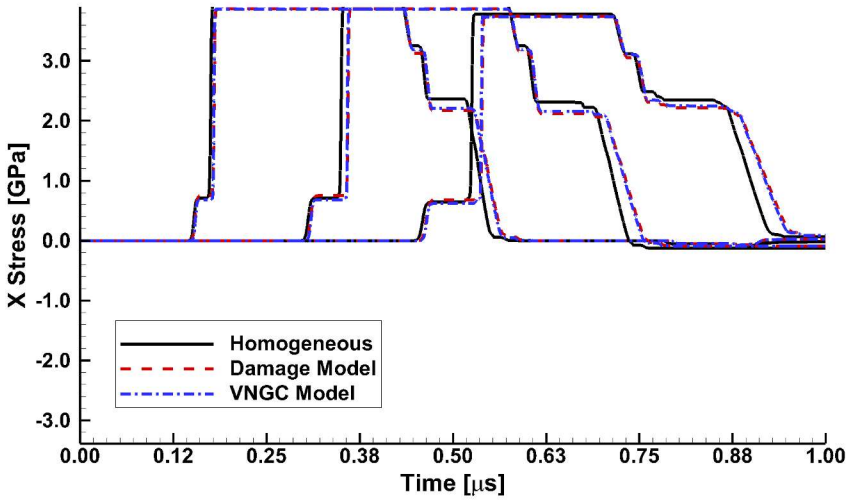


**Figure B.2 – Homogeneous SHOCK-1D X Stress results (black) compared to damage model results (red) and VNGC model (blue) for .5km/s impactor with LiF window**

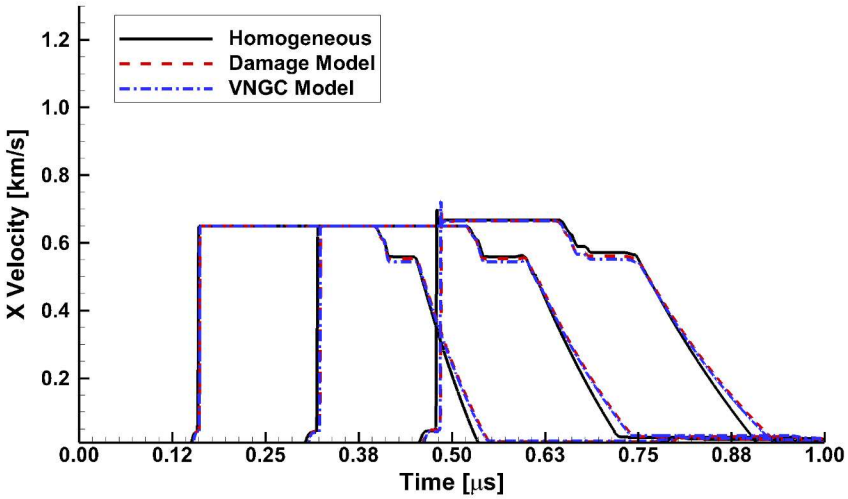


**Figure B.3 – Homogeneous SHOCK-1D X Velocity results (black) compared to damage model results (red) and VNGC model (blue) for 1.3km/s impactor with LiF window**

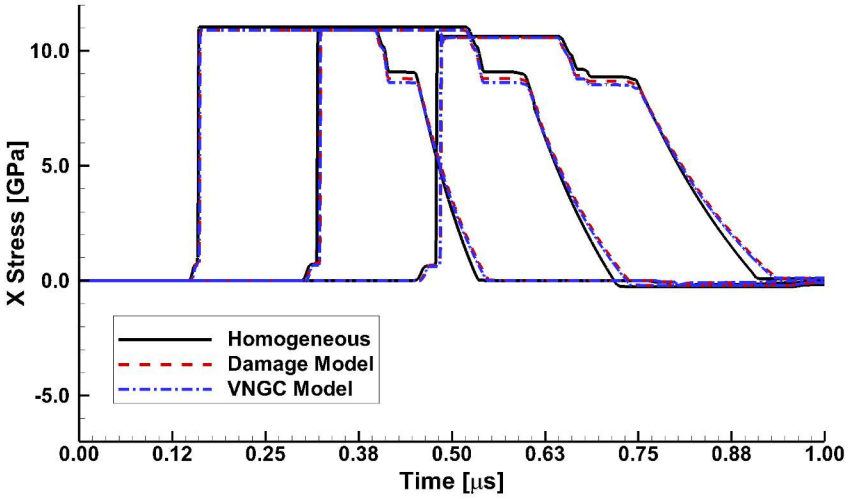


**Figure B.4 – Homogeneous SHOCK-1D X Stress results (black) compared to damage model results (red) and VNGC model (blue) for 1.3km/s impactor with LiF window.**

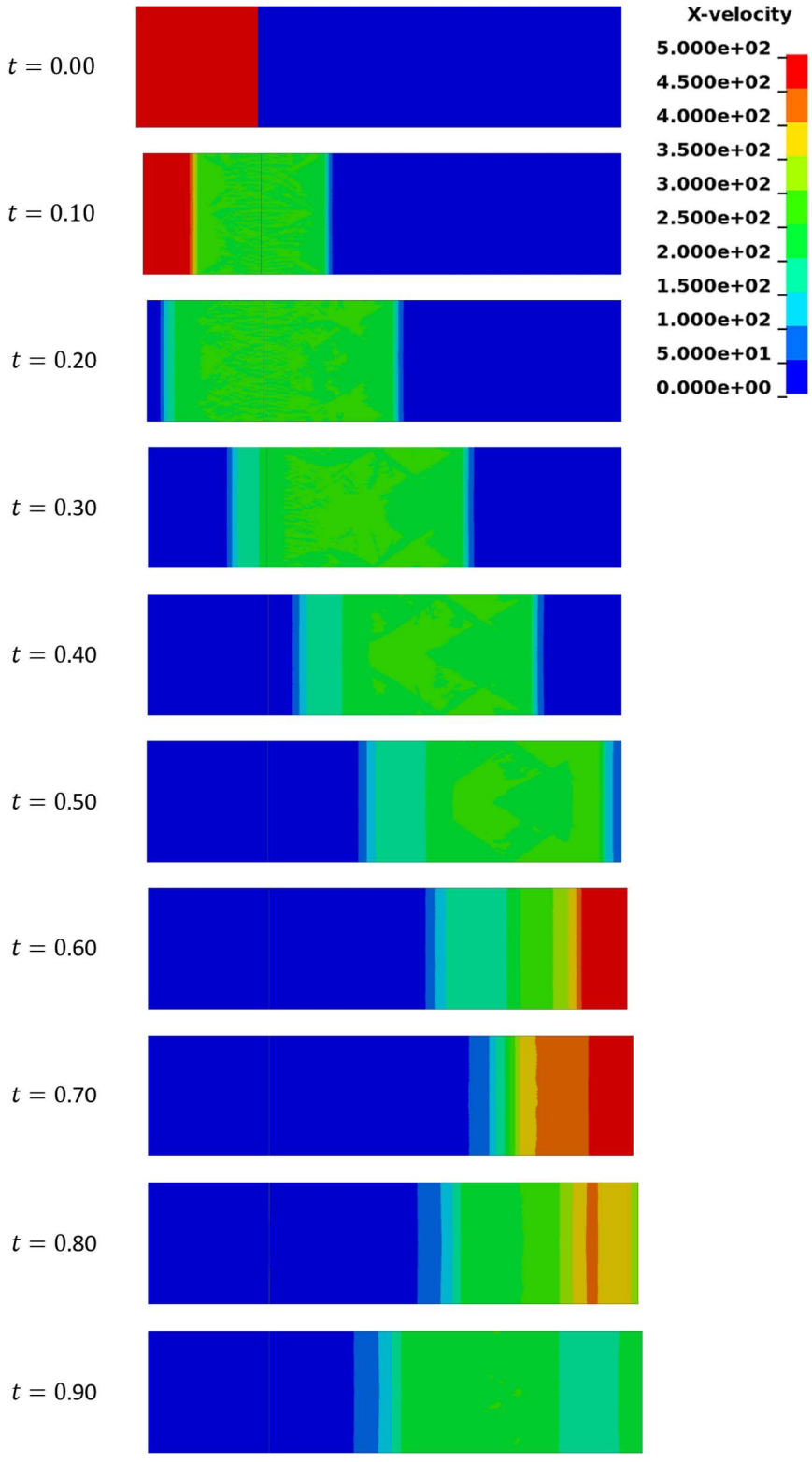


**Figure B.5 – Contour results for X velocity of 2D LS-DYNA homogeneous simulation with .5km/s impactor**

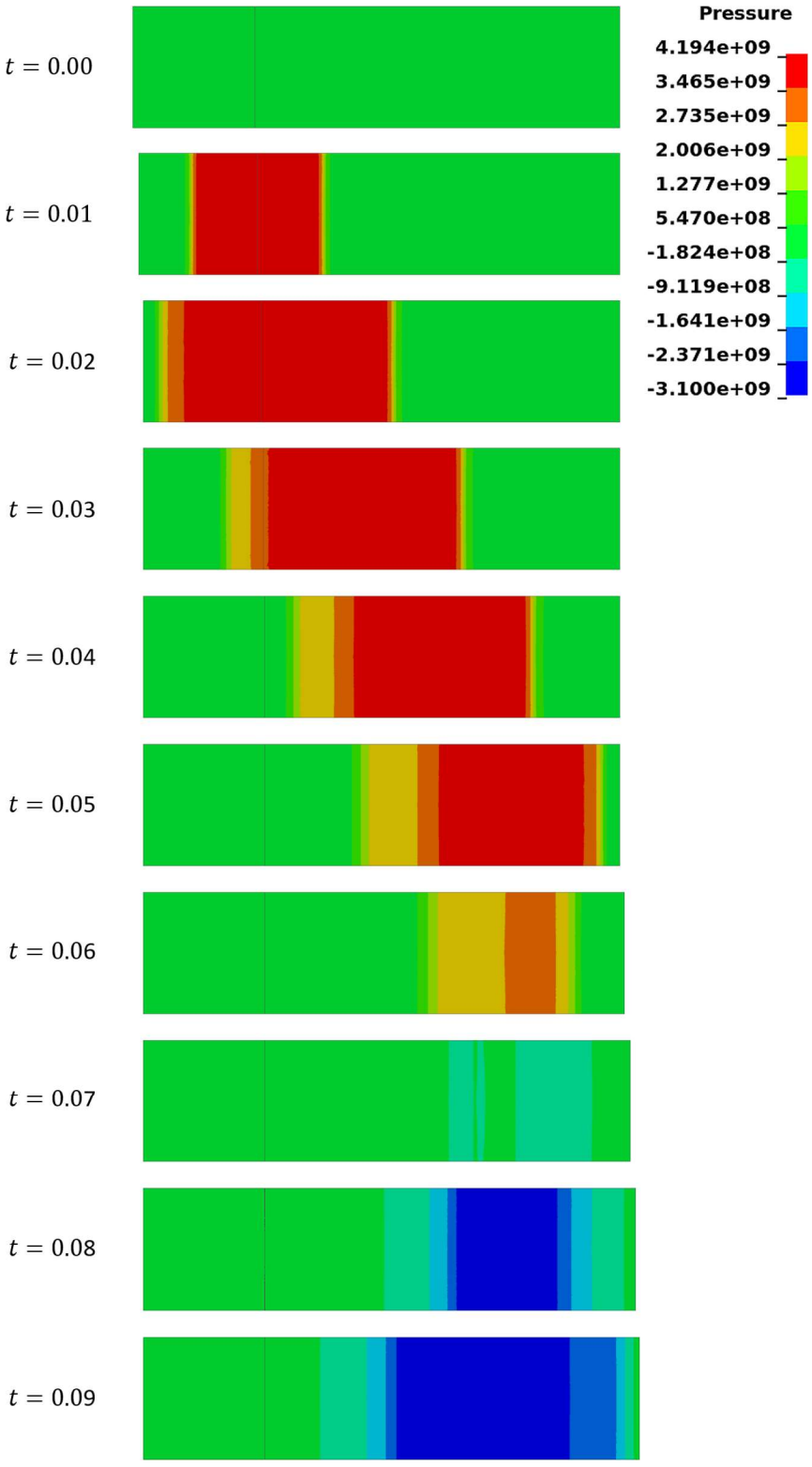


**Figure B.6 – Contour results for pressure of 2D LS-DYNA homogeneous simulation with .5km/s impactor**

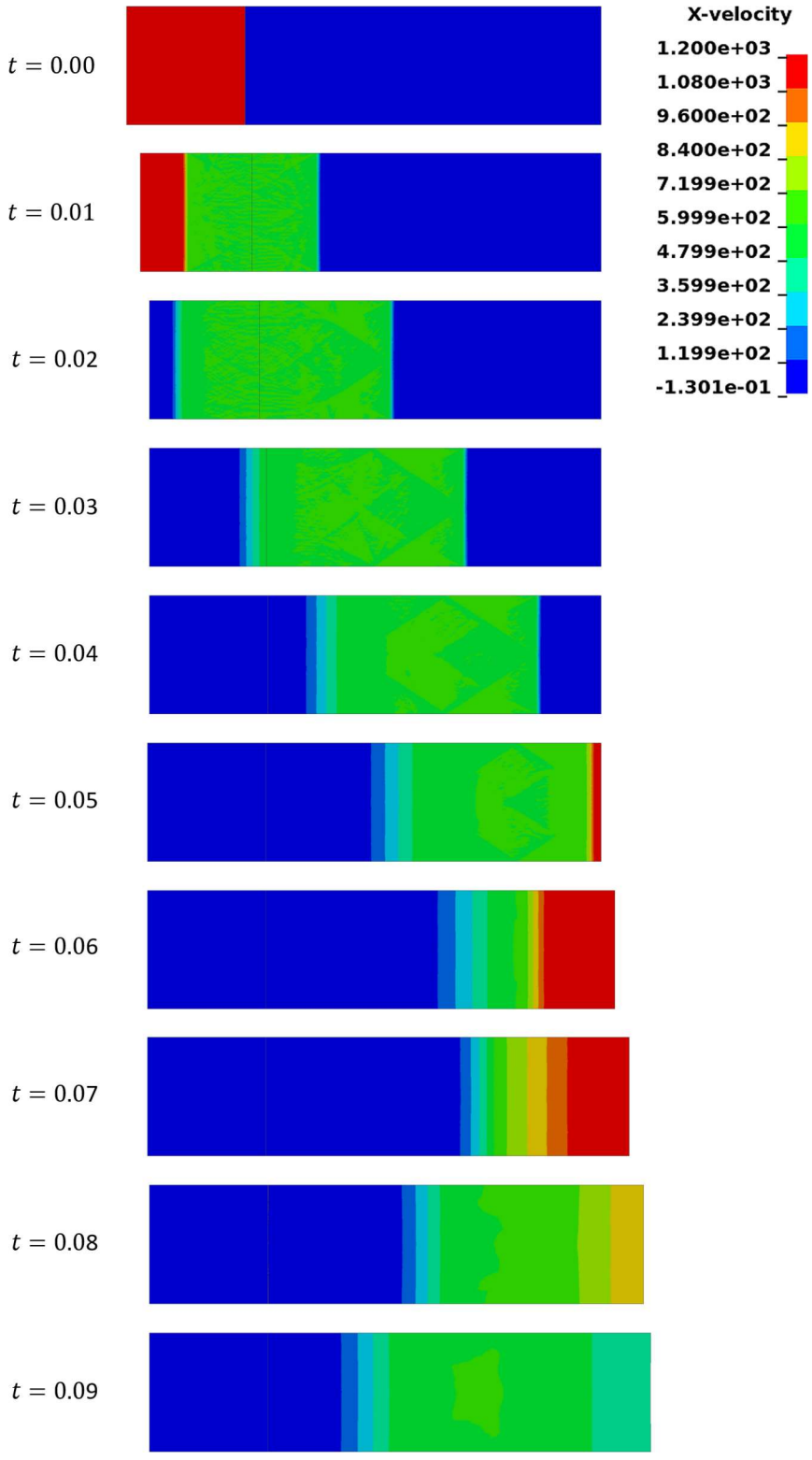


**Figure B.7 – Contour results for X velocity of 2D LS-DYNA homogeneous simulation with 1.3km/s impactor**

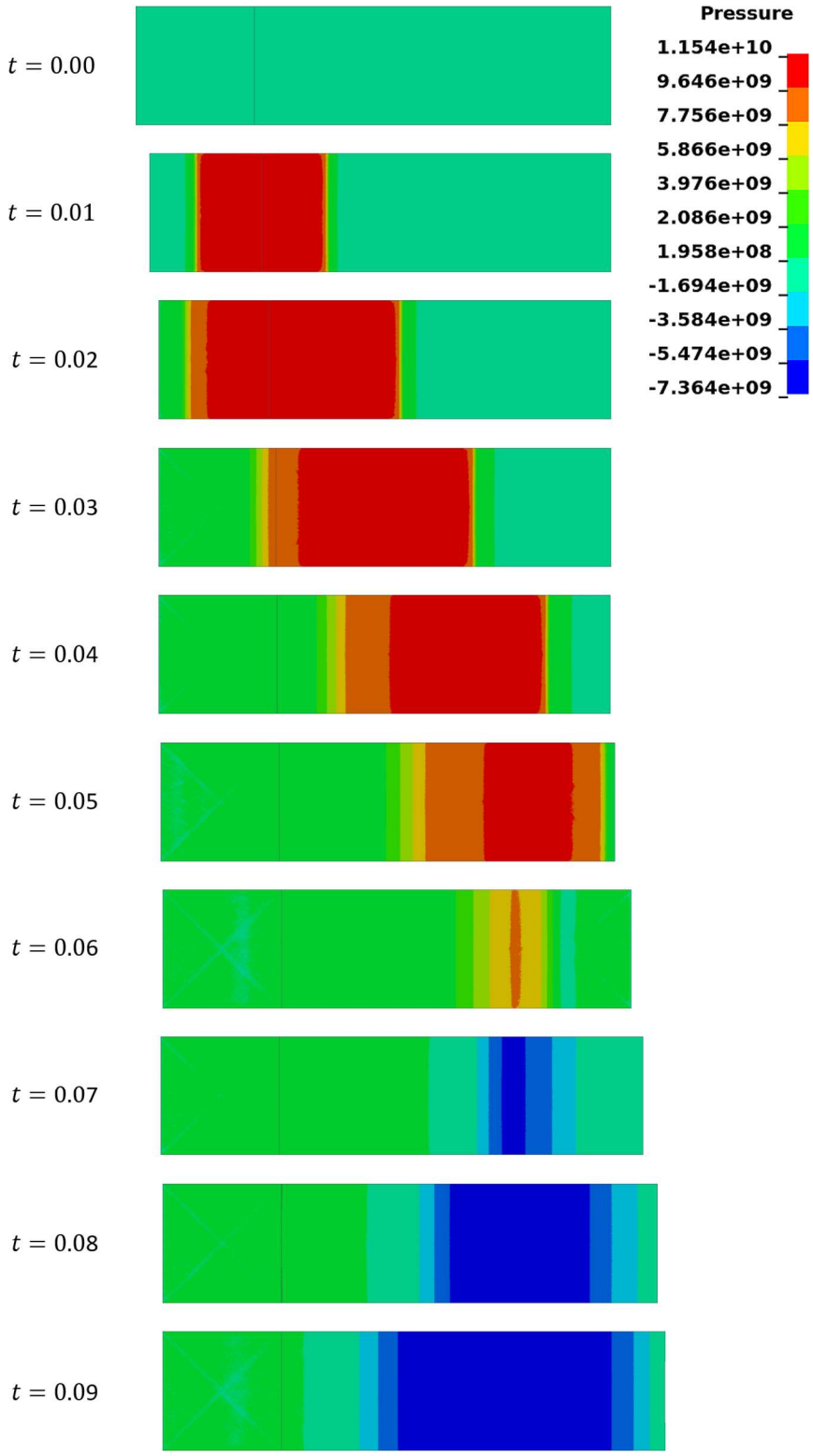


**Figure B.8 – Contour results for pressure of 2D LS-DYNA homogeneous simulation with 1.3km/s impactor**

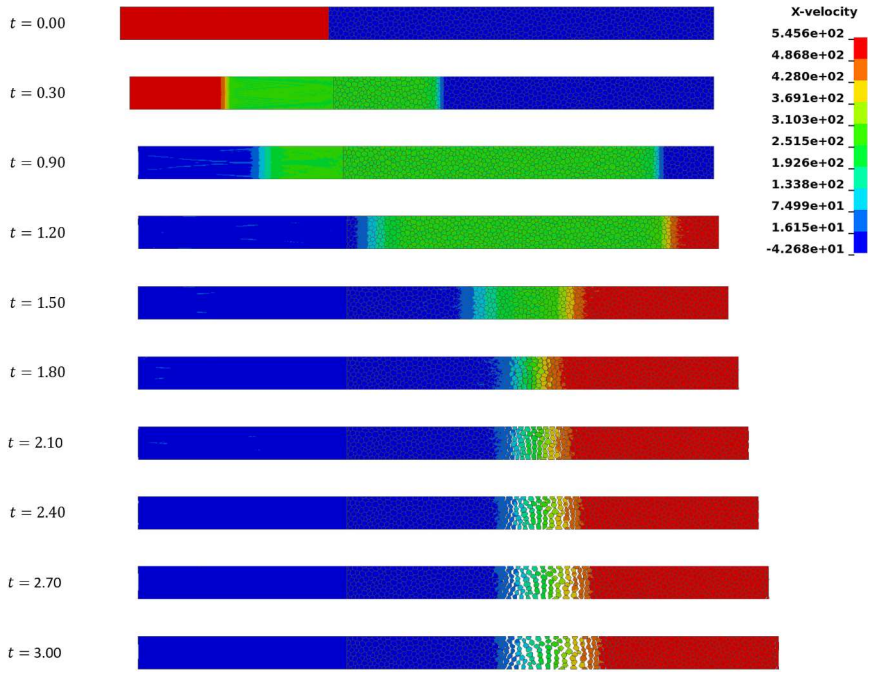


**Figure B.9 – Contour of X velocity results for contact-only granular simulation for .5km/s impactor**

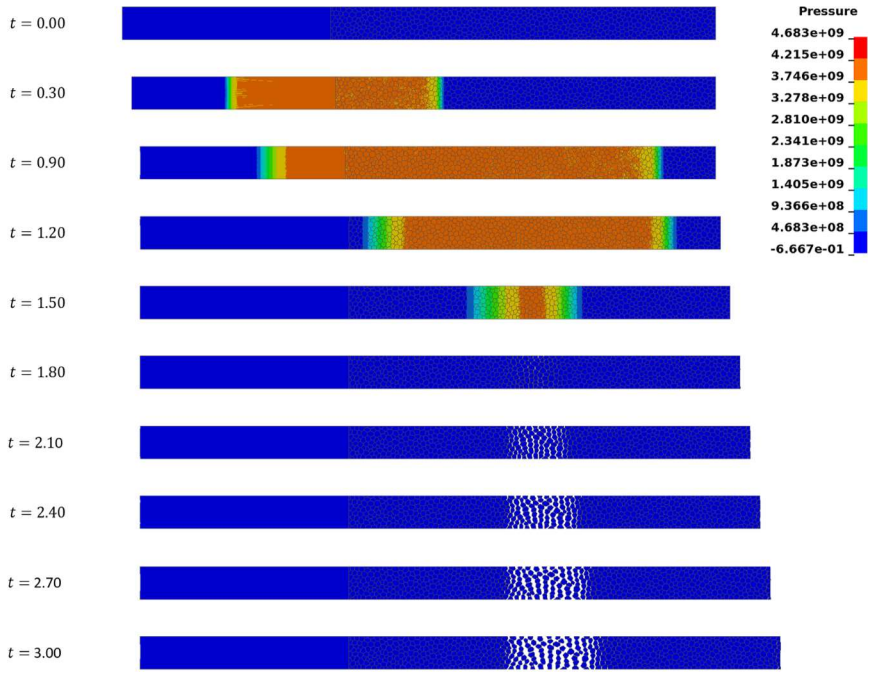


**Figure B.10 – Contour of pressure results for contact-only granular simulation for .5km/s impactor**

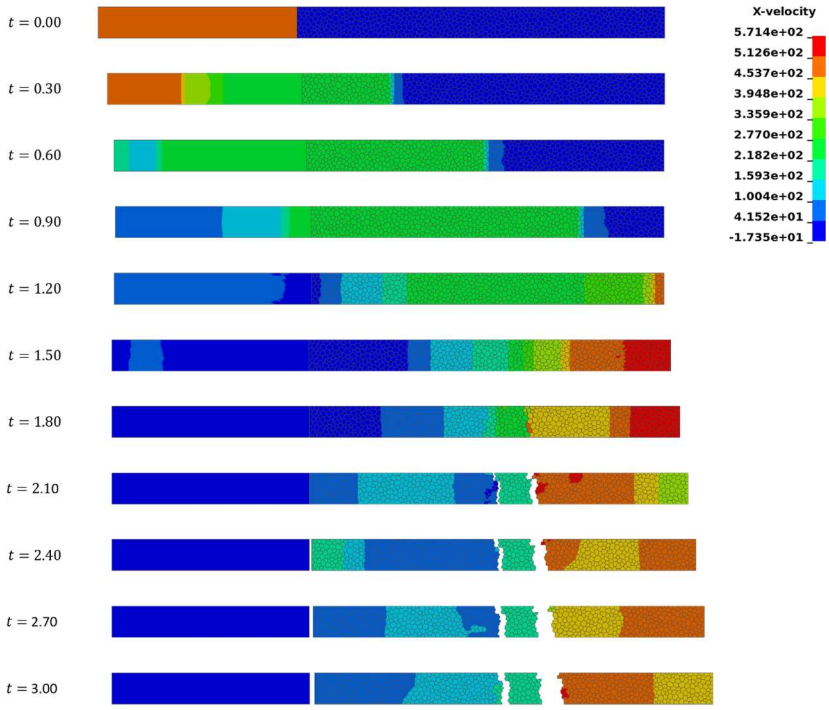


**Figure B.11 – Contour of X velocity results for granular simulation with cohesive elements for .5km/s impactor**

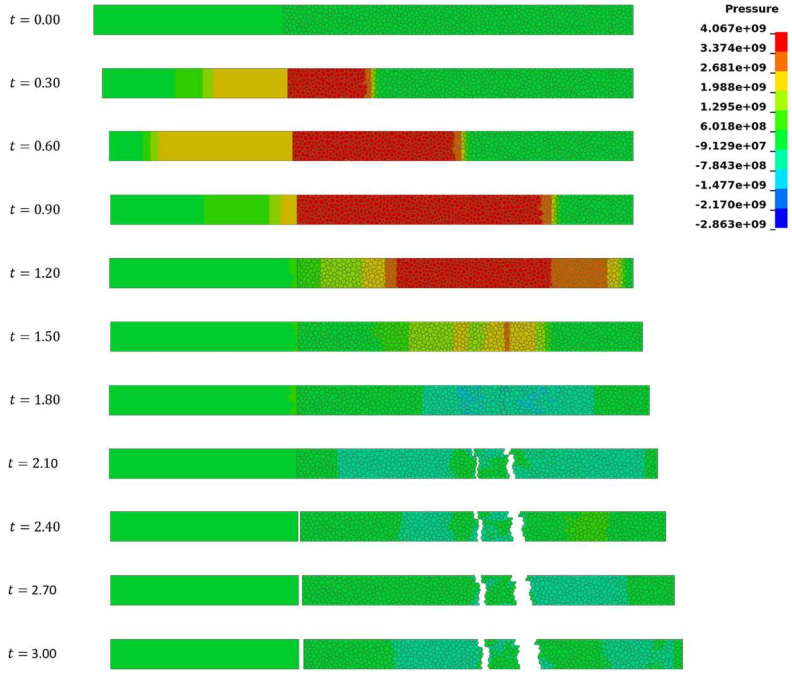


**Figure B.12 – Contour of pressure results for granular simulation with cohesive elements for .5km/s impactor**

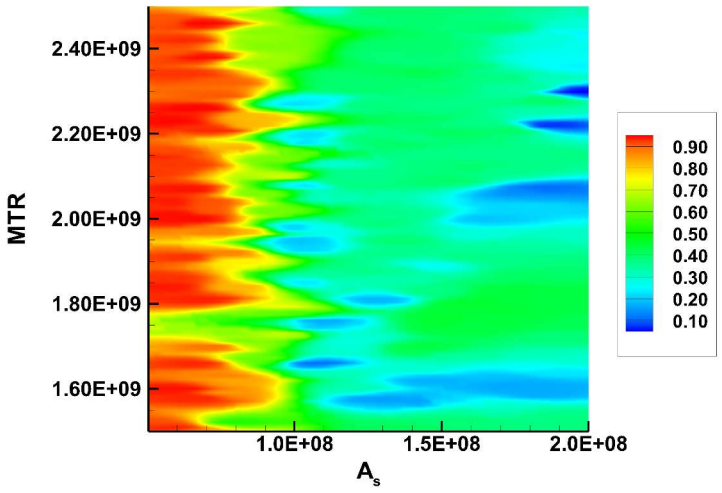


**Figure B.13 – Normalized area between curves error between combined failure model and experimental free surface velocity**

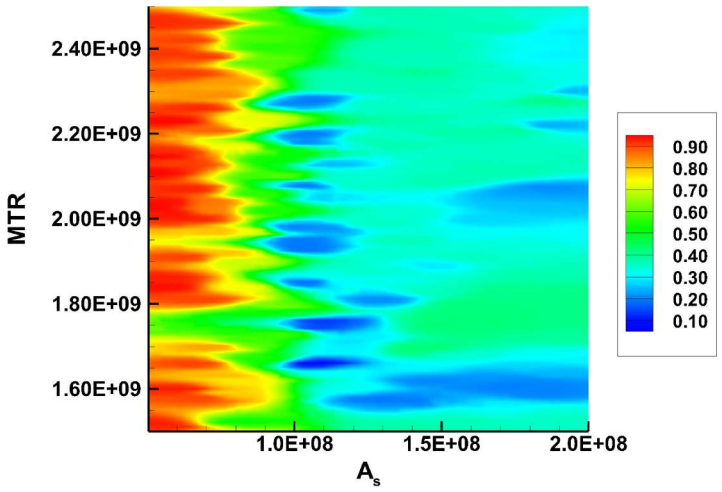


**Figure B.14 – 75% normalized area between curves error and 25% normalized spall strength error**

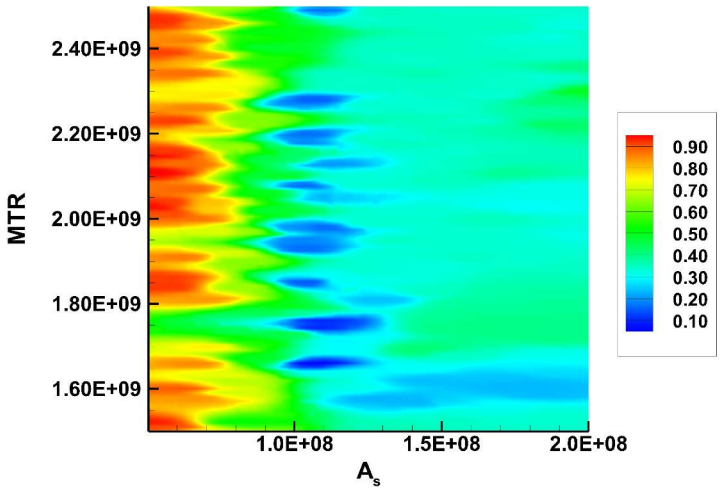


**Figure B.15 – 50% normalized area between curves error and 50% normalized spall strength error**

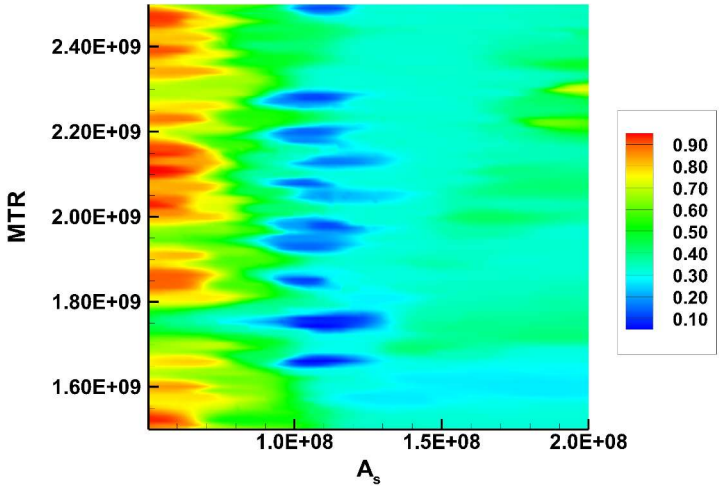


**Figure B.16 – 25% normalized area between curves error and 75% normalized spall strength error**

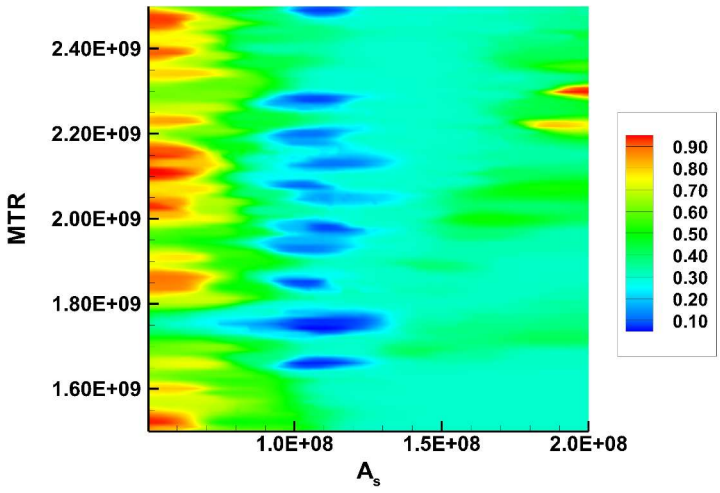


**Figure B.17 – Normalized spall strength error between combined failure model and experimental free surface velocity**

# REFERENCES


[1] P. A. Tipler, *Physics for Scientists and Engeneers: Vol. 1: Mechanics, Oscillations and Waves, Thermodynamics*: W. H. Freeman, 1999.

[2] X. Chen, J. R. Asay, S. K. Dwivedi, and D. P. Field, "Spall behavior of aluminum with varying microstructures," *Journal of Applied Physics,* vol. 99, p. 023528, 2006.

[3] T. Antoun, L. Seaman, D. R. Curran, G. I. Kanel, S. V. Razorenov, and A. V. Utkin, *Spall Fracture*: Springer New York, 2006.

[4] J. W. Forbes, *Shock wave compression of condensed matter a primer*. Berlin: Springer, 2012.

[5] C. E. Morris, *Los Alamos Shock Wave Profile Data*: University of California Press, 1982.

[6] T. Ahrens, "Equation of state," in *High-Pressure Shock Compression of Solids*, ed: Springer, 1993, pp. 75-113.

[7] S. K. Dwivedi, J. L. Ding, and Y. M. Gupta, "COMPUTATIONAL STUDY OF INTERFACE EFFECT ON IMPACT LOAD SPREADING IN SiC MULTI-LAYERED TARGETS," *International Journal of Computational Methods,* vol. 02, pp. 341-373, 2005.

[8] M. H. Rice, R. G. McQueen, and J. M. Walsh, "Compression of Solids by Strong Shock Waves," in *Solid State Physics*. vol. Volume 6, S. Frederick and T. David, Eds., ed: Academic Press, 1958, pp. 1-63.

[9] G. Johnson, "High velocity impact calculations in three dimensions," *Journal of Applied Mechanics,* vol. 44, pp. 95-100, 1977.

[10] L. E. Malvern, *Introduction to the mechanics of a continuous medium*: Prentice-Hall, 1969.

[11] S. K. Dwivedi, J. R. Asay, and Y. M. Gupta, "Two-dimensional mesoscale simulations of quasielastic reloading and unloading in shock compressed aluminum," *Journal of Applied Physics,* vol. 100, pp. 083509 1-15, 2006.

[12] G. R. Fowles, "Shock Wave Compression of Hardened and Annealed 2024 Aluminum," *Journal of Applied Physics,* vol. 32, pp. 1475-1487, 1961.

[13] E. S. Hertel, R. L. Bell, M. G. Elrick, A. V. Farnsworth, G. I. Kerley, J. M. McGlaun*, et al.*, "CTH: A Software Family for Multi-Dimensional Shock Physics Analysis," in *Shock Waves @ Marseille I: Hypersonics, Shock Tube & Shock*

*Tunnel Flow*, R. Brun and L. Z. Dumitrescu, Eds., ed Berlin, Heidelberg: Springer Berlin Heidelberg, 1995, pp. 377-382.

[14] T. Belytschko and T. J. R. Hughes, *Computational Methods for Transient Analysis*: North-Holland, 1983.

[15] S. K. Dwivedi, "Shock-1D, An updated Lagrangian shock propagation simulation code with multi-body contact dynamics and 1D grain-boundary cohesion," ed: University of Florida, Reef, Shalimar, FL 32579/Georgia Institute of Technology, Atlanta, GA 30332, 2013.

[16] J. O. Hallquist, "LS-DYNA Keyword User's Manual," *Livermore Software Technology Corporation,* vol. 7374, 2007.

[17] D. Chen, Y. Yuying, Y. Zhihua, W. Huanran, L. Guoqing, and X. Shugang, "A modified Cochran–Banner spall model," *International Journal of Impact Engineering,* vol. 31, pp. 1106-1118, 10// 2005.

[18] S. Cochran and D. Banner, "Spall studies in uranium," *Journal of Applied Physics,* vol. 48, pp. 2729-2737, 1977.

[19] J. N. Johnson, "Dynamic fracture and spallation in ductile solids," *Journal of Applied Physics,* vol. 52, pp. 2812-2825, 1981.

[20] D. Curran, L. Seaman, and D. Shockey, "Dynamic failure of solids," *Physics reports,* vol. 147, pp. 253-388, 1987.

[21] G. L. Goudreau and J. O. Hallquist, "Recent developments in large-scale finite element lagrangian hydrocode technology," *Computer Methods in Applied Mechanics and Engineering,* vol. 33, pp. 725-757, 1982/09/01 1982.

[22] J. R. Rice and D. M. Tracey, "On the ductile enlargement of voids in triaxial stress fields∗," *Journal of the Mechanics and Physics of Solids,* vol. 17, pp. 201-217, 1969/06/01 1969.

[23] V. Tvergaard, "Void shape effects and voids starting from cracked inclusion," *International Journal of Solids and Structures,* vol. 48, pp. 1101-1108, 4// 2011.

[24] S. K. Dwivedi, R. D. Teeter, C. W. Felice, and Y. M. Gupta, "Two dimensional mesoscale simulations of projectile instability during penetration in dry sand," *Journal of Applied Physics,* vol. 104, p. 083502, 2008.

[25] S. Pierce and W. Charlie, "High-intensity compressive stress wave propagation through unsaturated sands," DTIC Document1990.

[26] D. Stöffler, D. E. Gault, J. Wedekind, and G. Polkowski, "Experimental hypervelocity impact into quartz sand: Distribution and shock metamorphism of ejecta," *Journal of Geophysical Research,* vol. 80, pp. 4062-4077, 1975.

[27] J. VonNeumann and R. D. Richtmyer, "A Method for the Numerical Calculation of Hydrodynamic Shocks," *Journal of Applied Physics,* vol. 21, pp. 232-237, 1950.

[28] M. L. Wilkins, "Use of artificial viscosity in multidimensional fluid dynamic calculations," *Journal of Computational Physics,* vol. 36, pp. 281-303, 1980/07/15 1980.

[29] M. L. Wilkins, Lawrence Livermore Laboratory, and Lawrnece Radiation Laboratory University of California, Berkeley, *Calculation of elastic-plastic flow*: University of California Lawrence Radiation Laboratory, 1963.